Journal of Sensors

Sensor Based Intelligent Systems for Detection and Diagnosis

Guest Editors: Mehmet Karakose, Sergiu Dan Stan, Ilhan Aydin, and Manuel Pineda-Sanchez

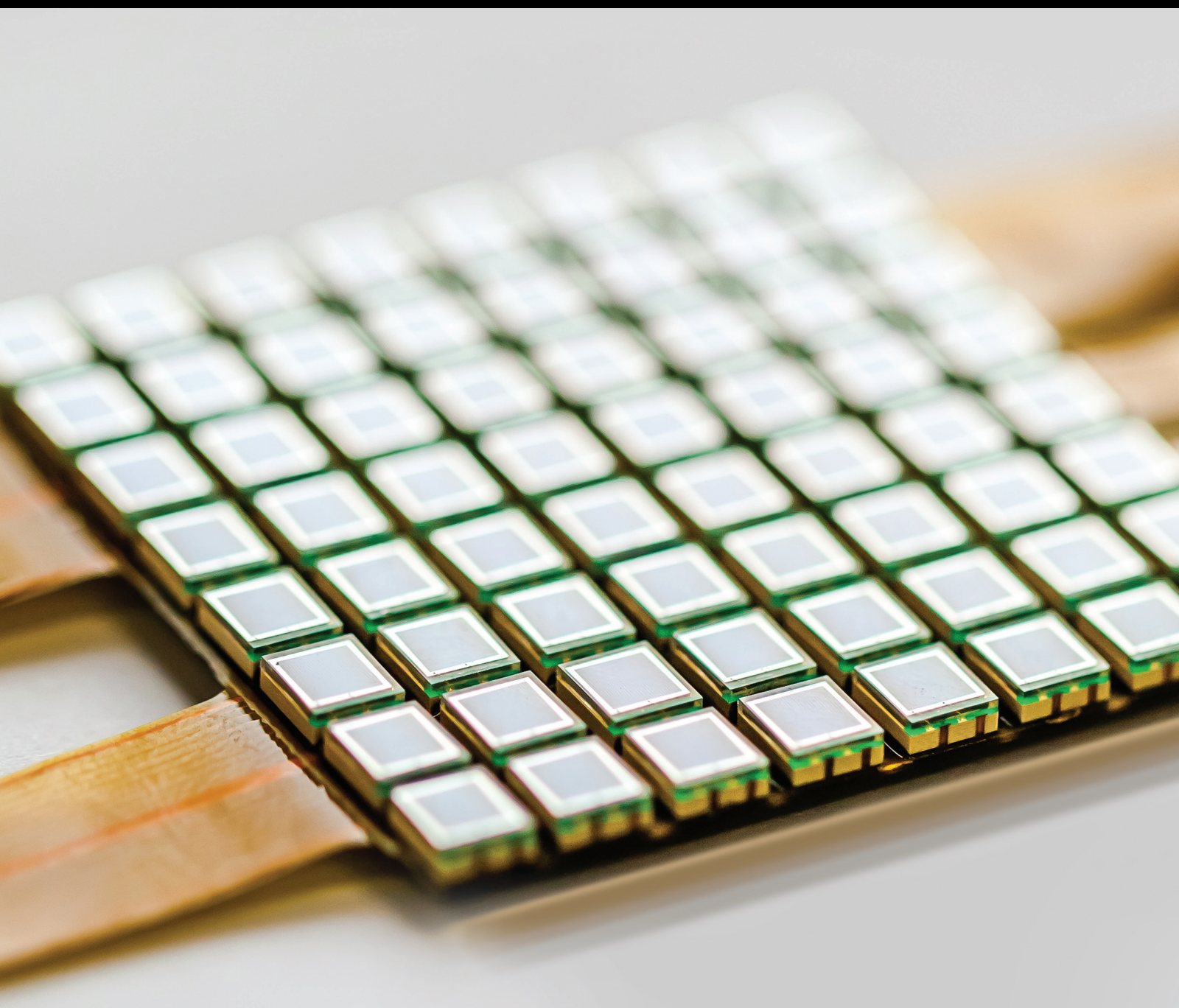

Sensor Based Intelligent Systems for Detection and Diagnosis

Journal of Sensors

Sensor Based Intelligent Systems for Detection and Diagnosis

Guest Editors: Mehmet Karakose, Sergiu Dan Stan, Ilhan Aydin, and Manuel Pineda-Sanchez

Editorial Board

Contents

Hindawi Publishing Corporation
Journal of Sensors
Volume 2016, Article ID 5269174, 1 page
http://dx.doi.org/10.1155/2016/5269174

Editorial

Sensor Based Intelligent Systems for Detection and Diagnosis

Mehmet Karakose

Computer Engineering, Firat University, 23119 Elazig, Turkey

Correspondence should be addressed to Mehmet Karakose; mkarakose@firat.edu.tr

Received 11 August 2015; Accepted 16 September 2015

Sensors are very commonly used as monitoring and observing elements in real world applications. However, sensors cannot provide a solution for systems, because data obtained with sensors should be processed for object functions. There are many approaches for processing and decision-making methods in industrial applications. In particular, it is very important for intelligent systems which used condition monitoring, detection, diagnosis, prognosis, and predictive maintenance.

The predictive maintenance basically consists of four components. These components are the condition monitoring, the detection, the diagnosis, and the prognosis for identification of anomalies and faulty conditions. The condition monitoring is monitoring of one or several parameters to identify an unexpected situation. The detection is indicating if there is an abnormal status using observable effects in a monitored system. The diagnosis is the process of detecting and determining where that anomaly is. The prognosis is predicting and estimating useful and healthy status of a system.

A lot of predictive maintenance techniques have been improved for detection, diagnosis, and prognosis of faults in the literature. The detection, diagnosis, and prognosis methods use measurements and preprocessed data using the condition monitoring. Then, the predictive maintenance methods provide a result for health of system. But systems have many uncertainties and they affect the performance of the predictive maintenance method. Therefore, intelligent systems are used to avoid this disadvantage. Process flow of the predictive maintenance is as follows. Firstly, actual functions or signals in any system for the condition monitoring are measured. Secondly, normal operation or faulty operation of the system for early recognition is determined in the anomaly detection. Thirdly, anomaly classification for correct assignment can be carried out for the diagnosis. Next, the prognosis stage can be used to estimate or predict anomalies. Finally, a result is obtained with decision-making.

An efficient predictive maintenance method should have some specifications. First of all, minimum information and sensor should be required. Other specifications are accurate and confident prediction, fast response, and robustness. Optimization algorithms such as genetic algorithms, artificial immune systems, and advanced Monte Carlo methods, learning algorithms such as artificial neural networks and support vector machines, and reasoning algorithms such as fuzzy logic systems, clustering algorithms, particle filtering algorithms, wavelet analysis algorithms, and principal component analysis algorithm can be used for the predictive maintenance methods. These methods can be used in data preprocessing, feature extraction, and feature selection too.

Finally, the predictive maintenance methods using computational intelligence techniques are very important for improving production and manufacturing and product quality. If the faulty condition in a system can be determined with the detection, the diagnosis, or the prognosis in early stage, most problems can be repaired at this time.

Mehmet Karakose

Hindawi Publishing Corporation
Journal of Sensors
Volume 2016, Article ID 9307560, 9 pages
http://dx.doi.org/10.1155/2016/9307560

Research Article

Fault Reconstruction Based on Sliding Mode Observer for Current Sensors of PMSM

Changfan Zhang, Huijun Liao, Xiangfei Li, Jian Sun, and Jing He

College of Electrical and Information Engineering, Hunan University of Technology, Zhuzhou, Hunan 412007, China

Correspondence should be addressed to Jing He; hejing@263.net

Received 6 January 2015; Revised 20 April 2015; Accepted 20 April 2015

Academic Editor: Mehmet Karakose

This paper deals with a method of phase current sensor fault reconstruction for permanent magnet synchronous motor (PMSM) drives. A new state variable is introduced so that an augmented system can be constructed to treat PMSM sensor faults as actuator faults. This method uses the PMSM two-phase stationary reference frame fault model and a sliding mode variable structure observer to reconstruct fault signals. A logic algorithm is built to isolate and identify the faulty sensor for a stator phase current fault after reconstructing the two-phase stationary reference frame fault signals, which allows the phase fault signals to be reconstructed. Simulation results are presented to illustrate the functionality of the theoretical developments.

1. Introduction

Permanent magnet synchronous motors (PMSMs) are an important category of electric machines, in which the rotor magnetization is created by permanent magnets attached to the rotor. Due to their high efficiency, high ratio of torque to weight, high power factor, faster response, and rugged construction, PMSMs are widely used for high performance variable speed motors in many industry applications. With the development of permanent magnet materials, especially the neodymium-iron-boron (Nd-Fe-B), which has high magnetic energy, high coercive force, and low price, the applications of PMSMs have become more extensive in recent years.

High performance systems usually have demanding requirements on availability, reliability, and survivability [1]. The reliable operation of PMSM is a primary concern for the entire ship system. Early detection of abnormalities in the PMSM drives will help to avoid failures. Indeed, detection, location, and analysis of faults play a very important role in reliable operation of electrical machines and are essential for major concerns such as efficiency and performance of applications involving PMSM drives. Sensor failure is one of several faults occurring in drive systems. Sensors are of great importance in the installation of monitoring and control systems. However, in most publications, detection of inverter faults or physical damage of the electrical machine is considered, rather than sensor faults. This paper proposes a method of phase current sensor fault detection and reconstruction for PMSM control systems.

In recent years, fault-tolerant control has been developed, which can be realized by reconstructing phase currents to substitute current feedback after the fault occurrence. For example, Lu et al. [2] reconstructed three-phase current based on DC bus sensors for fault-tolerant control for electric machines. Salmasi and Najafabadi [3] observed faulty phase stator currents based on an adaptive observer when there is only one normal phase current sensor. However, these designs do not separate fault signals from faulty sensors. Therefore, no further information can be obtained on the sensor state itself.

Due to the simplicity of the two-axis d-q-model, it has become the most widely used model in electric machine engineering controller design. The d-q-model offers significant convenience for control system design by transforming stationary symmetrical AC variables to DC variables in a rotating reference frame. Therefore, for electric machine sensor fault detection, the d-q axis currents, i_d and i_q, are assumed to be measured directly through sensors. Najafabadi et al. [4] detected d-q axis current sensor faults based on an adaptive observer. Liu [5] used a nonlinear parity relation method for detection of additive faults for virtual sensors for d-q

axis currents. Huang [6], an unknown input observer was designed for detection of q axis stator current residuals for induction motor. However, the two currents, i_d and i_q, are not practically measurable. These two virtual sensing signals are calculated from the measured phase current, i_{abc}, by applying a linear Clarke transformation. Abnormal changes in i_d and i_q may indicate a fault appearing in the phase current sensors, but this design will not provide more specific information. Furthermore, as the calculations of i_d and i_q are coupled, if a fault occurred in the measurement devices for i_{abc}, consequential faults in i_d and i_q will appear simultaneously. Hence, it is relatively difficult to detect the abnormal signals in the measurement devices for i_{abc}.

Sliding mode techniques are known for their robustness and insensitivity to the so-called matched uncertainty. Therefore these techniques offer great potential for robust fault detection and isolation (FDI) [7–10]. Faults are classified according to their physical locations into system, actuator, and sensor faults. Compared with actuators, sensors are passive elements in the sense that they only provide operational information about the system and do not affect the system behavior directly. Thus they have been less studied compared to actuator fault detection and isolation. This paper presents a method in which, using a newly designed filter, the sensor faults can be modeled as pseudoactuator faults. Then, using the transformed system structure and characteristics of the designed filter, a sliding mode observer is proposed to reconstruct the sensor fault in the system [11–13].

The paper is organized as follows. Section 2 describes a surface-mounted PMSM with current sensor faults. Section 3 proposes the method for reconstruction of faults. Section 4 presents simulation results and conclusions in Section 5 follow.

2. System Formulation

In the α-β rotor reference frame, a surface-mounted PMSM with current sensors faults can be expressed as the following dynamic model:

$$\begin{aligned} \dot{x}(t) &= Ax(t) + Bu(t) + E\psi, \\ y(t) &= Cx(t) + Nf_s(x,u,t), \end{aligned} \tag{1}$$

where $x(t)$, $u(t)$, $y(t)$, ψ, and $f_s(x,u,t)$ are the state variables, inputs, outputs, rotor flux, and sensor faults, respectively. Then the matrices are defined as

$$\begin{aligned} A &= \begin{bmatrix} -\dfrac{R_s}{L_\alpha} & 0 \\ 0 & -\dfrac{R_s}{L_\beta} \end{bmatrix}, \\ B &= \begin{bmatrix} \dfrac{1}{L_\alpha} & 0 \\ 0 & \dfrac{1}{L_\beta} \end{bmatrix}, \\ C &= \begin{bmatrix} 1 & 0 \\ 0 & 1 \end{bmatrix}, \\ E &= \begin{bmatrix} -\dfrac{\omega}{L_\alpha} & 0 \\ 0 & -\dfrac{\omega}{L_\beta} \end{bmatrix}, \\ N &= \begin{bmatrix} 1 & 0 \\ 0 & 1 \end{bmatrix}, \\ x &= \begin{bmatrix} i_\alpha \\ i_\beta \end{bmatrix}, \\ u &= \begin{bmatrix} u_\alpha \\ u_\beta \end{bmatrix}, \\ \psi &= \begin{bmatrix} \psi_\alpha \\ \psi_\beta \end{bmatrix} = \begin{bmatrix} -\psi_f \sin\theta_r \\ \psi_f \cos\theta_r \end{bmatrix}, \\ y &= \begin{bmatrix} i_\alpha \\ i_\beta \end{bmatrix}, \\ f_s &= \begin{bmatrix} f_{s\alpha} \\ f_{s\beta} \end{bmatrix} \end{aligned} \tag{2}$$

with

$$\begin{aligned} L_\alpha &= L_0 + L_1 \cos(2\theta_r), \\ L_\beta &= L_0 - L_1 \cos(2\theta_r), \\ L_0 &= \frac{L_d + L_q}{2}, \\ L_1 &= \frac{L_d - L_q}{2}, \end{aligned} \tag{3}$$

where i_α, i_β, u_α, and u_β are the α-β axis currents and voltages, respectively; ψ_f is the rotor permanent magnet flux linkage; θ_r is the electrical rotor angular position; ψ_α, ψ_β, $f_{s\alpha}$, and $f_{s\beta}$ are the α-β axis stator flux linkages and current sensor faults, respectively; R_s is the stator resistance; L_α, L_β, and ω are the α-β axis stator inductances and electrical rotor speed, respectively; and L_d and L_q are the stator d and q axis inductances, respectively. The surface-mounted PMSM stator winding shows the same electrical inductance on both d and q axes; that is, $L_d = L_q = L_s$, where L_s is the stator inductance.

3. Sensor Faults Reconstruction Based on Sliding Mode Variable Structure

The section proposes a novel method to reconstruct the phase current sensor faults for PMSM drives. Before dealing with the faults, an extended α-β axis fault model of PMSM is reformulated by using a transformation filter, which increases the system's state. Then, a sliding mode observer is constructed to

reconstruct α-β fault signals. A logic algorithm is built to convert the reconstructed α-β fault signal into *abc*-phase, so as to reconstruct phase current sensor faults.

3.1. Extended PMSM α-β Axis Fault Model and Sensor Faults Reconstruction. For system (1), a low-pass linear filter is introduced [11]:

$$\dot{z}(t) = A_s z(t) + B_s y, \tag{4}$$

where z is the new vector state; A_s and B_s are constant matrices, which are design parameters to be defined later; and y is the output.

Combining systems (1) and (4), we have

$$\dot{z}(t) = A_s z(t) + B_s C x(t) + B_s N f_s(x, u, t). \tag{5}$$

Then, the following augmented system can be obtained:

$$\begin{bmatrix} \dot{x} \\ \dot{z} \end{bmatrix} = \begin{bmatrix} A & 0 \\ B_s C & A_s \end{bmatrix} \begin{bmatrix} x \\ z \end{bmatrix} + \begin{bmatrix} B \\ 0 \end{bmatrix} u + \begin{bmatrix} 0 \\ B_s N \end{bmatrix} f_s + \begin{bmatrix} E \\ 0 \end{bmatrix} \psi,$$
$$z = \begin{bmatrix} 0 & I \end{bmatrix} \begin{bmatrix} x \\ z \end{bmatrix}, \tag{6}$$

where f_s is the sensor faults of system (1). The new state variables and matrices in a compatible way with system (6) are as follows:

$$\overline{A} = \begin{bmatrix} A & 0 \\ B_s C & A_s \end{bmatrix},$$
$$\overline{B} = \begin{bmatrix} B \\ 0 \end{bmatrix},$$
$$M = \begin{bmatrix} 0 \\ B_s N \end{bmatrix},$$
$$\overline{E} = \begin{bmatrix} E \\ 0 \end{bmatrix},$$
$$\overline{C} = \begin{bmatrix} 0 & I \end{bmatrix},$$
$$\overline{x}(t) = \begin{bmatrix} x(t) \\ z(t) \end{bmatrix},$$
$$\overline{y}(t) = z. \tag{7}$$

Therefore, following this transformation, the system is extended and the initial sensor fault problem has become an actuator fault problem. The corresponding extended fault model is

$$\dot{\overline{x}}(t) = \overline{A}\overline{x}(t) + \overline{B}u(t) + M f_s + \overline{E}\psi,$$
$$\overline{y}(t) = \overline{C}\overline{x}(t). \tag{8}$$

This paper focuses only on sensor faults, which have been transformed into pseudoactuator faults in system (8).

Assumption 1 ((A, C) is observable). When B_s is a nonsingular matrix, if (A, C) in system (1) is observable, $(\overline{A}, \overline{C})$ in system (8) will still be observable [14].

Therefore, there is a matrix L, which makes $A_0 = \overline{A} - L\overline{C}$ a stable matrix and satisfies the Lyapunov function:

$$A_0^T P + P A_0 = -Q, \tag{9}$$

where matrices P, Q are symmetric positive definite.

Assumption 2. There is a matrix F, such that $PM = \overline{C}^T F^T$.

Assumption 3. A fault in the system is a bounded function, such that $\|f_s\| \le \rho_1$, where ρ_1 is a selected scalar larger than 0.

The sliding mode observer for system (8) can be designed as

$$\dot{\hat{\overline{x}}}(t) = \overline{A}\hat{\overline{x}}(t) + \overline{B}u(t) + L\left(\overline{y}(t) - \overline{C}\hat{\overline{x}}(t)\right) + Mv + \overline{E}\psi,$$
$$\hat{\overline{y}}(t) = \overline{C}\hat{\overline{x}}(t), \tag{10}$$

where $\hat{\overline{x}}(t)$ and $\hat{\overline{y}}(t)$ are the estimated states and outputs, respectively, and v is the sliding mode signal, defined as

$$v = \begin{cases} -\rho \dfrac{F e_y(t)}{\left\| F e_y(t) \right\|} & \text{if } e_y \neq 0 \\ 0 & \text{if } e_y = 0, \end{cases} \tag{11}$$

where F is the observer gain and ρ is a positive scalar. Both of these need to be designed.

If the state estimation errors are defined as $e(t) = \hat{\overline{x}}(t) - \overline{x}(t)$ and $e_y(t) = \overline{C}\hat{\overline{x}}(t) - \overline{y}(t) = \overline{C}e(t)$, then from (8) and (10), the state estimation error dynamical system is

$$\dot{e}(t) = A_0 e(t) + M\left(v - f_s\right). \tag{12}$$

The convergence of the above observer is guaranteed by the following proposition.

Proposition 4. *Considering the system described by (8) and its observers described by (10), if Assumptions 1–3 hold, the parameter of the observer is selected according to the following criteria:*

$$\rho > \rho_1 \tag{13}$$

and thus e is asymptotically convergent; that is, $\lim_{t \to \infty} e(t) = 0$.

Proof. For system (12), consider a Lyapunov function candidate $V_1 = e^T P e$. The time derivative of V_1 along the trajectories of system (12) is

$$\dot{V}_1 = e^T \left(P A_0 + A_0 P\right) e + 2 e^T P M v - 2 e^T P M f_s \tag{14}$$

and it follows that

$$\begin{aligned}\dot{V}_1 &\le -e^T Qe + 2\left(F\overline{C}e\right)^T (v + f_s),\\ \dot{V}_1 &\le -e^T Qe - 2\left(Fe_y\right)^T \rho \frac{Fe_y}{\left\|Fe_y\right\|} + 2\left\|Fe_y\right\| \|f_s\|, \\ \dot{V}_1 &\le -e^T Qe - 2\left\|Fe_y\right\| (\rho - \|f_s\|).\end{aligned} \tag{15}$$

Then, under Assumption 3, the following can be obtained from (15):

$$\dot{V}_1 \le -e^T Qe - 2\left\|Fe_y\right\| (\rho - \rho_1) \le -e^T Qe, \tag{16}$$

from which $\dot{V}_1$ is negative definite. From the Lyapunov theorem, observer (10) is designed asymptotically stable.

It can be known from above that $e(t)$ will make asymptotic convergence to zero; that is, $\lim_{t\to\infty} e(t) = 0$.

This completes the proof. □

Proposition 4 implies that e is bounded; that is, t_0 exists, and when $t > t_0$,

$$\|e\| \le \delta_1, \tag{17}$$

where δ_1 is a finite positive scalar.

Remark 5. The obtained control algorithm of a sliding mode observer is simple and easy to implement. Because of the excellent robustness of the sliding mode variable techniques, the dependence on the precise mathematical model can be effectively reduced. The performance of the observer can be ensured in the case of a system modeling error, parameter perturbation, and the unknown inputs such as external noise and disturbance. Therefore, it has very strong engineering practicability.

Consider a sliding mode surface:

$$s = Fe_y(t). \tag{18}$$

Proposition 4 implies that the sliding mode dynamics of the error system (12) associated with the sliding surface (18) is stable. According to the sliding mode theory, observer stability will be guaranteed upon proving that the error system can be driven to the sliding mode surface in finite time by choosing an appropriate gain of ρ for the input signals (11). In view of this, the conclusion is presented by the following proposition.

Proposition 6. *If Assumptions 1–3 hold and ρ is sufficiently large, then the error system (12) will be driven to the sliding mode surface in finite time.*

Proof. Selecting the Lyapunov function

$$V_2 = \frac{1}{2} s^T s, \tag{19}$$

then the time derivative of V_2 along the trajectories of system (12) is

$$\begin{aligned}\dot{V}_2 &= s^T\left(F\overline{C}\dot{e}\right) = s^T F\overline{C}\left(A_0 e + M(v - f_s)\right)\\ &= s^T F\overline{C}A_0 e + s^T F\overline{C}M(v - f_s)\\ &= s^T F\overline{C}A_0 e + s^T M^T PM(v - f_s)\\ &= s^T F\overline{C}A_0 e - s^T M^T PMf_s + s^T M^T PMv\\ &= s^T F\overline{C}A_0 e - s^T M^T PMf_s - \rho s^T M^T PM\frac{s}{\|s\|}.\end{aligned} \tag{20}$$

Thus, from (17), there is

$$\begin{aligned}\dot{V}_2 &\le \|s\|\left\|F\overline{C}A_0\right\|\|e\| + \|s\|\left\|M^T PM\right\|\|f_s\|\\ &\quad - \rho\lambda_{\min}\left(M^T PM\right)\|s\| \le \|s\|\left(\left\|F\overline{C}A_0\right\|\delta_1\right.\\ &\quad \left. + \left\|M^T PM\right\|\|f_s\| - \rho\lambda_{\min}\left(M^T PM\right)\right) \le -\|s\|\\ &\quad \cdot \lambda_{\min}\left(M^T PM\right)\left(\rho\right.\\ &\quad \left. - \left(\frac{\left\|M^T PM\right\|}{\lambda_{\min}\left(M^T PM\right)}\|f_s\| + \frac{\left\|F\overline{C}A_0\right\|}{\lambda_{\min}\left(M^T PM\right)}\delta_1\right)\right).\end{aligned} \tag{21}$$

The variables can be defined as

$$\begin{aligned}K &= \lambda_{\min}\left(M^T PM\right)\left(\rho\right.\\ &\quad \left. - \left(\frac{\left\|M^T PM\right\|}{\lambda_{\min}\left(M^T PM\right)}\|f_s\| + \frac{\left\|F\overline{C}A_0\right\|}{\lambda_{\min}\left(M^T PM\right)}\delta_1\right)\right).\end{aligned} \tag{22}$$

Since $\|M^T PM\| \ge \lambda_{\min}(M^T PM) > 0$, it follows that $(\|M^T PM\|/\lambda_{\min}(M^T PM))\|f_s\| + (\|F\overline{C}A_0\|/\lambda_{\min}(M^T PM))\delta_1 \ge \|f_s\|$. So the scalar ρ in (11) satisfies $\rho > \rho_1$, and ρ can be selected to be large enough to satisfy

$$\rho \ge \frac{\left\|M^T PM\right\|}{\lambda_{\min}\left(M^T PM\right)}\rho_1 + \frac{\left\|F\overline{C}A_0\right\|}{\lambda_{\min}\left(M^T PM\right)}\delta_1; \tag{23}$$

then

$$\dot{V}_2 \le -K\|s\|. \tag{24}$$

This shows that the sliding mode reachability condition is satisfied. As a consequence, according to sliding mode principle [15], an ideal sliding motion will take place on the surface s after some finite time.

This completes the proof. □

When the system reaches the sliding mode surface, $s = \dot{s} = 0$ according to the sliding mode equivalent principle [9]. This implies

$$\begin{aligned}F\overline{C}e(t) = Fe_y(t) = 0,\\ F\overline{C}\dot{e} = F\dot{e}_y(t) = Fe_y(t) = 0\end{aligned} \tag{25}$$

and, from (12) and (25), the fault reconstruction equation can be got in the form of

$$f_s = v; \tag{26}$$

that is, the fault is now equivalent to the sliding mode signal.

Remark 7. Unlike many other methods which use residuals to diagnose the occurrence of sensor fault qualitatively, the method of fault reconstruction presented in this paper estimates the current sensor fault quantitatively. By this way, not only the original appearance of a fault can be reflected vividly, but also more specific fault information can be obtained. It actually becomes the important basis of adopting more targeted measures to eliminate the effect of fault on PMSM drives or achieving the active fault-tolerant control proposal as presented in this paper.

3.2. Reconstructing the Phase Current Sensors Fault Signals. As mentioned previously, a fault on one of the α-β axis current sensors can be reconstructed. But this design will not provide more specific information whether the faulty sensor is in phase "*a*" or "*b*." Therefore, the phase current sensor fault isolation and identification become somewhat complicated. To overcome this problem, a logic algorithm is constructed, devoted to transforming the α-β axis fault signals in *abc*-phase fault signals of PMSM. Thus, the phase current sensor faults will be reconstructed.

Generally, for electric motors, only two phase sensors are used. That is based on considerations of cost and the fact that the three phase currents make a vector sum to zero in a star connected system without a neutral line. So, in actual control systems of PMSM, the two phase stator currents, i_a and i_b, are measured by the phase current sensors, respectively, and the third phase current, i_c, is calculated using $i_a + i_b + i_c = 0$.

A linear (3/2) Clarke transformation is applied to transform the three-phase plane coordinate system *ABC* to the two-phase plane rectangular coordinate system $\alpha\beta$, the transformation equation is as below:

$$\begin{bmatrix} i_\alpha \\ i_\beta \\ i_0 \end{bmatrix} = \sqrt{\frac{2}{3}} \begin{bmatrix} 1 & -\frac{1}{2} & -\frac{1}{2} \\ 0 & \frac{\sqrt{3}}{2} & -\frac{\sqrt{3}}{2} \\ \frac{1}{\sqrt{2}} & \frac{1}{\sqrt{2}} & \frac{1}{\sqrt{2}} \end{bmatrix} \begin{bmatrix} i_a \\ i_b \\ i_c \end{bmatrix}, \tag{27}$$

where i_0 is a variable introduced, distinct from i_a and i_b, used for construction of the α-β-0 coordinate system, called the zero-axis current. The zero-axis is vertical to both α and β axes, and so it will have no influence on α and β axes.

For star connected systems without a neutral line, $i_a + i_b + i_c = 0$; that is, $i_c = -(i_a + i_b)$. Equation (27) becomes

$$\begin{bmatrix} i_\alpha \\ i_\beta \end{bmatrix} = \begin{bmatrix} \sqrt{\frac{3}{2}} & 0 \\ \frac{\sqrt{2}}{2} & \sqrt{2} \end{bmatrix} \begin{bmatrix} i_a \\ i_b \end{bmatrix}. \tag{28}$$

It can be seen that decoupling can be realized for current in this equation.

As discussed above, practically, currents i_α and i_β are calculated from phase currents i_a and i_b. Then, from (28), the effects of the stator α-β axis currents are related to the errors in phase *a* and *b* current sensors outputs:

$$\begin{bmatrix} i_\alpha + f_{s\alpha} \\ i_\beta + f_{s\beta} \end{bmatrix} = \begin{bmatrix} \sqrt{\frac{3}{2}} & 0 \\ \frac{\sqrt{2}}{2} & \sqrt{2} \end{bmatrix} \begin{bmatrix} i_a + f_{sa} \\ i_b + f_{sb} \end{bmatrix}, \tag{29}$$

where $f_{s\alpha}$ and $f_{s\beta}$ are the α-β axis sensor faults, respectively, and f_{sa} and f_{sb} are the *a* and *b* phase sensor faults, respectively.

From (28) and (29), the phase sensor faults f_{sa} and f_{sb} are

$$\begin{aligned} f_{sa} &= \sqrt{\frac{2}{3}} f_{s\alpha}, \\ f_{sb} &= \frac{1}{\sqrt{2}} f_{s\beta} - \sqrt{\frac{1}{6}} f_{s\alpha}, \end{aligned} \tag{30}$$

where $f_{s\alpha}$, $f_{s\beta}$ are derived by reconstruction of the state observer in the previous section.

In addition, the actual phase current is

$$\begin{aligned} i_a &= \sqrt{\frac{2}{3}} i_\alpha, \\ i_b &= \frac{1}{\sqrt{2}} i_\beta - \sqrt{\frac{1}{6}} i_\alpha. \end{aligned} \tag{31}$$

Thus, the phase current sensor fault signals can be reconstructed by transformation of the α-β axis fault signals of a PMSM.

Remark 8. In the previous literature [5, 6], the current sensor fault detection was usually corresponding to *d*-*q* axis, which is a virtual axis. In contrast, this paper proposes a new current sensor FDI algorithm which is directly corresponding to *abc*-phase, the actual mounting position of current sensor. This innovation can significantly improve the practicability of traditional FDI algorithm, as well as bring many potential applications.

4. Simulation Study

To verify the effectiveness of the method proposed in this paper, the drive tests with respect to two types of faults have been carried out. One tested fault is the incipient fault and the other is the gain sensor fault. The parameters for the PMSM of this study are given in Table 1.

The matrixes A_s and B_s in (4) are then

$$\begin{aligned} A_s &= \begin{bmatrix} -200 & 0 \\ 0 & -200 \end{bmatrix}, \\ B_s &= \begin{bmatrix} 200 & 0 \\ 0 & 200 \end{bmatrix}. \end{aligned} \tag{32}$$

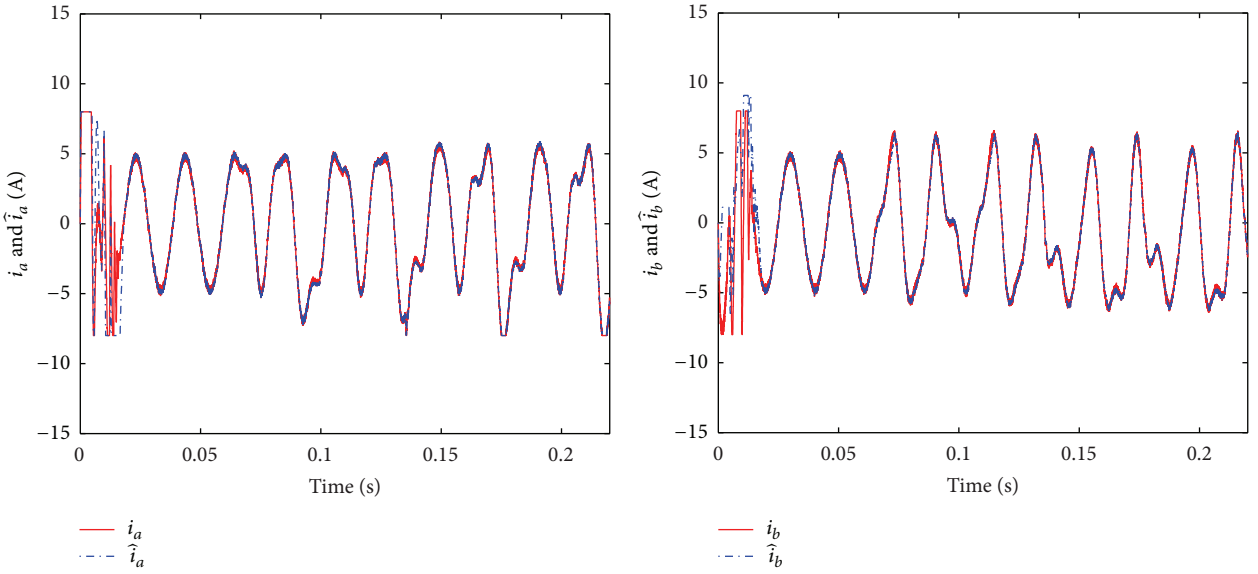

(a) i_a and its estimation $\hat{i}_a$

(b) i_b and its estimation $\hat{i}_b$

Figure 1: Case 1: current estimation.

Table 1: Nominal value for PMSM.

Parameters	Unit	Values
Stator resistance (R_s)	Ω	2.875
Number of pole pairs (n_p)	Pairs	4
Stator inductance (L_s)	H	0.0085
Rotor PM flux (ψ_f)	Wb	0.175
Rotor moment of inertia (J)	kg·m^2	0.008

The matrixes in system (8) are

$$\bar{A} = \begin{bmatrix} -338.23 & 0 & 0 & 0 \\ 0 & -338.23 & 0 & 0 \\ 200 & 0 & -200 & 0 \\ 0 & 200 & 0 & -200 \end{bmatrix},$$

$$\bar{B} = \begin{bmatrix} 117.65 & 0 \\ 0 & 117.65 \\ 0 & 0 \\ 0 & 0 \end{bmatrix},$$

$$\bar{C} = \begin{bmatrix} 0 & 0 & 1 & 0 \\ 0 & 0 & 0 & 1 \end{bmatrix},$$

$$\bar{E} = \begin{bmatrix} -117.65\omega & 0 \\ 0 & -117.65\omega \\ 0 & 0 \\ 0 & 0 \end{bmatrix},$$

$$M = \begin{bmatrix} 0 & 0 \\ 0 & 0 \\ 200 & 0 \\ 0 & 200 \end{bmatrix} \tag{33}$$

and matrix $(\bar{A}, \bar{C})$ is observable since B_s is nonsingular.

The matrix L in (10) is

$$L = \begin{bmatrix} 100 & 0 & 200 & 0 \\ 0 & 100 & 0 & 100 \end{bmatrix}^T. \tag{34}$$

And so the corresponding A_0 matrix is

$$A_0 = \begin{bmatrix} -338.23 & 0 & -100 & 0 \\ 0 & -338,23 & 0 & -100 \\ 200 & 0 & -400 & 0 \\ 0 & 200 & 0 & -100 \end{bmatrix}, \tag{35}$$

and, using linear matrix inequality techniques, we have the following solution:

$$P = \begin{bmatrix} 724.4 & 0 & 0 & 0 \\ 0 & 759.5 & 0 & 0 \\ 0 & 0 & 567.4 & 0 \\ 0 & 0 & 0 & 745.5 \end{bmatrix},$$

$$F = \begin{bmatrix} 113480 & 0 \\ 0 & 149100 \end{bmatrix}. \tag{36}$$

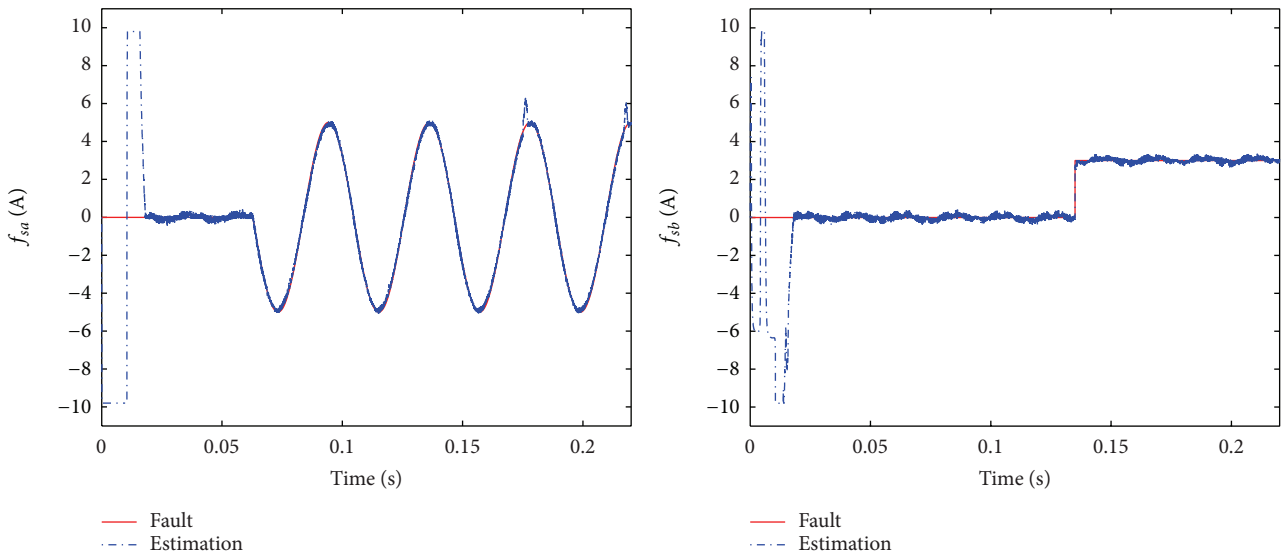

(a) The fault f_{sa} and its estimation

(b) The fault f_{sb} and its estimation

FIGURE 2: Case 1: current sensor faults estimation.

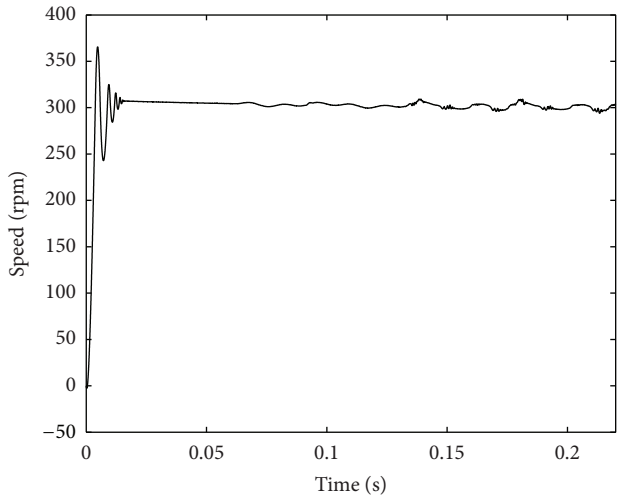

FIGURE 3: Case 1: the motor speed waveform during current sensor faults on a and b phases.

Remark 9. The following saturation function can be used to substitute for the sliding mode signal v to reduce chattering and eliminate high-frequency interference caused by the chattering:

$$v = -\rho \frac{Fe_y}{\left\| Fe_y \right\| + \delta_2}, \tag{37}$$

where δ_2 is a scalar of relatively small value.

The following parameters are chosen: $\rho = 46$, $\delta_2 = 0.1$; initial simulation conditions are all 5 A; output limiting values of state variable are chosen as ±10 A; fault reconstruction limiting values are chosen as ±7 A; simulation time is 0.22 s; and the given speed is 300 rpm.

Case 1. A sinusoidal signal is added with amplitude 5 A and frequency 150 Hz for a-phase from 0.063 s, simulating an incipient fault; and a step signal with amplitude 3 A from 0.135 s for b-phase, simulating a gain sensor fault.

The simulation (Figures 1-2) shows that the fault signals can be accurately reconstructed. The faults produce motor speed abnormalities in the drive's operation, as shown in Figure 3.

Case 2. A step signal is added with amplitude 5 A from 0.063 s for a-phase, simulating a gain sensor fault; and a sinusoidal signal with amplitude 3 A and frequency 150 Hz for b-phase from 0.135 s, simulating an incipient fault.

The simulation (Figures 4-5) shows that the fault signals can be accurately reconstructed. The faults produced motor

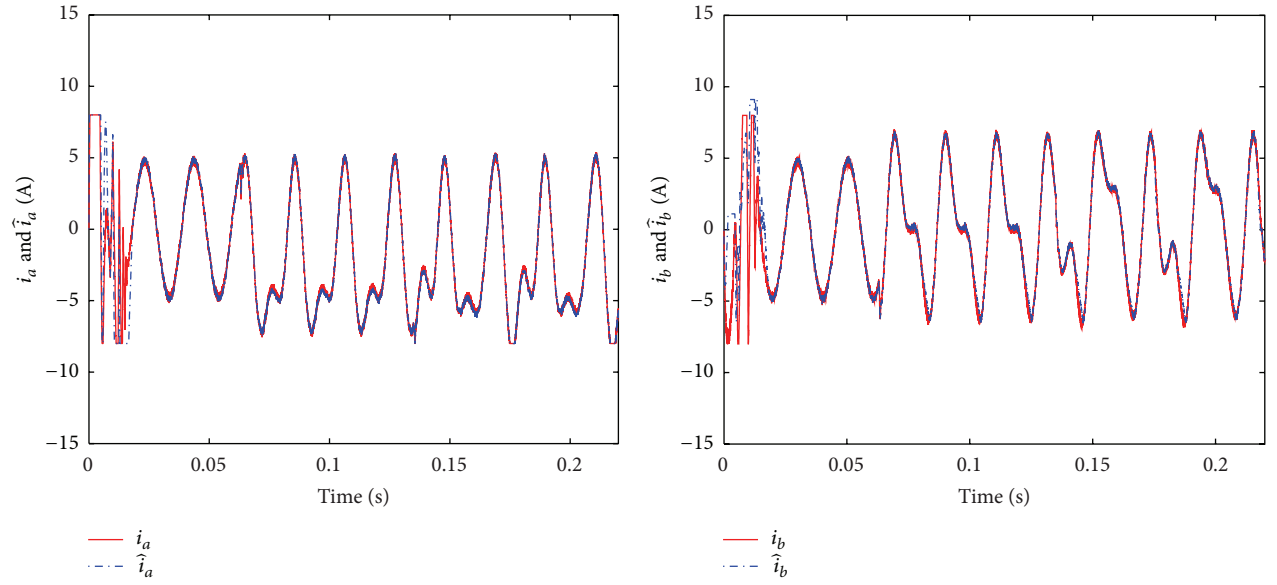

(a) i_a and its estimation $\hat{i}_a$ (b) i_b and its estimation $\hat{i}_b$

FIGURE 4: Case 2: current estimation.

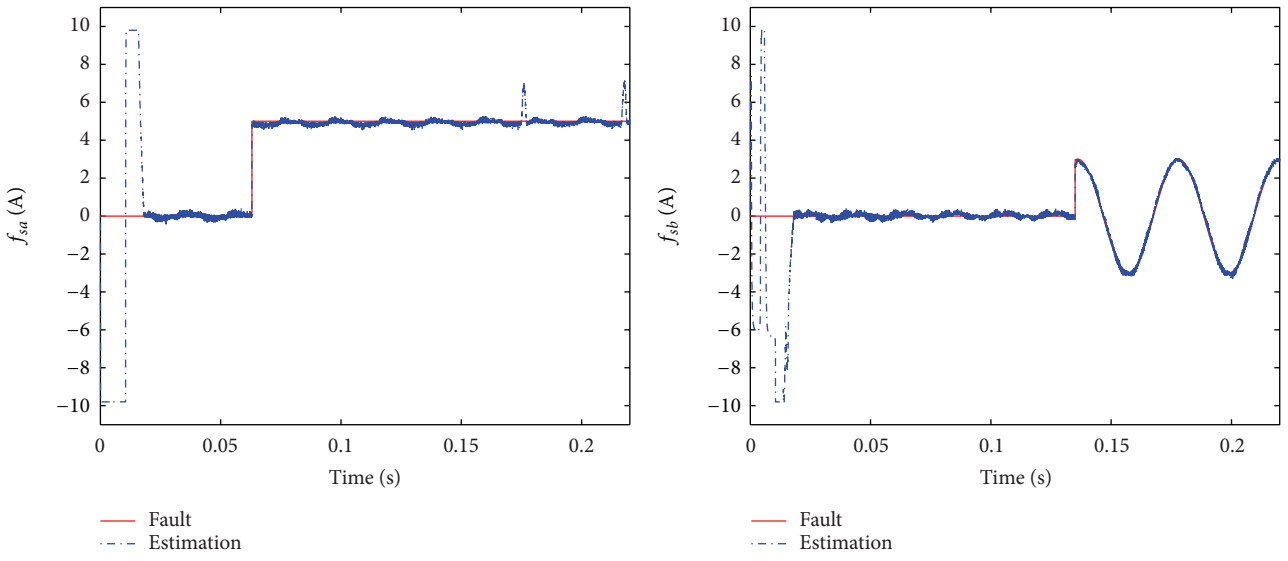

(a) The fault f_{sa} and its estimation (b) The fault f_{sb} and its estimation

FIGURE 5: Case 2: current sensor faults estimation.

speed abnormalities in the drive's operation, as shown in Figure 6.

The simulations show that the fault reconstruction is realized. The fault signal can be estimated to determine the size, location, and time of occurrence of a fault on phase a or b current sensor of a PMSM intuitively. This method will be ideal for directly isolating the faulty current sensor.

5. Conclusions

This paper presents a PMSM phase current sensor fault reconstruction method based on sliding mode variable structure observer. An α-β axis fault model of PMSM is firstly defined. Based on this, a first-order low-pass filter is introduced for constructing an augmented system with which the PMSM sensor faults can be considered as actuator faults.

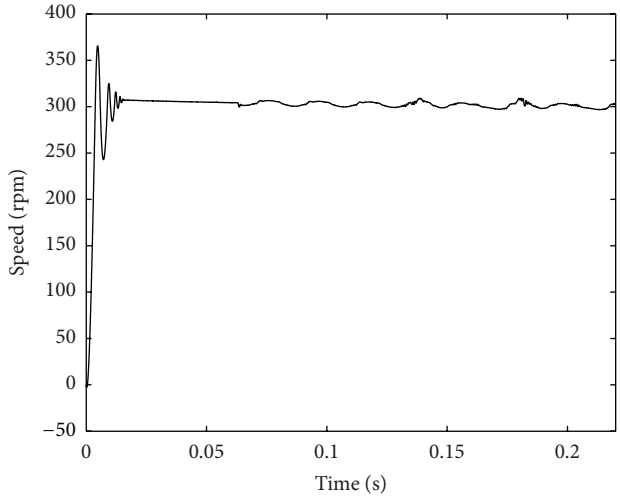

Figure 6: Case 2: the motor speed waveform during current sensor faults on a and b phases.

The design of a sliding mode variable structure observer follows to achieve fault reconstruction by using sliding mode equivalent principle. Then it comes to the design of logic algorithm, with which the reconstructed α-β axis fault signal can be converted into abc-phase, and then the detection and reconstruction of actual fault of phase current sensor can be implemented. It can be seen from the proof and simulation results that, with the proposed fault reconstruction scheme, there is almost no restriction on the fault type. In other words, the scheme is applicable for abrupt fault, incipient fault, or any other types of faults.

Conflict of Interests

The authors declare that there is no conflict of interests regarding the publication of this paper.

Acknowledgments

This work was supported by the Natural Science Foundation of China (nos. 61273157 and 61473117), Hunan Provincial Natural Science Foundation of China (nos. 14JJ5024 and 2015JJ5011), and Hunan Province Education Department Project of China (nos. 12A040 and 13CY018).

References

[1] I. Aydin, M. Karakose, and E. Akin, "An approach for automated fault diagnosis based on a fuzzy decision tree and boundary analysis of a reconstructed phase space," *ISA Transactions*, vol. 53, no. 2, pp. 220–229, 2014.

[2] H. Lu, X. Cheng, W. Qu, S. Sheng, Y. Li, and Z. Wang, "A three-phase current reconstruction technique using single DC current sensor based on TSPWM," *IEEE Transactions on Power Electronics*, vol. 29, no. 3, pp. 1542–1550, 2014.

[3] F. R. Salmasi and T. A. Najafabadi, "An adaptive observer with online rotor and stator resistance estimation for induction motors with one phase current sensor," *IEEE Transactions on Energy Conversion*, vol. 26, no. 3, pp. 959–966, 2011.

[4] T. A. Najafabadi, F. R. Salmasi, and P. Jabehdar-Maralani, "Detection and isolation of speed-, DC-link voltage-, and current-sensor faults based on an adaptive observer in induction-motor drives," *IEEE Transactions on Industrial Electronics*, vol. 58, no. 5, pp. 1662–1672, 2011.

[5] L. Liu, *Robust fault detection and diagnosis for permanent magnet synchronous motors [A Thesis Presented for the Degree of Doctor of Philosophy]*, The Florida State University, Summer Semester, 2006.

[6] Y. Huang, *Fault diagnosis method based on observer and application research [M.S. thesis]*, The Hunan University of Technology, Summer Semester, 2011.

[7] A. Šabanovic, "Variable structure systems with sliding modes in motion control—a survey," *IEEE Transactions on Industrial Informatics*, vol. 7, no. 2, pp. 212–223, 2011.

[8] Z. Gao, B. Jiang, P. Shi, M. Qian, and J. Lin, "Active fault tolerant control design for reusable launch vehicle using adaptive sliding mode technique," *Journal of the Franklin Institute*, vol. 349, no. 4, pp. 1543–1560, 2012.

[9] B. Jiang, M. Staroswiecki, and V. Cocquempot, "Fault estimation in nonlinear uncertain systems using robust/sliding-mode observers," *IEE Proceedings: Control Theory and Applications*, vol. 151, no. 1, pp. 29–37, 2004.

[10] C. Edwards, S. K. Spurgeon, and R. J. Patton, "Sliding mode observers for fault detection and isolation," *Automatica*, vol. 36, no. 4, pp. 541–553, 2000.

[11] C. P. Tan and C. Edwards, "Sliding mode observers for detection and reconstruction of sensor faults," *Automatica*, vol. 38, no. 10, pp. 1815–1821, 2002.

[12] H. K. Khalil, *Nonlinear Systems*, Prentice-Hall, Englewood Cliffs, NJ, USA, 3rd edition, 2002.

[13] X.-G. Yan and C. Edwards, "Sensor fault detection and isolation for nonlinear systems based on a sliding mode observer," *International Journal of Adaptive Control and Signal Processing*, vol. 21, no. 8-9, pp. 657–673, 2007.

[14] J. He, J. Qiu, and C. Zhang, "A multiple fault diagnosis method based on sliding mode observer," *Journal of Dynamics and Control*, vol. 7, no. 1, pp. 84–91, 2009.

[15] F. Y. Wang, *Sliding Mode Variable Structure Control*, Tsinghua University Press, Beijing, China, 2005.

Hindawi Publishing Corporation
Journal of Sensors
Volume 2016, Article ID 6139802, 8 pages
http://dx.doi.org/10.1155/2016/6139802

Research Article

Detection of Defective Sensors in Phased Array Using Compressed Sensing and Hybrid Genetic Algorithm

Shafqat Ullah Khan,[1] Ijaz Mansoor Qureshi,[2] Aqdas Naveed,[3] Bilal Shoaib,[3] and Abdul Basit[3]

[1]*School of Engineering & Applied Sciences, ISRA University, Islamabad 44000, Pakistan*
[2]*Electrical Department, Air University, Islamabad 44000, Pakistan*
[3]*Electronic Department, International Islamic University, Islamabad 44000, Pakistan*

Correspondence should be addressed to Shafqat Ullah Khan; shafqatphy@yahoo.com

Received 3 February 2015; Revised 12 June 2015; Accepted 14 July 2015

Academic Editor: Manuel Pineda-Sanchez

A compressed sensing based array diagnosis technique has been presented. This technique starts from collecting the measurements of the far-field pattern. The system linking the difference between the field measured using the healthy reference array and the field radiated by the array under test is solved using a genetic algorithm (GA), parallel coordinate descent (PCD) algorithm, and then a hybridized GA with PCD algorithm. These algorithms are applied for fully and partially defective antenna arrays. The simulation results indicate that the proposed hybrid algorithm outperforms in terms of localization of element failure with a small number of measurements. In the proposed algorithm, the slow and early convergence of GA has been avoided by combining it with PCD algorithm. It has been shown that the hybrid GA-PCD algorithm provides an accurate diagnosis of fully and partially defective sensors as compared to GA or PCD alone. Different simulations have been provided to validate the performance of the designed algorithms in diversified scenarios.

1. Introduction

Nowadays array testing is of great interest in the research community. Moreover, the estimation of the power pattern and detection of faulty sensors in antenna arrays are an important issue in radar, remote sensing, and mobile and satellite communications [1–3]. There is a possibility of getting one or more antenna elements defective which results in degradation of radiation pattern of the array [4–6]. Prior to the correction of the patterns, it is necessary to first diagnose the defective antenna element in the array. Several traditional techniques are available to detect the number and the positions of faulty elements from the observation of healthy array and damaged power pattern [7, 8]. The most commonly used techniques for array detection are matrix method [9], back propagation algorithm [10], and exhaustive searches [11]. However, these techniques are computationally expensive as they require that the number of measurements should not be less than the number of antenna elements in the array.

In array diagnosis, the purpose is to locate the faulty elements in linear array. The sparse vector is defined as the deviation between the weights of the healthy reference array and the array under test [12]. In practical scenario, the number of defective elements is small. Thus the new array is very sparse with a small number of active elements, allowing a less number of measurements for the detection of faulty elements. The failure detection problem using the recovery techniques of signals in compressed sensing allows the harmonic estimation of sparse signals using a small number of data [13, 14]. The measurement matrix must satisfy the restricted isometry property to avoid information in the actual signal from distortion. In such a framework, an inventive turnup for the detection of defective linear arrays from far-field measurement has been proposed [15] enchanting the benefit of the compressed sensing technique.

Compressed sensing (CS) is a signal processing technique, in which one can recover a signal from a set of linear measurements instead of a signal itself, where the number of

the measurements is less than the signal. As a consequence, the original signal has to be recovered from the measurement matrix, which is ill-posed due to the reduced dimension. CS technique [16–19] states that it possible to recover the underlying signal from less number of measurements below the Nyquist sampling rate, under the suitable conditions such as restricted isometry property (RIP). In literature several techniques are available for solving the ill-posed recovery problem. These techniques can be classified into a number of algorithm families with their problem varying approach [20–22].

Among the researchers in engineering, GA and PCD algorithm have required special attention. GA is bioinspired technique that has been used successfully for different optimization problems in numerous fields of engineering [23–25]. On the other hand, PCD, with the idea taken from coordinate descent method, is also used for different minimization problems.

In this paper, taking into account the promising performance of GA and PCD, we have introduced a CS based array diagnosis technique. This technique is based on the measurement data of the far-field pattern. The system relating the difference between the field measured using the healthy reference array and the field radiated by the array under test is solved using GA, PCD algorithm, and GA hybridized with PCD algorithm. The major advantage of this hybrid technique is the avoidance of slow and early convergence of GA. The performances of all of these algorithms have been compared with each other in terms of convergence and mean square error (MSE). The GA-PCD algorithm provides an accurate diagnosis of fully and partially defective sensors as compared to the individual GA or PCD algorithm alone. Different simulations have been provided to validate the performance of the designed algorithms.

The remaining of paper is organized as follows. The problem formulation is discussed in Section 2, while in Section 3, we have designed GA, PCD, and hybrid GA-PCD. Section 4 describes the simulations and results, while Section 5 concludes the work and recommends some future directions.

2. Problem Formulation

Let us consider a linear array of N elements along z-axis, whose far-field patterns are given as [1]

$$A(\theta_i) = \sum_{n=1}^{N} w_n \cos\left[\left(\frac{2n-1}{2}\right) kd \sin\theta_i\right], \quad (1)$$

where w_n is the weight vector of the nth antenna element, k is the wave number, i is the ith measurement pattern, and d is the distance between the consecutive elements. The noisy far-field pattern of the array under test is expressed as

$$F_m(\theta_i) = \sum_{\substack{n=1 \\ n\neq m}}^{N} a_n \cos\left[\left(\frac{2n-1}{2}\right) kd \sin\theta_i\right] + r(\theta_i), \quad (2)$$

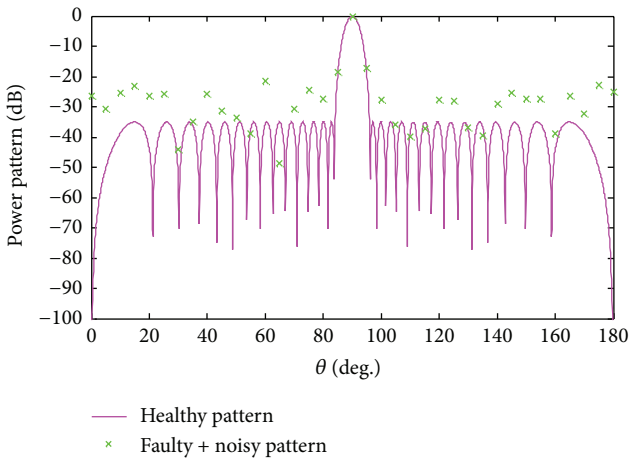

FIGURE 1: The Chebyshev healthy and noisy faulty pattern with $N = 30$ and SLL = −35 dB.

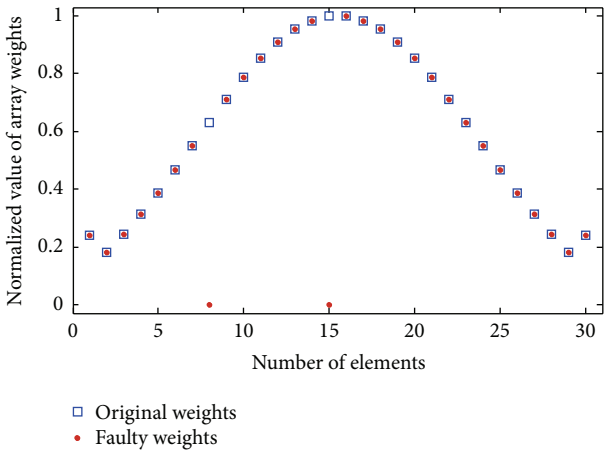

FIGURE 2: The Chebyshev healthy and faulty (8th and 15th) weights with $N = 30$ and SLL = −35 dB.

where $r(\theta_i)$ is the ith sample of an additive zero mean complex Gaussian noise with variance σ and a_n is the nth weight vector of the array under test. In (2), a_n is given as

$$a_n = \begin{cases} 0 & \text{with propability } \phi \\ w_n & \text{otherwise,} \end{cases} \quad (3)$$

where $\phi < 1$ is the fraction of faulty elements. The original and noisy faulty Chebyshev power pattern with $N = 30$ and SLL = −35 dB are shown in Figure 1. The normalized Chebyshev weights of the original and faulty array with 8th and 15th elements not working are depicted in Figure 2. The difference field pattern between the ideal and the array under test is given [11] by the following equation:

$$p(\theta_i) = A(\theta_i) - F_m(\theta_i) \quad (4)$$

or it can be written as follows:

$$p(\theta_i) = \sum_{n=1}^{N} x_n \cos\left[\left(\frac{2n-1}{2}\right) kd \sin\theta_i\right] - r(\theta_i), \quad (5)$$

where $\mathbf{p} = \{p(\theta_i),\ i = 1, 2, 3, \ldots, K\}$ and x_n is the nth element of the array under test failure vector which is given by

$$x_n = w_n - a_n. \tag{6}$$

To solve the array detection problem, we find x_n. In practical scenario, some element failure occurs; thus the failure vector turns out to be sparse. The array detection problem can be reformulated in sparseness frame work [13]. Given the difference vector $\mathbf{p}$ find the minimum l_0 norm that satisfies the equation

$$\mathbf{p} - \mathbf{Ex} = \mathbf{r}$$

$$\mathbf{E} = \begin{bmatrix} \exp\left(jnkd\sin\theta_1\right) & \cdots & \exp\left(jNkd\sin\theta_1\right) \\ \vdots & \ddots & \vdots \\ \exp\left(jnkd\sin\theta_K\right) & \cdots & \exp\left(jN\sin\theta_K\right) \end{bmatrix}, \tag{7}$$

where $\mathbf{E}$ is the measurement matrix [14]. Given the difference vector and the measurement matrix, the algorithm looks for the finest solution of inverse problem under a definite constraint. If the measurement matrix is square and invertible then the unique solution can be found through matrix inversion. In practical scenario, the measurement matrix is ill-conditioned, which leads to underdetermined system of linear equations. Thus we find the sparsest solution.

3. Proposed Methodology

In compressed sensing (CS), sparsity in signals allows us to undersample the signal below the Nyquist minimum sampling criterion. In CS, less number of measurements in sparse signal contains complete information compared to its dimensions, so that exact recovery from less number of measurements is possible [16, 17]. CS has many applications, that is, communications and Magnetic Resonance Imaging (MRI) [15, 18]. Restricted isometry property (RIP) should be fulfilled by measurement matrix to avoid information in the actual signal from distortion, such as Gaussian matrices. For the exact recovery, the number of measurements taken is; that is, $m \geq S\log(N/S)$, where m measurements are taken from a signal of length N having S defective elements; then sparse signal could be recovered with high probability [20]. The minimum l_2 norm based solution minimizes the total energy of the approximated signal and has a unique solution. However, solution is generally nonsparse. l_0 norm minimization makes use of sparsity constraint for finding an estimate of solution with few defective elements in linear array. However, it has nonconvex formulation for finding the sparse solution and is computationally intractable as it involves an exhaustive search $\binom{N}{S}$ for defective elements.

There is temptation for l_2 norm minimization given in (8) due to its unique solution and because it is computationally tractable. Consider

$$\widehat{x} = \arg\min_x \left\| p - Ex \right\|_2^2. \tag{8}$$

Sparse approximation problems such as l_0 minimization in (9) use the sparsity constraint as a regularizer to find an approximate solution with few defective elements in the antenna array. One has

$$\widehat{x} = \arg\min_x \left\| p - Ex \right\|_2^2 \quad \text{subject to} \quad \|x\|_0 \leq S. \tag{9}$$

The l_1 norm is convex and promotes sparsity in solution, whereas, l_0 norm in (9) is generally not tractable and nonconvex. Thereby, we can replace l_0 norm by l_1 norm to remodel the problem in (9) by

$$\widehat{x} = \arg\min_x \left(\left\| p - Ex \right\|_2^2 + \|x\|_1 \right). \tag{10}$$

3.1. Genetic Algorithm (GA). GA is a nature inspired metaheuristic optimization technique which is based on the ideology of inheritance. The algorithm starts with the initialization of chromosomes. Each chromosome in the inhabitants acts as a candidate solution. The elements of a chromosome are called genes. The price of each chromosome is determined through a fitness function. With the help of crossover, the genes of different chromosomes can be combined in a variety of ways to produce the offspring having different fitness values. The new population is formed with the normal selection by combining the best parents and offspring. In this way the GA proceeds to search for the best candidate solution. Nature inspired metaheuristic algorithms are preferred for the problems which are NP-hard. When the optimization involves constraints the application of GA [23] becomes more difficult as the crossovers are blind to the constraints.

Constraints can be included in the fitness function as well as in the chromosome. However indirect constraint usage does not work well for the sparse problems. In our proposed algorithm the constraint is used to guarantee the preferred sparsity level before and after the crossover during hard thresholding. One of the main problems in GA is the early convergence which is linked to the loss of inherited variety of the population. To avoid this problem we pass through the mutation process. However for sparse signal recovery the ordinary mutation will not work, making the chromosome denser and compromising the sparsity constraint. The proposed algorithm avoids this problem by using the PCD algorithm when the population tends to converge prematurely.

3.2. Parallel Coordinate Descent Algorithm (PCD). PCD is an algorithm that minimizes the function. The idea of PCD is taken from the coordinate descent method in which the fitness function minimizes one coordinate at a time [20]. In order to get the new solution, it updates all the coefficients in parallel instead of doing it sequentially. The update equation of the algorithm is given by

$$x_{k+1} = x_k + \mu\left(e_s - x_k\right), \tag{11}$$

where μ is a constant and is computed through line search. In the proposed algorithm we replace it with a random number. The starting value of the solution can be either an estimate of

the least square solution or a zero vector. In (11) the term e_s is computed by the following expression:

$$e_s = \left(x_k + \operatorname{diag}\left(E^T E\right)^{-1} E^T r_k\right). \tag{12}$$

Here $r_k = p - Ex_k$ is the residue. The pseudocode of PCD is given as follows.

The Pseudo Code of Parallel Coordinate Decent (PCD) Algorithm

Task. Find the value of **x**.

Input. The inputs are measurement matrix **E** and compressed measurement **p**.

Output. The output is the result of **x**.

Initialization. Initialize $k = 0$ and set the following:

The initial solution $x_0 = 0$.

The initial residual $r_0 = b - Ex_0 = b$.

Prepare the weights $Q = \operatorname{diag}(E^T E)^{-1}$.

Main Iteration. Increment k by 1, and apply these steps: that is, $k = k + 1$.

Back Projection. Compute $e = E^T r_k$.

Shrinkage. Compute $e_s = \operatorname{shrink}(x_k + Qe)$.

Line Search. Choose μ to minimize the real value function $f(x_k + \mu(e_s - x_k))$.

Update Solution. Compute $x_k + \mu(e_s - x_k)$.

Update Residual. Compute $r_{k+1} = b - Ex_{k+1}$.

Stopping Rule. If $\|x_{k+1} - x_k\|_2^2$ is smaller than some predetermined threshold, stop, or else apply another iteration.

Output. Result is x_{k+1}.

The proposed algorithm modifies the regular PCD to accelerate the convergence of GA. In order for PCD to interact with GA, randomness is introduced in it at various levels. PCD is used to update chromosome when the fitness of the best chromosome does not change in a few consecutive iterations thereby preventing the convergence issue. The interaction of PCD in the proposed algorithm is a random phenomenon. PCD algorithm each time is accessed by GA. The residue is computed using the current best chromosome while in (11) and (12) a chromosome from the current generation is selected randomly to replace r_{k-1}.

3.3. Hybrid Genetic Algorithm. The flow chart of the proposed hybrid GA with PCD algorithm is shown in Figure 3 while its pseudopod is given as follows.

The Pseudo Code of Hybrid GA for the Detection of Faulty Elements

Input. The inputs are measurement matrix E, measurement vector p, population size P, and faulty element S.

Output. Find the vector x.

(1) Population Generation. Generate random P chromosomes:

$$\begin{gathered} G = \left[g_1, g_2, \ldots, g_P\right], \\ \operatorname{card}\left(g_i\right) \le S \\ \forall i \le 1 \le P. \end{gathered} \tag{13}$$

(2) Calculating Fitness of Parents and Sorting. Calculate the fitness of each chromosome based on (9) and sort them in the descending order:

$$\begin{aligned} f_p &= \operatorname{fit}\left(g_1, g_2, \ldots, g_P\right) \\ &= \left[f_{p1}, f_{p2}, \ldots, f_{pP}\right] \\ f_{pi} &= \left(Eg_i - p\right)^{\tau}\left(Eg_i - p\right) \\ \left[f_{ps}\ \text{index}\right] &= \operatorname{sort}\left(f_p, \text{descend}\right) \\ f_{ps} &= \left[f_1, f_2, \ldots, f_P\right] \\ &\qquad \text{with } f_1 < f_2, \ldots < f_P \\ G_s &= G\left(\text{index}\right) = \left[g_{s1}, g_{s2}, \ldots, g_{sP}\right] \\ &\qquad \text{where } g_{si} \text{ has fitness } f_i. \end{aligned} \tag{14}$$

(3) Crossover. Offspring of size half of the population are generated in random manner:

$$\begin{aligned} C &= \operatorname{crossover}\left(G_s\right) = \left[c_1, c_2, \ldots, c_{P/2}\right] \\ c_j &= \left\lfloor g_{sj} + \gamma\left(g_{sj} - g_{\text{srnd}i}\right)\right\rfloor_s \quad 1 \le j \le \frac{P}{2},\ 1 \le i \le P. \end{aligned} \tag{15}$$

(4) Calculating Fitness of Children and Sorting. It is the same as Step 2 but executed for offspring:

$$\begin{aligned} f_c &= \operatorname{fit}\left(c_1, c_2, \ldots, c_{P/2}\right) \\ \left[f_{cs}\ \text{index}\right] &= \operatorname{sort}\left(f_c, \text{descend}\right) \\ C_s &= c\left(\text{index}\right) = \left[c_{s1}, c_{s2}, \ldots, c_{sp/2}\right]. \end{aligned} \tag{16}$$

(5) PCD Algorithm. If f_1 remains the same during the specified consecutive iterations then execute:

$$e_s = \left(g_{\text{srnd}} + w_{\text{rand}} \otimes \left(E^{\tau}\left(p - Eg_{s1}\right)\right)\right). \tag{17}$$

(6) Generating New Population. Generate new population using half of the best parents and all children:

$$G_1 = \left[g_{s1}, g_{s2}, \ldots, g_{sp/2} c_{s1}, c_{s2}, \ldots, c_{sp/2}\right]. \tag{18}$$

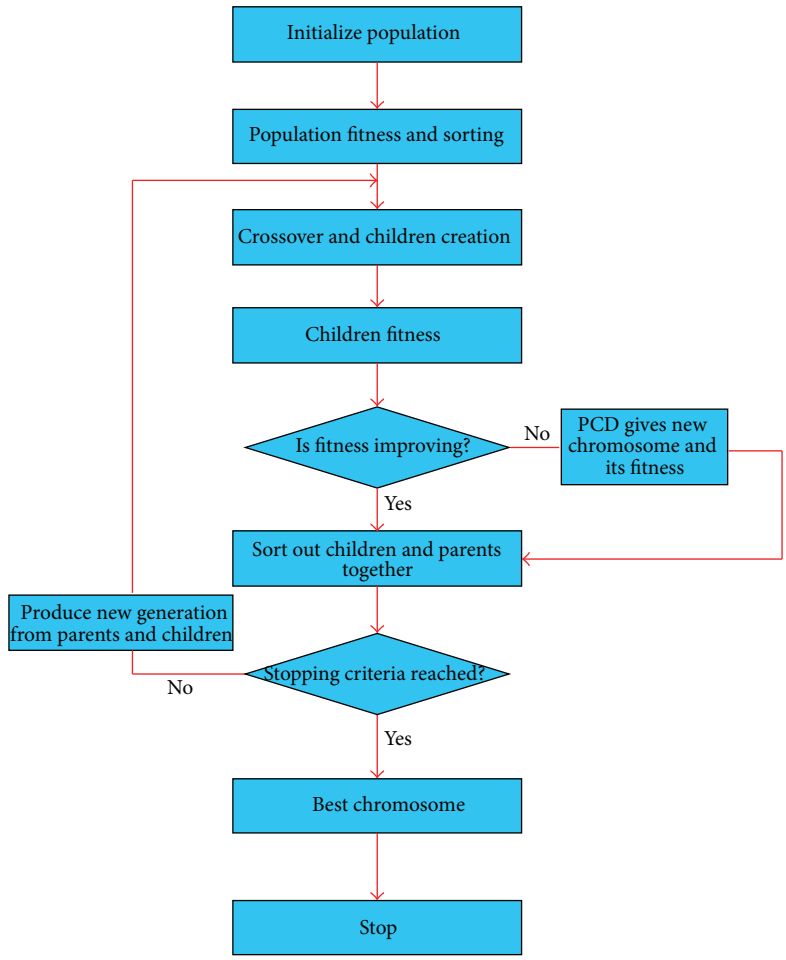

Figure 3: The flow chart of hybrid GA with PCD algorithm.

(7) Output. The chromosome with best fitness is the candidate solution $x = g_{s1}$.

The symbol card(Z) is used to indicate the cardinality of the vector Z whereas index represents a vector containing the indices when sorted in the descending arrangement. The data $\otimes$ represents the element-by-element product. The program can be stopped after either achieving the desired fitness function calculated in Step 2 or reaching maximum number of cycles.

4. Simulation Results and Discussion

In this section, first we consider a Chebyshev array of 20 elements with $\lambda/2$ interelement spacing that is used as the reference antenna. The power pattern in this case represents a −35 dB peak side lobe level with the nulls at the particular angles. The normalized MSE that is determined in detecting the faulty elements at the jth iterations is given by the following equation:

$$\text{MSE} = \frac{\left\|\widehat{x}_j - x_0\right\|_2^2}{\left\|x_0\right\|_2^2} \quad j = 1, 2, \ldots, 350, \tag{19}$$

where $j = 1, 2, \ldots, 350$ is the number of iterations and the signal to noise ratio (SNR) is given by

$$\text{SNR} = \frac{\left[\sum_{i=1}^{K} \left|A\left(\theta_i\right)\right|^2\right]}{\left[\sum_{i=1}^{K} \left|r\left(\theta_i\right)\right|^2\right]}. \tag{20}$$

To examine the simulation results the radiation pattern is sampled and 37 samples were taken from the pattern. To check the validity of the proposed method we use Matlab as a programming tool. At the first instant, we consider that the 3rd and 7th elements in the array become damaged as shown in Figure 4. Now we use the PCD algorithm to detect the location of faulty elements. After simulation with the PCD algorithm, the number and the location of faulty elements are recovered; this is shown in Figure 4. The blue square represents the original weights of the Chebyshev array, green circle represents faulty elements, and red cross represents the diagnosed fault.

The same scenario is repeated to detect the number and location of faulty elements by using GA. After using GA, the fault diagnosed is shown in Figure 5. Now we check the same fault with the hybrid GA which is depicted in Figure 6.

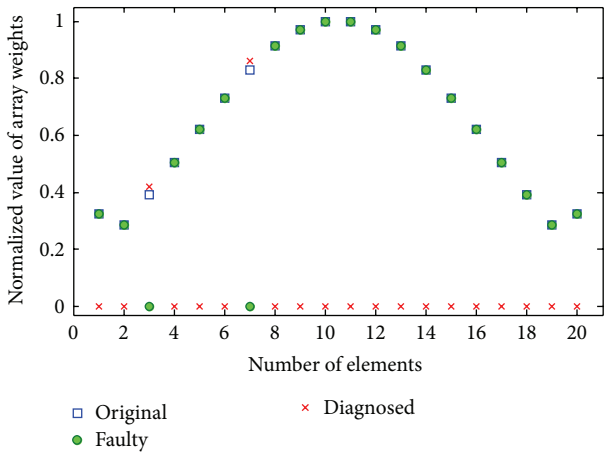

Figure 4: Detection of faulty sensors through PCD.

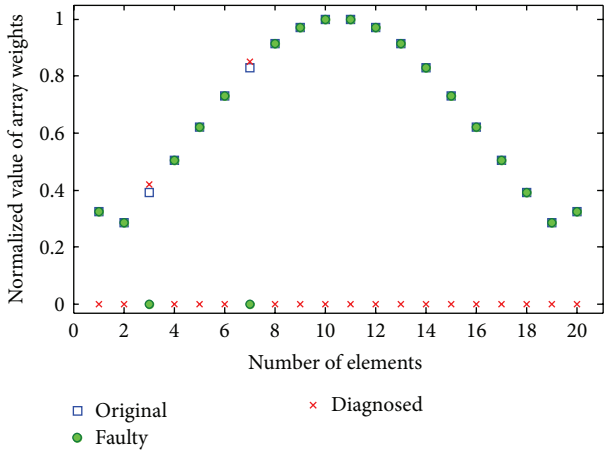

Figure 5: Detection of faulty sensors through GA.

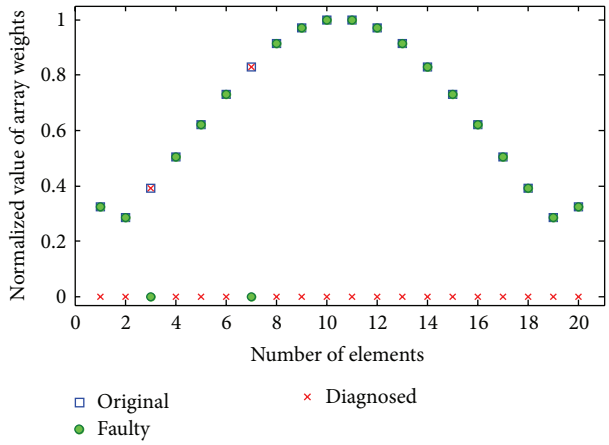

Figure 6: Detection of faulty sensors through proposed hybrid GA algorithm.

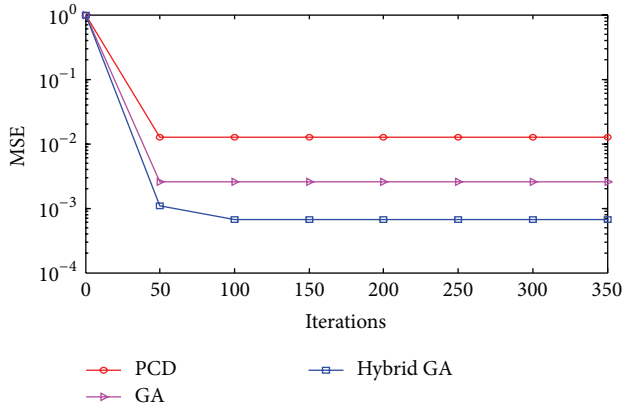

Figure 7: Comparison of PCD, GA, and hybrid GA with PCD based on MSE.

Now we detect the 3rd and 7th element failure by applying hybrid GA algorithm. The fault diagnosed through hybrid GA is depicted in Figure 6. By using the hybrid GA, we diagnosed the number and location of faulty elements more accurately than PCD and GA alone.

The performance of the proposed hybrid GA was compared with PCD and GA alone based on the normalized MSE which is computed at each run of 350 iterations by using (19). Figure 7 is the comparison of the MSE of the PCD, GA, and hybrid GA. From Figure 7 it is clear that the MSE of the hybrid GA detect the number and location of faulty elements more accurately as compared to PCD and GA alone.

Figure 8 shows the performance of the diagnosis error for different values of SNR for PCD, GA, and hybrid GA. From Figure 8, it is clear that, for lower value of SNR, we have a greater value of MSE. For the value of SNR ≥45, the value of MSE is lower and stable. Hence the hybrid GA performs better than PCD and GA alone for different value of SNR.

Now we test the proposed hybrid technique for different number of array sensors. In this case we consider an array of 30, 40, and 50 sensors. We assumed that 4 sensors are damaged. The fault is assumed at 5th, 10th, 15th, and 25th locations in an array of 30 and 40 sensors. Now we applied the proposed hybrid technique to detect the faulty sensors. The hybrid GA with PCD algorithm detect the positions of faulty sensors more accurately and the MSE graph is shown in Figure 9. Now the hybrid GA with PCD algorithm is tested for an array of 40 sensors. Again the position of fault is assumed at 5th, 10th, 15th, and 25th locations; after applying the proposed hybrid GA with PCD algorithm the fault is diagnosed. From the simulation results of Figure 9 it is clear that as the array size increases while keeping the number of faulty sensors fix, we achieved minimum MSE. The same scenario of faulty sensors is repeated for an array of 50 sensors; again the hybrid GA with PCD algorithm detects the faulty sensors positions more accurately as shown in Figure 10. From Figure 9, it is clear that the MSE curve of an array of 50 sensors is lower than the array of 30 and 40 sensors. It is clear, from simulation results, that as we increase the array size while keeping the number of faulty sensors fixed, we received accurate detection and better MSE curve. The advantages of the proposed method have been fully examined. The disadvantage is when the array size increases, the method deteriorates.

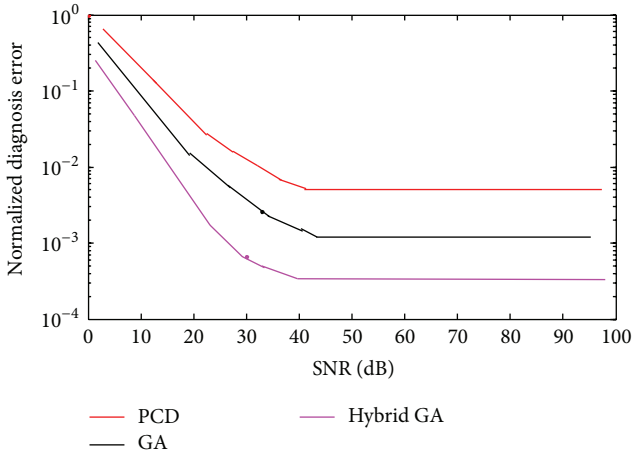

Figure 8: Diagnosis of faulty elements for different values of SNR.

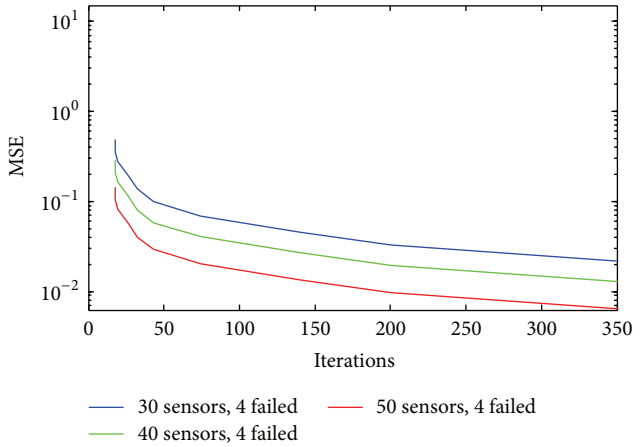

Figure 9: Comparison of hybrid GA with PCD based on MSE for different array.

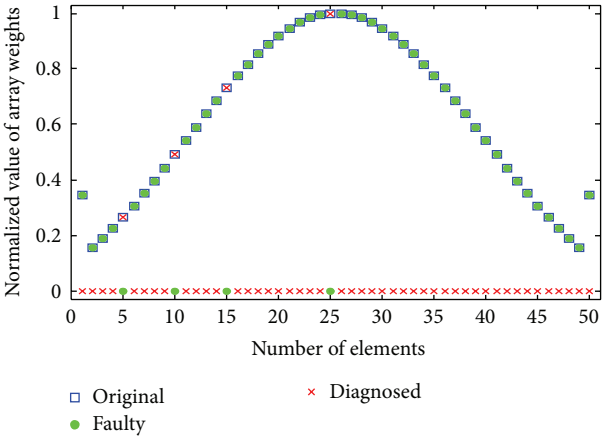

Figure 10: Detection of faulty sensors through hybrid GA with PCD algorithm.

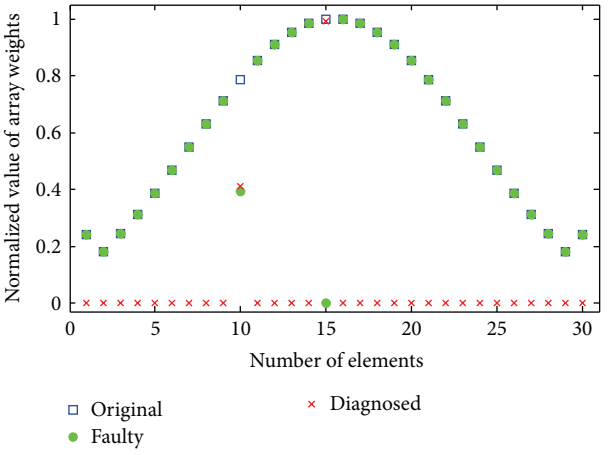

Figure 11: Detection of partial and complete fault through proposed algorithm.

4.1. Diagnosis of Partial Faults. If some elements in the array become faulty but radiate some power that is, its weight excitation is a fraction of the original but not equal to zero. The mathematical formula for partial fault is given by the following expression:

$$a_n = \begin{cases} \kappa w_n & \text{with propability } \phi \\ w_n & \text{otherwise,} \end{cases} \quad (21)$$

where $\kappa < 1$ is the partial failure factor. In this case, we consider the complete as well as partial fault. We assume that the 10th element is partially faulty (50% faulty) and the 15th element is completely faulty. The proposed technique detects the partial and complete fault more accurately which is depicted in Figure 11.

5. Conclusion and Future Work

In this paper, a compressed sensing based array diagnosis technique has been presented. This technique starts from collecting the measurement of the far-field pattern. The system linking the difference between the field measured using the healthy reference array and the field radiated by the array under test is solved using a GA, PCD algorithm, and GA hybridized with PCD algorithm. These algorithms are tested for the detection of fully and partially defective antenna elements and their simulation results validate that the proposed algorithm gives better results in terms of failure detection with a small number of measurements. The slow and early convergence of GA is prohibited by hybridizing with PCD algorithm. The hybrid GA-PCD algorithm makes the diagnosis of defective sensors (fully or partially) more accurate as compared to GA and PCD alone. Different simulation results are provided for Chebyshev array to validate the performance of the designed algorithms.

Conflict of Interests

The authors declare that there is no conflict of interests regarding the publication of this paper.

References

[1] R. J. Mailloux, *Phased Array Antenna Handbook*, Artech House, Norwood, Mass, USA, 2nd edition, 2005.

[2] G. Oliveri, M. Donelli, and A. Massa, "Linear array thinning exploiting almost difference sets," *IEEE Transactions on Antennas and Propagation*, vol. 57, no. 12, pp. 3800–3812, 2009.

[3] G. Oliveri, L. Manica, and A. Massa, "ADS-based guidelines for thinned planar arrays," *IEEE Transactions on Antennas and Propagation*, vol. 58, no. 6, pp. 1935–1948, 2010.

[4] M. Carlin, G. Oliveri, and A. Massa, "On the robustness to element failures of linear ADS-thinned arrays," *IEEE Transactions on Antennas and Propagation*, vol. 59, no. 12, pp. 4849–4853, 2011.

[5] S. U. Khan, I. M. Qureshi, F. Zaman, and A. Naveed, "Null placement and sidelobe suppression in failed array using symmetrical element failure technique and hybrid heuristic computation," *Progress In Electromagnetics Research B*, no. 52, pp. 165–184, 2013.

[6] S. U. Khan, I. M. Qureshi, F. Zaman, B. Shoaib, A. Naveed, and A. Basit, "Correction of faulty sensors in phased array radars using symmetrical sensor failure technique and cultural algorithm with differential evolution," *The Scientific World Journal*, vol. 2014, Article ID 852539, 10 pages, 2014.

[7] A. Patnaik, B. Choudhury, P. Pradhan, R. K. Mishra, and C. Christodoulou, "An ANN application for fault finding in antenna arrays," *IEEE Transactions on Antennas and Propagation*, vol. 55, no. 3, pp. 775–777, 2007.

[8] S. U. Khan, I. M. Qureshi, F. Zaman, A. Basit, and W. Khan, "Application of firefly algorithm to fault finding in linear arrays antenna," *World Applied Sciences Journal*, vol. 26, no. 2, pp. 232–238, 2013.

[9] O. M. Bucci, M. D. Migliore, G. Panariello, and P. Sgambato, "Accurate diagnosis of conformal arrays from near-field data using the matrix method," *IEEE Transactions on Antennas and Propagation*, vol. 53, no. 3, pp. 1114–1120, 2005.

[10] J. J. Lee, E. M. Ferren, D. P. Woollen, and K. M. Lee, "Near-field probe used as a diagnostic tool to locate defective elements in an array antenna," *IEEE Transactions on Antennas and Propagation*, vol. 36, no. 6, pp. 884–889, 1988.

[11] J. A. Rodríguez-González, F. Ares-Pena, M. Fernández-Delgado, R. Iglesias, and S. Barro, "Rapid method for finding faulty elements in antenna arrays using far field pattern samples," *IEEE Transactions on Antennas and Propagation*, vol. 57, no. 6, pp. 1679–1683, 2009.

[12] M. D. Migliore, "A compressed sensing approach for array diagnosis from a small set of near-field measurements," *IEEE Transactions on Antennas and Propagation*, vol. 59, no. 6, pp. 2127–2133, 2011.

[13] E. J. Candes and T. Tao, "Near-optimal signal recovery from random projections: universal encoding strategies?" *IEEE Transactions on Information Theory*, vol. 52, no. 12, pp. 5406–5425, 2006.

[14] M. Akçakaya and V. Tarokh, "Shannon-theoretic limits on noisy compressive sampling," *IEEE Transactions on Information Theory*, vol. 56, no. 1, pp. 492–504, 2010.

[15] G. Oliveri, P. Rocca, and A. Massa, "Reliable diagnosis of large linear arrays—a Bayesian compressive sensing approach," *IEEE Transactions on Antennas and Propagation*, vol. 60, no. 10, pp. 4627–4636, 2012.

[16] E. J. Candes, J. K. Romberg, and T. Tao, "Stable signal recovery from incomplete and inaccurate measurements," *Communications on Pure and Applied Mathematics*, vol. 59, no. 8, pp. 1207–1223, 2006.

[17] E. J. Candès and M. B. Wakin, "An introduction to compressive sampling," *IEEE Signal Processing Magazine*, vol. 25, no. 2, pp. 21–30, 2008.

[18] M. Lustig, D. L. Donoho, J. M. Santos, and J. M. Pauly, "Compressed sensing MRI: a look at how CS can improve on current imaging techniques," *IEEE Signal Processing Magazine*, vol. 25, no. 2, pp. 72–82, 2008.

[19] S. Ji, Y. Xue, and L. Carin, "Bayesian compressive sensing," *IEEE Transactions on Signal Processing*, vol. 56, no. 6, pp. 2346–2356, 2008.

[20] M. Elad, *Sparse and Redundant Representations: From Theory to Applications in Signal and Image Processing*, Springer, 2010.

[21] S. Mendelson, A. Pajor, and N. Tomczak-Jaegermann, "Uniform uncertainty principle for Bernoulli and subgaussian ensembles," *Constructive Approximation*, vol. 28, no. 3, pp. 277–289, 2008.

[22] R. G. Baraniuk, "Compressive sensing," *IEEE Signal Processing Magazine*, vol. 24, no. 4, pp. 118–124, 2007.

[23] L. Haupt Randy and S. Ellen Haupt, *Practical Genetic Algorithms*, John Wiley & Sons, 2004.

[24] F. Zaman, I. M. Qureshi, A. Naveed, J. A. Khan, and R. M. A. Zahoor, "Amplitude and directional of arrival estimation: comparison between different techniques," *Progress in Electromagnetics Research B*, vol. 39, pp. 319–335, 2012.

[25] F. Zaman, I. M. Qureshi, A. Naveed, and Z. U. Khan, "Joint estimation of amplitude, direction of arrival and range of near field sources using memetic computing," *Progress in Electromagnetics Research C*, vol. 31, pp. 199–213, 2012.

Hindawi Publishing Corporation
Journal of Sensors
Volume 2016, Article ID 6971952, 14 pages
http://dx.doi.org/10.1155/2016/6971952

Research Article

Gearbox Fault Diagnosis in a Wind Turbine Using Single Sensor Based Blind Source Separation

Yuning Qian and Ruqiang Yan

School of Instrument Science and Engineering, Southeast University, Nanjing, Jiangsu 210096, China

Correspondence should be addressed to Ruqiang Yan; ruqiang@seu.edu.cn

Received 28 January 2015; Accepted 19 March 2015

Academic Editor: Mehmet Karakose

This paper presents a single sensor based blind source separation approach, namely, the wavelet-assisted stationary subspace analysis (WSSA), for gearbox fault diagnosis in a wind turbine. Continuous wavelet transform (CWT) is used as a preprocessing tool to decompose a single sensor measurement data into a set of wavelet coefficients to meet the multidimensional requirement of the stationary subspace analysis (SSA). The SSA is a blind source separation technique that can separate the multidimensional signals into stationary and nonstationary source components without the need for independency and prior information of the source signals. After that, the separated nonstationary source component with the maximum kurtosis value is analyzed by the enveloping spectral analysis to identify potential fault-related characteristic frequencies. Case studies performed on a wind turbine gearbox test system verify the effectiveness of the WSSA approach and indicate that it outperforms independent component analysis (ICA) and empirical mode decomposition (EMD), as well as the spectral-kurtosis-based enveloping, for wind turbine gearbox fault diagnosis.

1. Introduction

Wind energy is one of the renewable energy sources, which have received considerable attention around the world. As critical equipment for wind energy development, the wind turbine is being widely used due to its technological maturity and good infrastructure construction [1, 2]. However, with the high demand for energy efficiency, the size of the wind turbine is increasing over the years, leading to high operation costs and risk of failures. To avoid expensive maintenance costs and economic losses caused by wind turbine failures, researches on condition monitoring and fault diagnosis of the wind turbine have been carried out. For example, Kotzalas and Doll [3] investigated the failure principle of various wind turbines. Ciang et al. [1], García Márquez et al. [4], and Liu et al. [5] reviewed the existing condition-monitoring strategies and relative fault diagnosis methods for wind turbines. Chen et al. [6] summarized main failure modes of the wind turbines and corresponding signal characteristics. It is known that the wind turbine failures often occur in the generator, blade, gearbox, and electrical system. As a key component for wind turbines, the gearbox is vulnerable to damage and the gearbox failure has a severe influence on working status of the whole system. As a result, effective diagnosis of gearbox failures has become a focused research trend. Generally, the gear mesh signal is strong while the gearbox fault-related signal is often weak and transient, causing difficulty to separate such fault-related signatures from gear mesh signals.

Over the past, some filtering methods [7, 8], for example, spectral-kurtosis-based and autoregressive model-based methods, were used to extract the fault-related signal components, but the filtering results are highly related to the filter parameter selection and may be sensitive to noise. Li et al. [9] developed a noise-controlled technique based on stochastic resonance method to enhance the fault signal by adjusting the input signal and the noise level. Combet and Gelman [10] and Heyns et al. [11] both utilized the time synchronous averaging technique to remove the gear meshing frequency with the help of an independent encoder signal to resample the measured vibration signals. Different from the above methods, independent component analysis (ICA) is a blind source separation approach, which can separate the raw

signal into several independent sources without any prior information or reference signal. For example, both He et al. [12] and Wang et al. [13] used the ICA to extract the fault-related features from gearbox vibration signals. However, the ICA approach needs to assume that each component to be separated is independent and does not take distribution changes of the signals into account. Compared with ICA, the recently developed stationary subspace analysis (SSA) [14] is also a blind source separation approach. The SSA can not only take the signal distribution into consideration [15], but also decompose a multidimensional time series into stationary and nonstationary source components without the independency assumption of these source signals. Since the gearbox fault-related signal often exhibits nonstationary behavior due to complex working condition of the wind turbines, it can be naturally characterized by the nonstationary components resulting from the SSA. Therefore, the SSA presents a good alternative for gearbox fault diagnosis. The applications of the SSA have been seen in change-point detection of the multidimensional time series [16], EEG signal processing [15, 17], geophysical data analysis [18], and image processing [19]. It should be noted that there is a multidimensional requirement when implementing the SSA algorithm. For real-time gearbox fault diagnosis of the wind turbine, although there are several sensors attached on the system, we often have only one sensor near the fault component to collect a single-dimensional signal that is highly related to the fault feature. To address such a problem, this paper presents a single sensor based blind source separation approach for gearbox fault diagnosis by integrating continuous wavelet transform with stationary subspace analysis, which is called the wavelet-assisted stationary subspace analysis (WSSA). The proposed approach first uses CWT to decompose a one-dimensional signal into multiscale wavelet coefficients, which can be considered as a multidimensional signal. Then, the SSA is applied to separating it into a set of stationary and nonstationary source components. It should be emphasized that the key of the proposed approach is to utilize the inherent multiscale analysis capability and the redundancy resulting from the CWT decomposition for dimension extension of a single sensor signal [20] and then select the SSA as a blind source separation approach for both the stationary and nonstationary signal components separation. Besides, this paper also proposes to use modified principal component analysis and runs test methods to select the number of wavelet scales and the number of nonstationary source components, respectively, for further improving the effectiveness of the WSSA approach.

The organization of the rest of the paper is as follows. Section 2 provides the theoretical background of the CWT and the SSA. The parameter selection methods for the SSA and the framework of the WSSA-based gearbox fault diagnosis approach are introduced in Section 3. Section 4 gives the experimental results, together with some discussions. Conclusions are finally stated in Section 5.

2. Wavelet-Assisted Stationary Subspace Analysis

2.1. Continuous Wavelet Transform. The CWT of a signal $x(t)$ is defined as the inner product of the signal and a selected wavelet function, which is expressed as

$$Wf_x(a,b) = \langle \psi_{a,b}(t), x(t) \rangle = |a|^{-1/2} \int x(t)\, \psi^*_{a,b}(t)\, dt, \quad (1)$$

where $\psi_{a,b}(t) = |a|^{-1/2}\psi((t-b)/a)$ is the scaled and translated wavelet function, a is the scale factor, and b denotes the time location. From this equation, the CWT at a certain scale a can be considered as a continuous correlation operation between the original signal and the wavelet function by changing the time location b. The result of the CWT is a series of wavelet coefficients with the same length as the original signal, which can express the similarity between the signal and the wavelet function at a given scale. It should be noted that the selection of the wavelet function significantly affects the performance of the CWT. Previous study for wavelet function selection using a quantitative measure (i.e., energy-to-Shannon entropy ratio) [22] has shown that the Morlet wavelet is effective for mechanical fault feature extraction and it has also been successfully applied in many cases [23–25]. Hence, the Morlet wavelet is chosen as the wavelet function in this study.

2.2. Stationary Subspace Analysis (SSA). The SSA [14] is a blind source separation technique that can separate the stationary source components from the nonstationary source components in a multidimensional signal. Neither independency nor prior information is required for these source components. In the SSA algorithm, the observed signal $\mathbf{x}(t)$ with D-dimension is assumed to be generated by a linear mixture of d stationary sources (s-sources) $\mathbf{s}_s(t) = [s_1(t), \ldots, s_d(t)]^T$ and d_n ($d_n = D - d$) nonstationary (n-sources) sources $\mathbf{s}_n(t) = [s_{d+1}(t), \ldots, s_D(t)]^T$, and $\mathbf{x}(t)$ can be expressed as

$$\mathbf{x}(t) = \mathbf{A}\mathbf{s}(t) = \begin{bmatrix}\mathbf{A}_s & \mathbf{A}_n\end{bmatrix} \begin{bmatrix}\mathbf{s}_s(t) \\ \mathbf{s}_n(t)\end{bmatrix}, \quad (2)$$

where $\mathbf{A}$ is an unknown invertible mixing matrix. The spaces spanned by the columns of $\mathbf{A}_s$ and $\mathbf{A}_n$ are called s-space and n-space, respectively. Particularly, different from the ICA algorithm, there is no independency assumption on the sources $\mathbf{s}_s(t)$ and $\mathbf{s}_n(t)$. The aim of the SSA algorithm is to find a linear transformation

$$\widehat{\mathbf{A}}^{-1} = \begin{bmatrix}\widehat{\mathbf{P}}_s \\ \widehat{\mathbf{P}}_n\end{bmatrix} \quad (3)$$

that can separate the stationary sources $\mathbf{s}_s(t)$ from nonstationary sources $\mathbf{s}_n(t)$. This can be expressed as

$$\begin{bmatrix}\widehat{\mathbf{s}}_s(t) \\ \widehat{\mathbf{s}}_n(t)\end{bmatrix} = \widehat{\mathbf{A}}^{-1}\mathbf{x}(t) = \begin{bmatrix}\widehat{\mathbf{P}}_s\mathbf{x}(t) \\ \widehat{\mathbf{P}}_n\mathbf{x}(t)\end{bmatrix}, \quad (4)$$

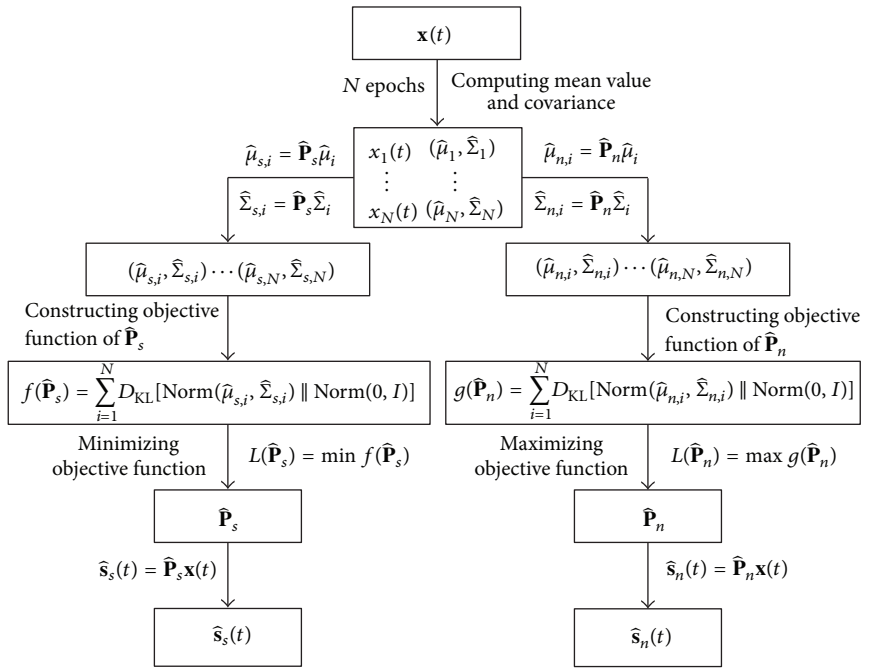

Figure 1: Flowchart of the SSA algorithm.

where $\widehat{\mathbf{s}}_s(t)$ and $\widehat{\mathbf{s}}_n(t)$ are the estimated stationary and nonstationary sources and $\widehat{\mathbf{P}}_s$ and $\widehat{\mathbf{P}}_n$ are called s-projection and n-projection. The SSA algorithm uses weak stationarity condition as an optimization criterion to recover the sources as stationary as possible [16]. The weak stationarity condition can be expressed as the mean and covariance of a time series are constant over time. Since the SSA employs an optimization criterion to recover the sources as stationary as possible, it can identify the true $\mathbf{s}_s(t)$, not the true $\mathbf{s}_n(t)$. The $\mathbf{s}_n(t)$ is often identified by maximizing the nonstationarity of the estimated nonstationary sources. The flowchart of the SSA is shown in Figure 1 and the specific procedures are illustrated as follows.

(I) The observed signal is divided into N ($N \geq (D - d_s)/2 + 2$) equal time epochs and the mean value $\widehat{\mu}_i$ and covariance $\widehat{\Sigma}_i$ for the ith epoch are calculated. For any selected $\widehat{\mathbf{P}}_s$, the mean value $\widehat{\mu}_{s,i} = \widehat{\mathbf{P}}_s \mu_i$ and covariance matrix $\widehat{\Sigma}_{s,i} = \widehat{\mathbf{P}}_s \widehat{\Sigma}_i (\widehat{\mathbf{P}}_s)^T$ of the estimated stationary source in the ith epoch can be obtained. Then the probability distribution of the estimated stationary source in the ith epoch can be obtained using normal distribution as $\mathrm{Norm}(\widehat{\mu}_{s,i}, \widehat{\Sigma}_{s,i})$.

(II) Kullback-Leibler (KL) divergence D_{KL} [26] is utilized to measure the difference between the distribution of the estimated stationary source and the standard normal distribution in each epoch. Given that $p_{s,i}(x)$ and $q_{s,i}(x)$ are probability distribution functions of two distributions $\mathrm{Norm}(\widehat{\mu}_{s,i}, \widehat{\Sigma}_{s,i})$ and $\mathrm{Norm}(0, I)$, the KL divergence between the two distributions in the ith epoch can be defined as

$$D_{\mathrm{KL}}\left[\mathrm{Norm}\left(\widehat{\mu}_{s,i}, \widehat{\Sigma}_{s,i}\right) \parallel \mathrm{Norm}\left(0, I\right)\right] = \sum_{x=1}^{n_i} p_{s,i}(x) \log\left(\frac{p_{s,i}(x)}{q_{s,i}(x)}\right), \tag{5}$$

where I is unit matrix and n_i is the point number in the ith epoch. Then the objective function is set as the sum of the KL divergence in each epoch as shown in the following equation:

$$\begin{aligned} f\left(\widehat{\mathbf{P}}_s\right) &= \sum_{i=1}^{N} D_{\mathrm{KL}}\left[\mathrm{Norm}\left(\widehat{\mu}_{s,i}, \widehat{\Sigma}_{s,i}\right) \parallel \mathrm{Norm}\left(0, I\right)\right] \\ &= \sum_{i=1}^{N} D_{\mathrm{KL}}\left[\mathrm{Norm}\left(\widehat{\mathbf{P}}_s \widehat{\mu}_i, \widehat{\mathbf{P}}_s \widehat{\Sigma}_i \left(\widehat{\mathbf{P}}_s\right)^T\right) \parallel \mathrm{Norm}\left(0, I\right)\right] \\ &= \sum_{i=1}^{N} \sum_{x=1}^{n_i} p_{s,i}(x) \log\left(\frac{p_{s,i}(x)}{q_{s,i}(x)}\right). \end{aligned} \tag{6}$$

It should be noted that $\widehat{\mathbf{P}}_s$ is the only variable in (6). Therefore, the optimal s-projection $\widehat{\mathbf{P}}_s$ can be obtained by minimizing the objective function shown in (7). Then, the optimal estimated stationary source $\widehat{\mathbf{s}}_s(t)$ can be obtained using (4):

$$L\left(\widehat{\mathbf{P}}_s\right) = \min f\left(\widehat{\mathbf{P}}_s\right). \tag{7}$$

(III) Similar to the procedure described in (I) and (II), the objective function for nonstationary source components is formulated in (8). By maximizing the objective function [16] as shown in (9), the n-projection $\widehat{\mathbf{P}}_n$ is obtained and the estimated nonstationary source $\widehat{\mathbf{s}}_n(t)$ can be calculated by (4):

$$\begin{aligned} g\left(\widehat{\mathbf{P}}_n\right) &= \sum_{i=1}^{N} D_{\mathrm{KL}}\left[\mathrm{Norm}\left(\widehat{\mu}_{n,i}, \widehat{\Sigma}_{n,i}\right) \parallel \mathrm{Norm}\left(0, I\right)\right] \\ &= \sum_{i=1}^{N} D_{\mathrm{KL}}\left[\mathrm{Norm}\left(\widehat{\mathbf{P}}_n \widehat{\mu}_i, \widehat{\mathbf{P}}_n \widehat{\Sigma}_i \left(\widehat{\mathbf{P}}_n\right)^T\right) \parallel \mathrm{Norm}\left(0, I\right)\right] \end{aligned}$$

$$= \sum_{i=1}^{N} \sum_{x=1}^{n_i} p_{n,i}(x) \log\left(\frac{p_{n,i}(x)}{q_{n,i}(x)}\right), \tag{8}$$

$$L\left(\widehat{\mathbf{P}}_n\right) = \max g\left(\widehat{\mathbf{P}}_n\right). \tag{9}$$

From the procedures presented above, it can be seen that, as compared to the ICA, the SSA takes the distribution change of the raw signal into account and allows for dependency between the source components, which may better satisfy real-world situations. Combing the CWT with the SSA, a single sensor based blind source separation approach (i.e., WSSA) can now be developed.

2.3. Simulation Evaluation. To evaluate the performance of the WSSA for gearbox fault diagnosis, a simulation study is first conducted, where a test signal simulating the gearbox signal is formulated as follows [13]:

$$\begin{aligned} x_1(t) &= e^{-400*t_1} \sin(2\pi f_1 t), \quad t_1 = \operatorname{mod}\left(t, \frac{1}{f_B}\right), \\ x_2(t) &= \sin(2\pi f_2 t), \\ x_3(t) &= 0.8 * \sin(2\pi f_3 t), \\ x_4(t) &= \sin(2\pi f_4 t), \\ n(t) &= 0.16 * \operatorname{randn}(n, 1), \quad n = \operatorname{length}(t), \\ x(t) &= x_1(t) + x_2(t) + x_3(t) + x_4(t) + n(t). \end{aligned} \tag{10}$$

There are four source signals in the simulated signal as shown in Figure 2. $x_1(t)$ represents the outer raceway defect-related signal of a bearing modulated by the resonance signal of the system, where f_1 is the resonance frequency and f_B is the bearing defect characteristic frequency. The 3-stage gear meshing signals are simulated by $x_2(t)$, $x_3(t)$, and $x_4(t)$, respectively. In addition, $n(t)$ represents the noise. The values of these frequency components are set as f_B = 33 Hz, f_1 = 3600 Hz, f_2 = 420 Hz, f_3 = 160 Hz, and f_4 = 50 Hz, respectively. The waveform of the simulated signal and its frequency spectrum are shown in Figure 3, where the three-stage gear meshing frequencies f_2, f_3, and f_4 can be seen clearly, but the bearing defect characteristic frequency cannot be identified.

The simulated signal is then decomposed using the CWT, where the Morlet wavelet is chosen as the wavelet function. Since there are four main source components in the raw signal, the wavelet coefficients at four scales are chosen as input for the SSA decomposition and they are separated into 3 stationary sources and 1 nonstationary source as shown in Figure 4. It can be seen that the shape of the nonstationary source is similar to the wave shape of the $x_1(t)$. At last, the Hilbert transform is used to extract the envelope of the nonstationary source and spectral analysis is subsequently applied to obtaining the envelope spectrum as shown in Figure 5(b), where the bearing defect characteristic frequency f_B is clearly extracted. Although the simulated signal is not very complex when comparing with the signals in real cases, the simulation results verify the effectiveness of the WSSA for gearbox failure signal analysis.

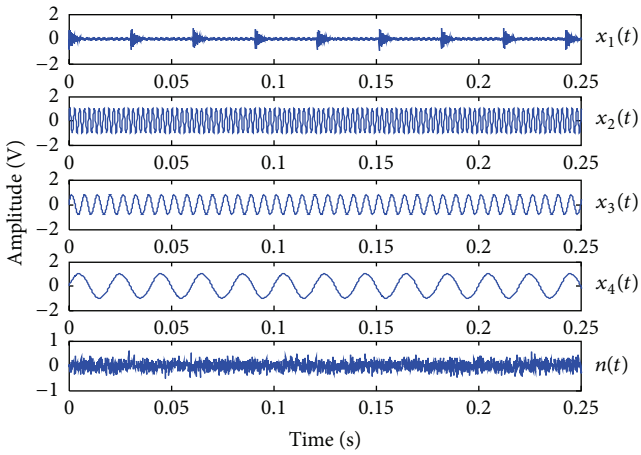

FIGURE 2: Source components of simulation signal.

It should be noted that when the WSSA is applied to real gearbox vibration signals, the number of source components contained in the vibration signals is not known *a priori*; thus it is necessary to determine how many wavelet scales (D value) should be chosen and which scales need to be selected for the WSSA. In addition, how to choose a proper number of stationary or nonstationary sources is another key issue. These two issues will be addressed in the following section.

3. Framework of Gearbox Fault Diagnosis Based on WSSA

3.1. Dimension D Selection Using mPCA. Generally speaking, the result of the CWT is a high-dimensional wavelet coefficient matrix. The considerable signal dimension severely affects the algorithm efficiency of the WSSA. Hence, dimension reduction is necessary for the high-dimensional wavelet coefficient matrix. As a popular dimension reduction method, principal component analysis (PCA) has been widely used to transform a set of possibly correlated variables into a set of linearly uncorrelated principal components which can better reflect the characteristics of the system [27]. Specifically, given a N-dimension series $\mathbf{x}(t) = [x_1(t), x_2(t), \ldots, x_N(t)]$, PCA can transform $\mathbf{x}(t)$ into a set of principal components $\mathbf{f}(t) = [f_1(t), f_2(t), \ldots, f_N(t)]$. Each $f_i(t)$ is a linear superposition of $\{x_1(t), x_2(t), \ldots, x_N(t)\}$ as

$$\begin{aligned} f_1(t) &= b_{11}x_1(t) + b_{12}x_2(t) + \cdots + b_{1N}x_N(t), \\ f_2(t) &= b_{21}x_1(t) + b_{22}x_2(t) + \cdots + b_{2N}x_N(t), \\ &\vdots \\ f_N(t) &= b_{N1}x_1(t) + b_{N2}x_2(t) + \cdots + b_{NN}x_N(t), \end{aligned} \tag{11}$$

where b_{ij} (i, j = 1 to N) represents the principal component coefficient and each principal component corresponds to

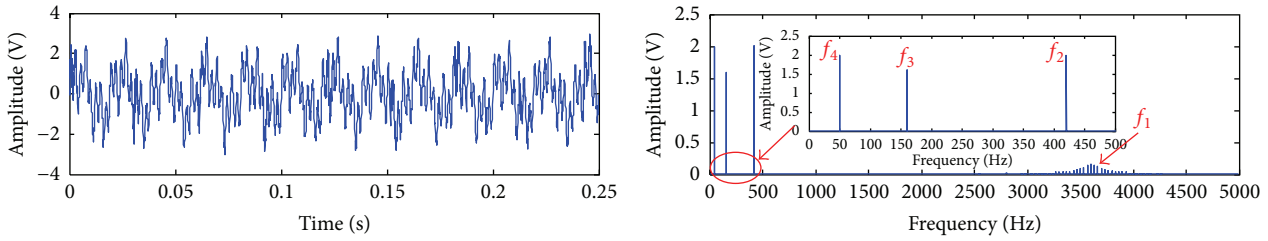

(a) (b)

Figure 3: The simulated signal and its frequency spectrum.

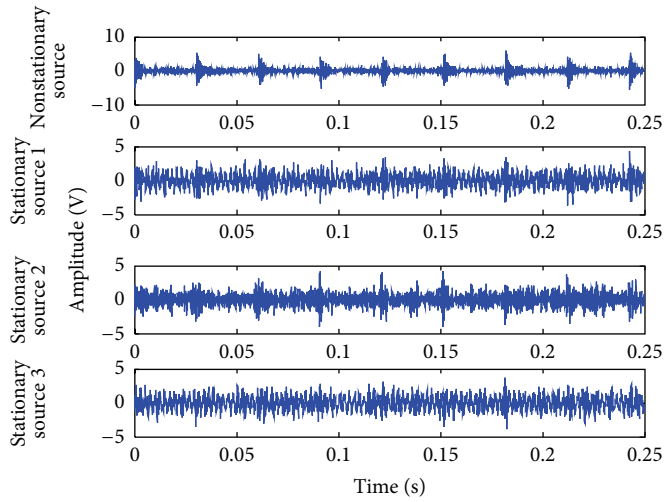

Figure 4: SSA results of simulation signal.

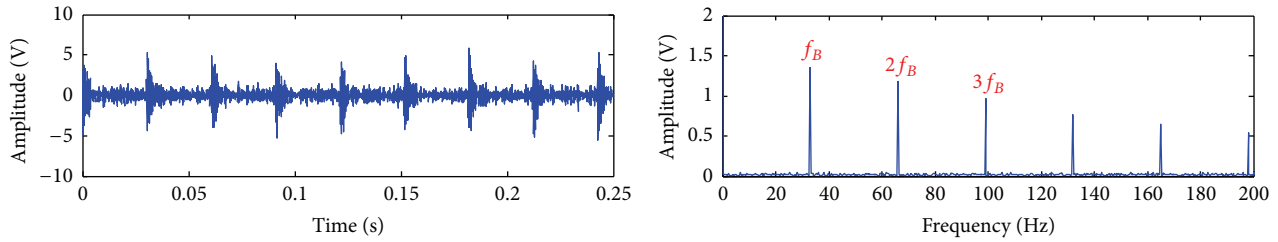

(a) (b)

Figure 5: Envelope analysis for nonstationary source with maximum kurtosis.

a variance contribution σ_i. Equation (11) can be rewritten using matrix style as

$$\mathbf{f}^T(t) = \mathbf{B}\mathbf{x}^T(t), \tag{12}$$

where

$$\mathbf{B} = \begin{bmatrix} b_{11} & b_{12} & \cdots & b_{1N} \\ b_{21} & b_{21} & \cdots & b_{2N} \\ \vdots & \vdots & \vdots & \vdots \\ b_{N1} & b_{N2} & \cdots & b_{NN} \end{bmatrix}. \tag{13}$$

Traditionally, the principal components with high cumulative variance contribution can be selected as low-dimensional features of the raw high-dimensional series. For example, if $\sum_{i=1}^{K-1}\sigma_i < \sigma_{\text{th}}$ and $\sum_{i=1}^{K}\sigma_i \geq \sigma_{\text{th}}$ (σ_{th} represents cumulative variance contribution), the K principal components $f_1(t)$ to $f_K(t)$ can be chosen as low-dimensional features. However, there will be a problem when the traditional PCA is used to choose the outstanding wavelet scales. The wavelet coefficient series in each scale represents the feature of the raw signal under a certain frequency-band window, but the chosen principal components by the PCA are a linear superposition of these wavelet coefficients in each scale, leading to multi-frequency information mixture in each principal component, which may increase separation difficulty of the SSA. On the other hand, for each principal component, the value of component coefficient b_{ij} can reflect the contribution rate of each $x_j(t)$. The larger the coefficient b_{ij} is, the more important the wavelet series $x_j(t)$ will be. Taking all chosen principal

components into account, a measure called variable score can be calculated using the following method: based on cumulative variance contribution σ_{th}, the number D ($D < N$) of outstanding principal components is obtained. Then the coefficients of the first D principal components are processed by (14) to calculate the variable score $\mathbf{F} = [F_1 \ F_2 \ \cdots \ F_D]$:

$$\mathbf{F}^T = \mathbf{B}^T \boldsymbol{\Delta}^T, \tag{14}$$

where $\boldsymbol{\Delta} = [\sigma_1 \ \sigma_2 \ \cdots \ \sigma_N]$. This equation can be further expanded as

$$\begin{aligned} F_1 &= b_{11}\sigma_1 + b_{21}\sigma_2 + \cdots + b_{N1}\sigma_N, \\ F_2 &= b_{12}\sigma_1 + b_{22}\sigma_2 + \cdots + b_{N2}\sigma_N, \\ &\vdots \\ F_D &= b_{1D}\sigma_1 + b_{2D}\sigma_2 + \cdots + b_{ND}\sigma_N, \end{aligned} \tag{15}$$

where F_i stands for the ith variable score. It should be noted that each F_i represents the contribution rate of wavelet coefficients in each scale $x_i(t)$. As a result, the D series of wavelet coefficients with larger score F, corresponding to D wavelet scales, are chosen from the N-dimensional wavelet series as a D-dimension feature for the WSSA algorithm.

3.2. Dimension d Selection Using Runs Test. Before the SSA algorithm is executed, we need to determine the number of stationary sources d from the D-dimensional features. If d is chosen, d_n can be calculated as $D - d$. In [16], this parameter selection issue is discussed and a likelihood ratio test statistic is constructed to choose d using the distribution test. In fact, the essence of this method is to identify the stationarity of the source signals obtained by the SSA. Hence, this d selection problem can be transferred to a stationarity identification problem. The D-dimensional signals can be decomposed by the SSA using different d from 1 to $D - 1$, and the dimension of the most stationary sources is the most suitable d value. Therefore, a novel d selection method, called runs test, has been utilized for the SSA in this study. The runs test method [28] is a stationarity identification method which has been used in various fields, such as wireless networks [29], financial time series analysis [30], and simulation run length determination [31]. In this study, the d selection method using runs test is designed as follows.

(a) Based on the D-dimensional wavelet coefficient series, $d = i$ ($i = 1$ to D) is chosen to implement the SSA and obtain the d stationary sources $\hat{s}^s(t)$ and $D-d$ nonstationary sources $\hat{s}^n(t)$.

(b) For each stationary source involved in a d-dimensional stationary source, the points larger than mean value will be marked as 1 and the rest will be marked as 0. The number of 1 and 0 can be marked as n_1 and n_0, respectively. The runs r can be defined as the total number of consecutive 1's and 0's in one series. For example, given two series $L_1 = [1 \ 0 \ 0 \ 1 \ 1]$ and $L_2 = [1 \ 1 \ 0 \ 0 \ 0]$, the runs $r_1 = 3$ and $r_2 = 2$, respectively. Based on the definition, the number of runs r can be calculated.

(c) The total number of runs in the signal can provide information regarding whether it is stationary or not. A signal that contains very few runs is probably stationary, while a signal that contains many runs is more likely to be nonstationary. Considering that different sizes of different signals may affect runs calculation, the runs value r cannot be compared directly. Since the runs value r can be treated as an approximate Gaussian distribution, the mean value and variance of r can be acquired as (16) [30] and a statistic Z [32], standardization of r, can be obtained to identify the stationarity of the series as (17). The larger the $|Z|$ is, the more nonstationary the series will be. As a result, the mean value Z_d of $|Z|$ for d stationary sources is obtained from (18). Consider

$$\begin{aligned} E &= \frac{2n_0n_1}{n_0 + n_1} + 1, \\ D &= \frac{2n_0n_1\left(2n_0n_1 - n_0 - n_1\right)}{\left(n_0 + n_1\right)^2\left(n_0 + n_1 - 1\right)}, \end{aligned} \tag{16}$$

$$\begin{aligned} Z &= \frac{r - E}{\sqrt{D}} \\ &= \frac{r - 2n_0n_1/\left(n_0 + n_1\right) - 1}{\sqrt{2n_0n_1\left(2n_0n_1 - n_0 - n_1\right)/\left(n_0 + n_1\right)^2\left(n_0 + n_1 - 1\right)}}, \end{aligned} \tag{17}$$

$$Z_d = \frac{1}{d}\sum_{i=1}^{d} |Z(i)|. \tag{18}$$

(d) d from 1 to $D-1$ is chosen for the SSA algorithm, and then $(D-1)$ Z_d values are obtained based on procedures (b) and (c). The d value, corresponding to the smallest Z_d, will be selected as the final number of stationary sources.

3.3. Framework of Gearbox Fault Diagnosis Approach. By integrating the proposed methods, the framework of gearbox fault diagnosis approach is presented in Figure 6. The gearbox vibration signal is firstly decomposed by the CWT to obtain the multiscale wavelet coefficients. Secondly, the modified PCA is used to select the coefficients in certain scales and obtain a low-dimensional coefficient series. Thirdly, the runs test method is utilized to decide how many stationary sources should be separated from the wavelet coefficient series. Fourthly, the SSA algorithm is applied to separating the wavelet coefficient series into stationary sources and nonstationary sources. At last, the nonstationary source with the maximum kurtosis value is selected and processed using enveloping spectral analysis. The obtained envelope spectrum is used to detect the defect frequency of the gearbox.

4. Experimental Study

In order to verify the effectiveness of the WSSA-based gearbox fault diagnosis approach, vibration signals collected from a real wind turbine gearbox are analyzed. The experimental data is contributed by a project called Gearbox Reliability Collaborative (GRC) hosted by National Renewable Energy

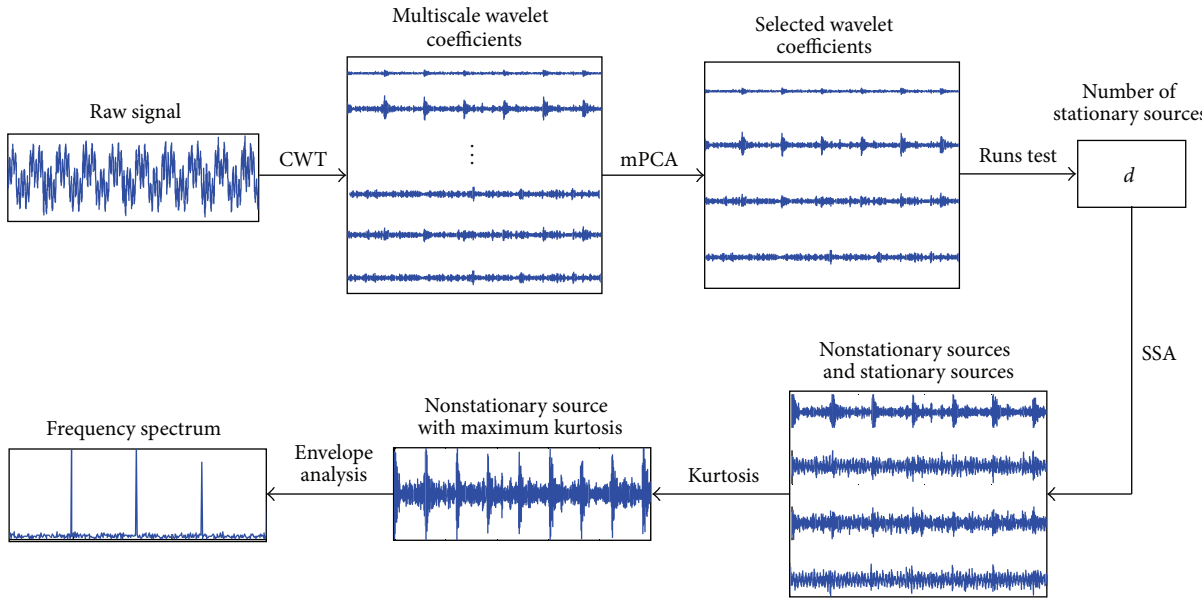

Figure 6: Flowchart of gearbox fault diagnosis approach.

Figure 7: Test wind turbine.

Laboratory (NREL) [33]. The test turbine (Figure 7) is a stall-controlled, three-bladed, upwind turbine with a rated power of 750 kW. The gearbox under test is composed of one low speed (LS) planetary stage and two parallel stages and has an overall ratio of 1 : 81.491. The structure of this gearbox is shown in Figure 8. Accelerometers are mounted on several locations outside of the gearbox to collect vibration signals with 40 kHz sampling rate.

4.1. Case Study I. The first case study analyzes a vibration signal measured by the accelerometer AN6 (model: IMI622B01), which is close to bearing D (model: SKF NU-2220-ECM, near the high speed shaft). In this study, the rotation speed of the high speed shaft (denoted as HS_shaft) is 1200 rpm and the electric power is 25%. The waveform and frequency spectrum of the vibration signal are shown in Figure 9. It can be seen that the rotation frequency of HS_shaft ($f_{HS} = 20$ Hz) is visible in Figure 9(b), while no defect-related frequency for bearing D is identified.

The WSSA algorithm is then used to process the same signal. After the CWT decomposition, wavelet coefficients of scale 1–32 are obtained and mPCA is used to find four outstanding scales, which are identified as scales 15, 18, 19, and 20. Then the runs test method is utilized to compute the statistic $Z_1 = 192.89$, $Z_2 = 265.10$, and $Z_3 = 217.06$, among which Z_1 is the smallest. This means one stationary source and three nonstationary sources can be determined through the SSA. The results for extracted stationary and nonstationary source components are shown in Figure 10, among which the nonstationary source 3 with the maximum kurtosis value is selected and processed using enveloping spectral analysis. From the envelope spectrum shown in Figure 11, the inner raceway defect frequency of the bearing D ($f_{BPFI} = 50$ Hz) can be clearly identified. In fact, the bearing D indeed suffered from the inner raceway defect as shown in Figure 12. To make a comparison, the wavelet coefficients at the scale with the maximum kurtosis are directly used for enveloping spectral analysis, and the defect frequency 50 Hz cannot be identified from the results shown in Figure 13. In addition, the ICA method is used to process the same vibration signal and conduct the same diagnostic procedure as the SSA does. As shown in Figure 14, although the defect frequency can also be identified, it is not so prominent as compared to the result obtained using the SSA. Empirical mode decomposition (EMD) technique is also used to decompose the signal and the intrinsic mode function (IMF) with maximum kurtosis is chosen for enveloping spectral analysis. From the result shown in Figure 15, the defect frequency is nearly submerged in the surrounding frequency components. Furthermore, the spectral kurtosis is applied to the vibration signals to find the proper central frequency 2500 Hz and bandwidth 312 Hz (shown in Figure 16), and then a band-pass filter with the chosen central frequency and bandwidth is used to filter the vibration signal. From the envelope spectrum of the filtered signal shown in Figure 17, the magnitude of the defect frequency 50 Hz is not large enough as compared to other adjacent frequency components. This case study verifies the effectiveness of the proposed WSSA for wind turbine gearbox fault diagnosis.

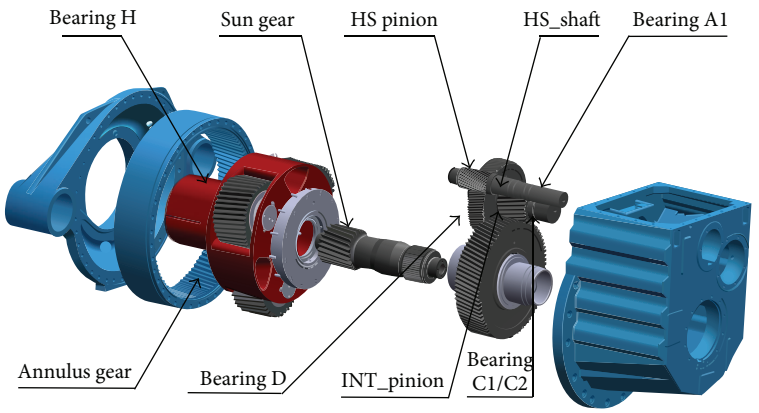

FIGURE 8: Structure of test gearbox.

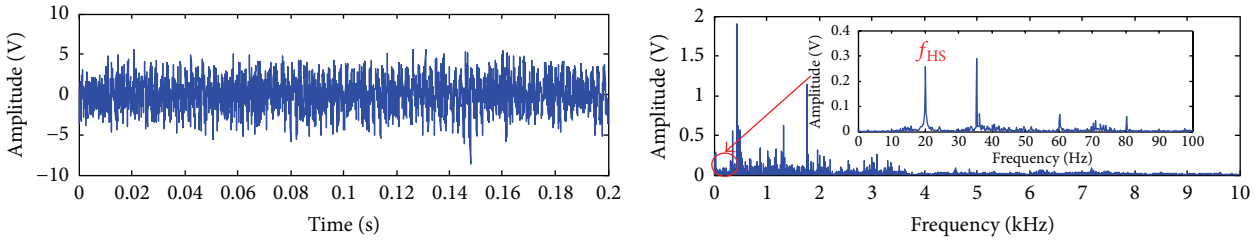

(a) (b)

FIGURE 9: Waveform and frequency spectrum of AN6 signals: (a) waveform; (b) frequency spectrum.

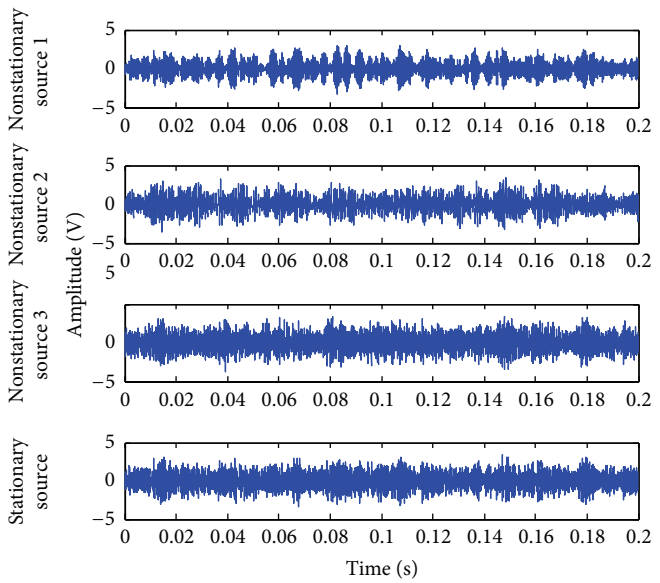

FIGURE 10: SSA results of AN6 signals.

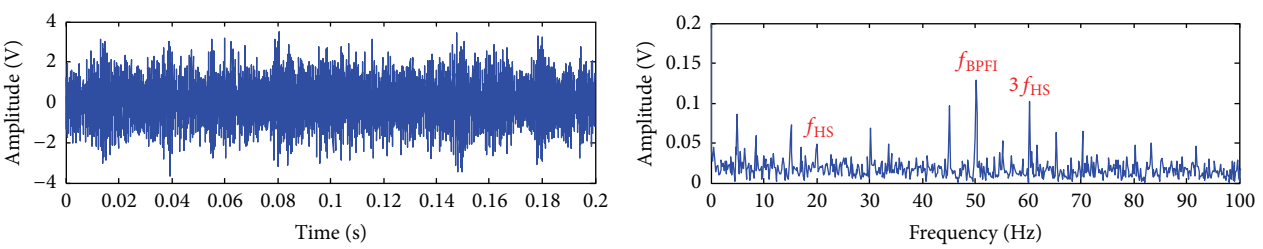

(a) (b)

FIGURE 11: Envelope analysis of nonstationary source with maximum kurtosis: (a) waveform; (b) frequency spectrum.

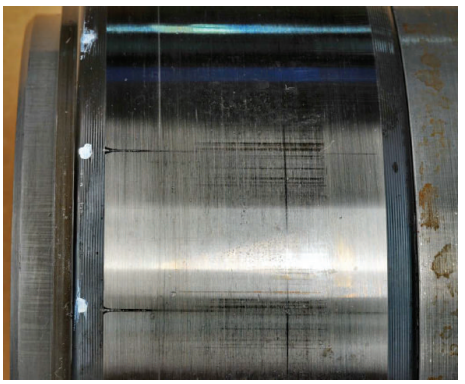

Figure 12: Inner race defect of bearing D [21].

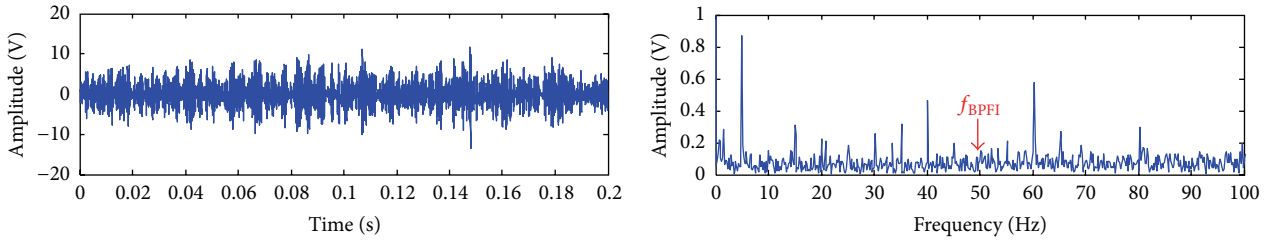

Figure 13: CWT and maximum kurtosis comparison results of AN6 signals: (a) waveform; (b) frequency spectrum.

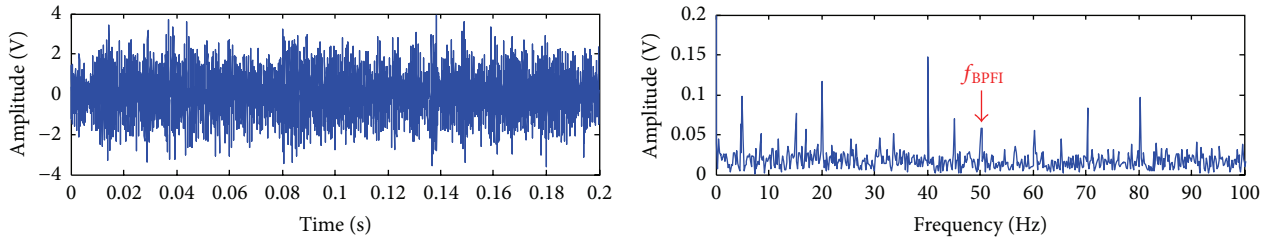

Figure 14: ICA comparison results of AN6 signals: (a) waveform; (b) frequency spectrum.

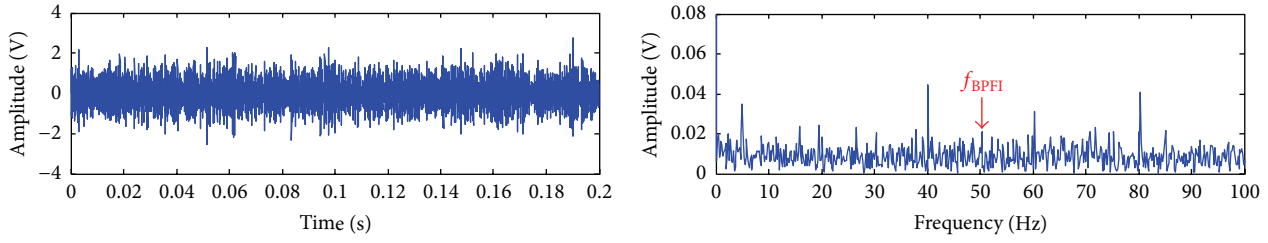

Figure 15: EMD comparison results of AN6 signals: (a) waveform; (b) frequency spectrum.

4.2. Case Study II. The second case study analyzes a vibration signal measured by the accelerometer AN3 (model: IMI 626B02), which is close to bearing H (model: FAG SL181856E). In this study, the rotation speed of the high speed shaft (HS_shaft) is 1800 rpm and the electric power is 25%. The bearing H is used to support the main shaft (rotation speed: 22.09 rpm). The waveform and frequency spectrum of the vibration signal are shown in Figure 18, where no defect-related frequency for bearing H is identified.

The vibration signal is then processed by the proposed WSSA approach. Following the same procedure as shown in case study I, wavelet coefficients of the vibration signal at

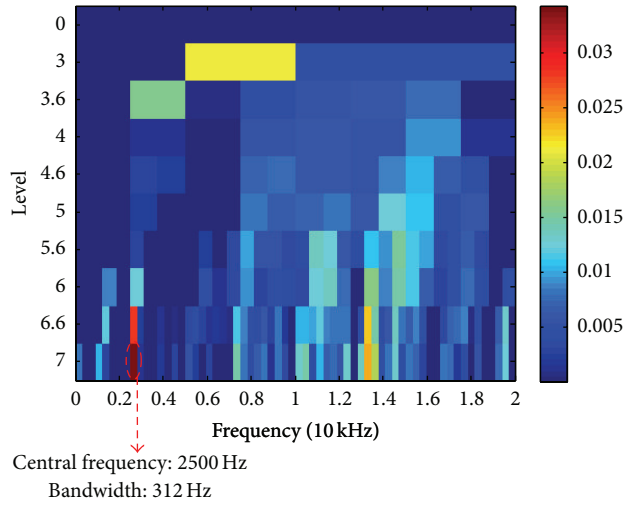

FIGURE 16: Spectral kurtosis of AN6 signals.

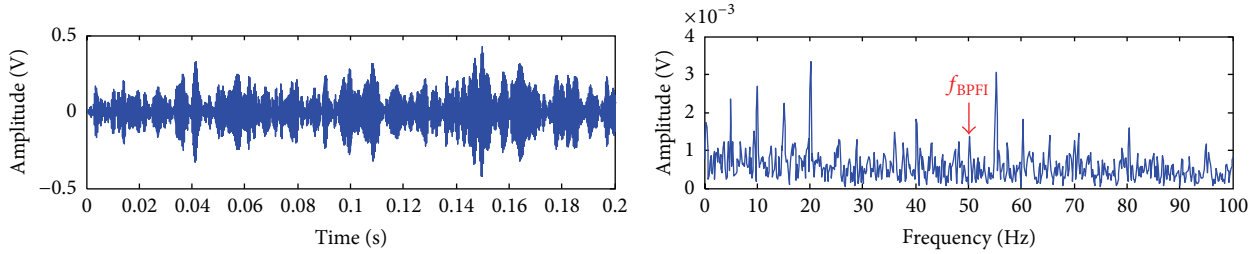

FIGURE 17: Filtered results based on spectral kurtosis of AN6 signals: (a) filtered signal; (b) frequency spectrum.

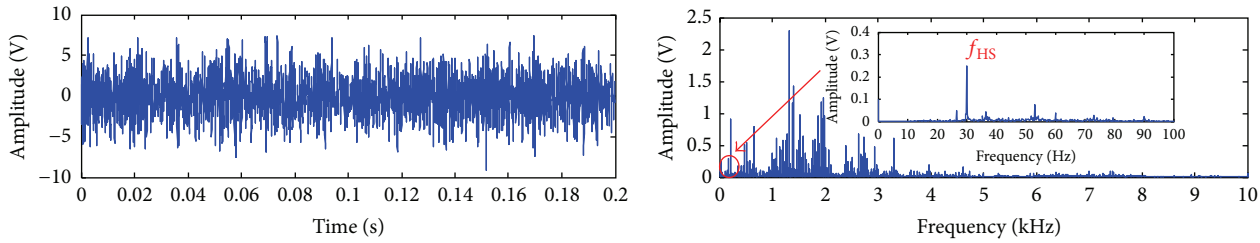

FIGURE 18: Waveform and frequency spectrum of AN3 signals: (a) waveform; (b) frequency spectrum.

scales 1–32 are obtained by the CWT. Then the coefficients at the three scales 23, 24, and 25 are selected by the mPCA, and the runs test is performed to calculate the statistic $Z_1 = 409.68$ and $Z_2 = 350.80$, among which Z_2 is smaller than Z_1. This means two stationary sources and one nonstationary source can be extracted from the vibration signal through the SSA, and the result is shown in Figure 19. The enveloping spectral analysis of the nonstationary source is then conducted and the resulting envelope spectrum is shown in Figure 20. In addition to the intermediate speed shaft (denoted as IS_shaft) rotation frequency $f_{IS} = 7.5$ Hz, the outer raceway defect frequency of the bearing H ($f_{BPFO} = 8.6$ Hz) can also be clearly identified. This is consistent with the physical examination for the bearing H as shown in Figure 21. For comparison study, the methods using the CWT with maximum kurtosis-based scale selection, ICA, EMD, and the band-pass filter based on spectral kurtosis are also used to process the same vibration signal and the results are shown in Figures 22–26, respectively. From these figures, it can be seen that the rotation frequency of the IS_shaft is highlighted, while the outer raceway defect frequency of the bearing H is almost submerged in the spectrum and cannot be identified. The comparison results further confirm the effectiveness of the WSSA for wind turbine gearbox fault diagnosis.

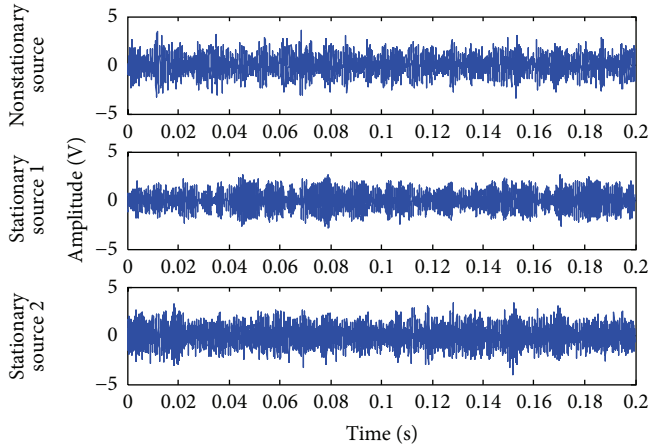

Figure 19: SSA result of AN3 signals.

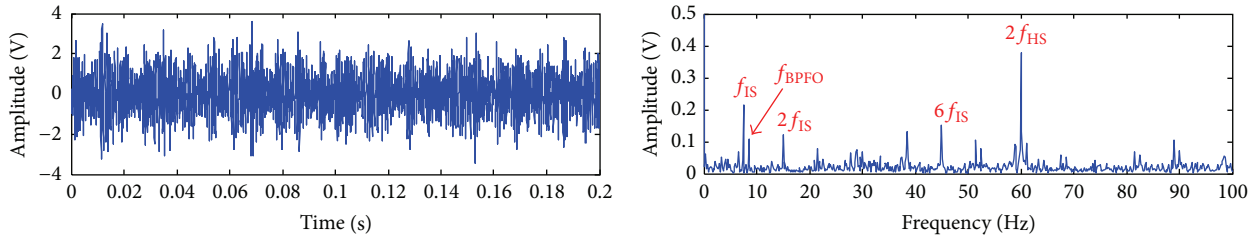

(a) (b)

Figure 20: Envelope analysis of nonstationary source with maximum kurtosis: (a) waveform; (b) frequency spectrum.

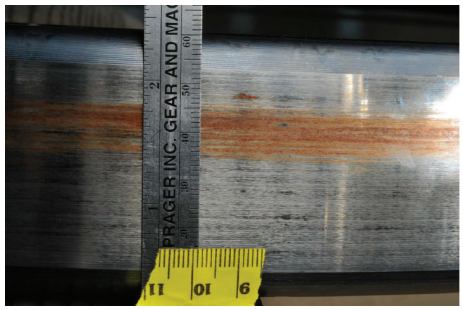

Figure 21: Outer race defect of the bearing H [21].

5. Conclusions

This paper presents a single sensor based blind source separation approach (i.e., the WSSA) for wind turbine gearbox fault diagnosis by integrating the CWT with the SSA. The modified PCA (mPCA) and runs test methods are brought in for the presented approach to quantitatively choose the suitable wavelet scales and the number of stationary sources, respectively. The proposed method can use a single sensor signal for SSA separation based on the signal distribution without any independency assumption. Furthermore, the mPCA can effectively reduce the computation load of the SSA by wavelet coefficient dimension reduction and the runs test can ensure an optimal separation mode for the SSA. In the experimental study performed on a real wind turbine gearbox, the proposed WSSA approach can well separate the stationary signal components from the nonstationary signal components mixed in the vibration signal and accurately identify the defect frequency of the bearing in the wind turbine gearbox. In addition, comparison study using CWT with maximum kurtosis, ICA, EMD, and spectral-kurtosis-based approaches indicates that the proposed WSSA approach is more beneficial than these existing methods for wind turbine gearbox diagnosis. However, the influence of the time epoch number N proposed in Section 2.2 on the SSA result is not considered in this paper which needs to be further investigated in the future study. In addition, it should be noted that the proposed diagnosis approach is tested using the signal collected from constant speed gearbox. By combining this approach with order tracking method, it is

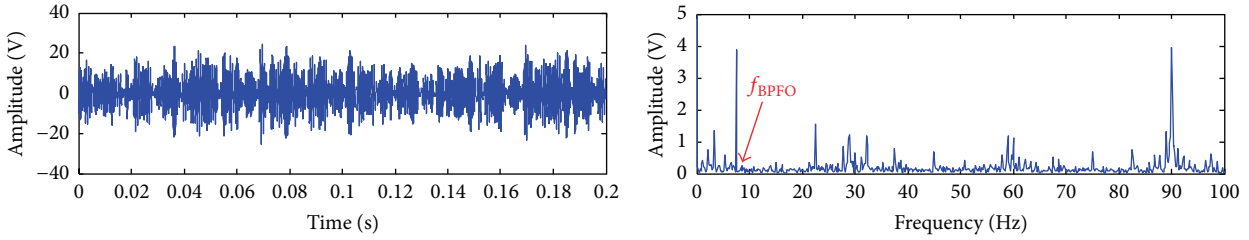

Figure 22: CWT and maximum kurtosis comparison results of AN3 signals: (a) waveform; (b) frequency spectrum.

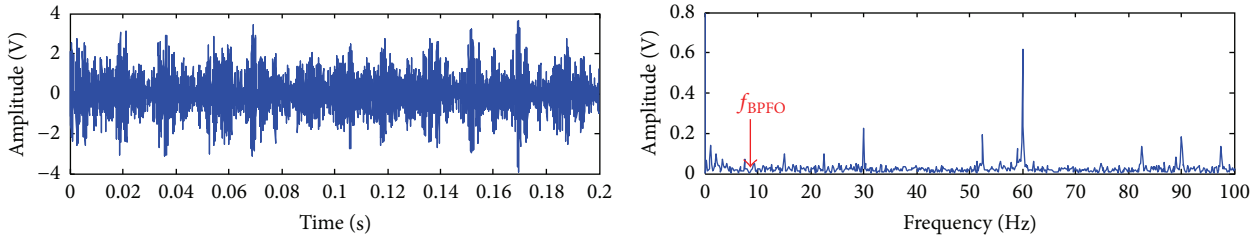

Figure 23: ICA comparison results of AN3 signals: (a) waveform; (b) frequency spectrum.

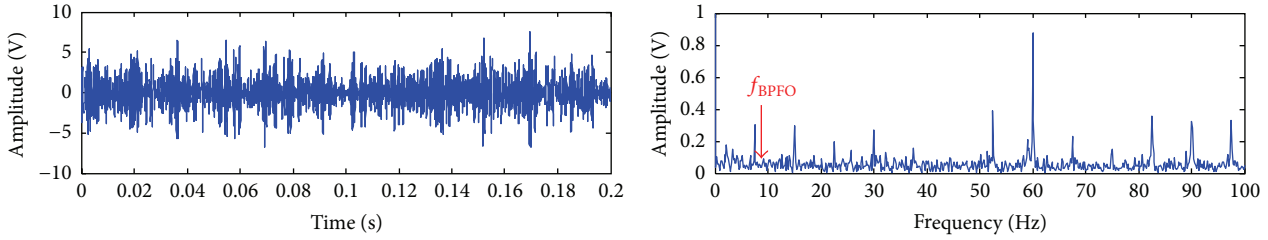

Figure 24: EMD comparison results of AN3 signals: (a) waveform; (b) frequency spectrum.

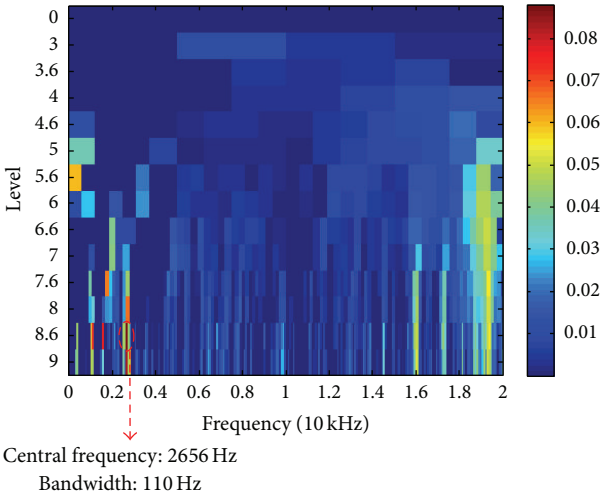

Figure 25: Spectral kurtosis of AN3 signals.

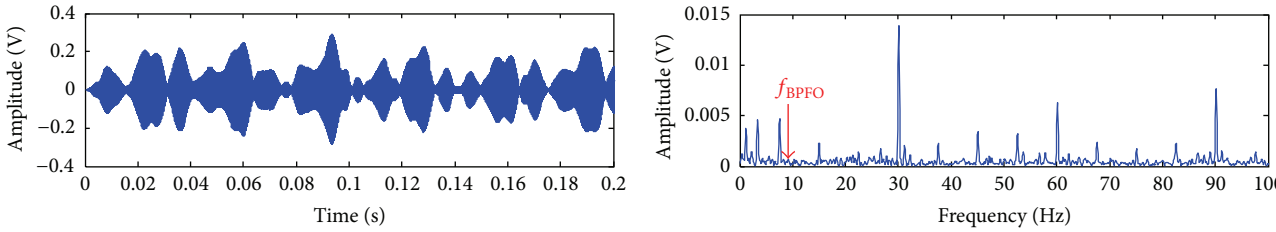

FIGURE 26: Filtered results based on spectral kurtosis of AN3 signals: (a) filtered signal; (b) frequency spectrum.

able to deal with the signals under variable-speed conditions and can also be applied to monitoring variable-speed wind turbines.

Conflict of Interests

The authors declare that there is no conflict of interests regarding the publication of this paper.

Acknowledgments

The authors would like to thank Dr. Shuangwen Sheng (from National Renewable Energy Laboratory) for supplying the experimental data of the wind turbine gearbox. This work has been supported in part by the National Natural Science Foundation of China (51175080), the State Key Laboratory for Manufacturing Systems Engineering, Xi'an Jiaotong University (sklms2012010), Scientific Research Foundation of Graduate School of Southeast University (YBJJ1424), Postgraduate Research & Innovation Project of Jiangsu Province, and the Fundamental Research Funds for the Central Universities under Grant CXZZ12-0096.

References

[1] C. C. Ciang, J.-R. Lee, and H.-J. Bang, "Structural health monitoring for a wind turbine system: a review of damage detection methods," *Measurement Science and Technology*, vol. 19, no. 12, Article ID 122001, 20 pages, 2008.

[2] A. Kusiak and W. Li, "The prediction and diagnosis of wind turbine faults," *Renewable Energy*, vol. 36, no. 1, pp. 16–23, 2011.

[3] M. N. Kotzalas and G. L. Doll, "Tribological advancements for reliable wind turbine performance," *Philosophical Transactions of the Royal Society A: Mathematical, Physical and Engineering Sciences*, vol. 368, no. 1929, pp. 4829–4850, 2010.

[4] F. P. García Márquez, A. M. Tobias, J. M. Pinar Pérez, and M. Papaelias, "Condition monitoring of wind turbines: techniques and methods," *Renewable Energy*, vol. 46, pp. 169–178, 2012.

[5] W. Liu, B. Tang, and Y. Jiang, "Status and problems of wind turbine structural health monitoring techniques in China," *Renewable Energy*, vol. 35, no. 7, pp. 1414–1418, 2010.

[6] X. Chen, J. Li, and H. Cheng, "Research and application of condition monitoring and fault diagnosis technology in wind turbines," *Chinese Journal of Mechanical Engineering*, vol. 47, no. 9, pp. 47–52, 2011.

[7] F. Combet and L. Gelman, "Optimal filtering of gear signals for early damage detection based on the spectral kurtosis," *Mechanical Systems and Signal Processing*, vol. 23, no. 3, pp. 652–668, 2009.

[8] H. Endo and R. B. Randall, "Enhancement of autoregressive model based gear tooth fault detection technique by the use of minimum entropy deconvolution filter," *Mechanical Systems and Signal Processing*, vol. 21, no. 2, pp. 906–919, 2007.

[9] J. Li, X. Chen, Z. Du, Z. Fang, and Z. He, "A new noise-controlled second-order enhanced stochastic resonance method with its application in wind turbine drivetrain fault diagnosis," *Renewable Energy*, vol. 60, pp. 7–19, 2013.

[10] F. Combet and L. Gelman, "An automated methodology for performing time synchronous averaging of a gearbox signal without speed sensor," *Mechanical Systems and Signal Processing*, vol. 21, no. 6, pp. 2590–2606, 2007.

[11] T. Heyns, P. S. Heyns, and J. P. de Villiers, "Combining synchronous averaging with a Gaussian mixture model novelty detection scheme for vibration-based condition monitoring of a gearbox," *Mechanical Systems and Signal Processing*, vol. 32, pp. 200–215, 2012.

[12] Q. He, Z. Feng, and F. Kong, "Detection of signal transients using independent component analysis and its application in gearbox condition monitoring," *Mechanical Systems and Signal Processing*, vol. 21, no. 5, pp. 2056–2071, 2007.

[13] J. Wang, R. X. Gao, and R. Yan, "Integration of EEMD and ICA for wind turbine gearbox diagnosis," *Wind Energy*, vol. 17, no. 5, pp. 757–773, 2014.

[14] P. von Bünau, F. C. Meinecke, F. Király, and K.-R. Müller, "Finding stationary subspaces in multivariate time series," *Physical Review Letters*, vol. 103, no. 21, Article ID 214101, 2009.

[15] H. Zeng, A. Song, R. Yan, and H. Qin, "EOG artifact correction from EEG recording using stationary subspace analysis and empirical mode decomposition," *Sensors*, vol. 13, no. 11, pp. 14839–14859, 2013.

[16] D. A. J. Blythe, P. Von Bunau, F. C. Meinecke, and K.-R. Muller, "Feature extraction for change-point detection using stationary subspace analysis," *IEEE Transactions on Neural Networks and Learning Systems*, vol. 23, no. 4, pp. 631–643, 2012.

[17] P. von Bunau, F. C. Meinecke, S. Scholler, and K. Muller, "Finding stationary brain sources in EEG data," in *Proceedings of the Annual International Conference of the IEEE Engineering in Medicine and Biology Society (EMBC '10)*, pp. 2810–2813, Buenos Aires, Argentina, August-September 2010.

[18] S. Hara, Y. Kawahara, T. Washio, P. von Bünau, T. Tokunaga, and K. Yumoto, "Separation of stationary and non-stationary sources with a generalized eigenvalue problem," *Neural Networks*, vol. 33, pp. 7–20, 2012.

[19] F. C. Meinecke, P. von Bünau, M. Kawanabe, and K.-R. Müller, "Learning invariances with stationary subspace analysis," in

Proceedings of the IEEE 12th International Conference on Computer Vision Workshops (ICCV '09), pp. 87–92, Kyoto, Japan, September-October 2009.

[20] B. Tang, W. Liu, and T. Song, "Wind turbine fault diagnosis based on Morlet wavelet transformation and Wigner-Ville distribution," *Renewable Energy*, vol. 35, no. 12, pp. 2862–2866, 2010.

[21] R. Errichello and J. Muller, "Gearbox reliability collaborative gearbox 1 failure analysis report," Tech. Rep., Geartech, Townsend, Mont, USA, 2010.

[22] R. Yan and R. X. Gao, "Base wavelet selection for bearing vibration signal analysis," *International Journal of Wavelets, Multiresolution and Information Processing*, vol. 7, no. 4, pp. 411–426, 2009.

[23] J. Lin and L. Qu, "Feature extraction based on morlet wavelet and its application for mechanical fault diagnosis," *Journal of Sound and Vibration*, vol. 234, no. 1, pp. 135–148, 2000.

[24] Y. Jiang, B. Tang, Y. Qin, and W. Liu, "Feature extraction method of wind turbine based on adaptive Morlet wavelet and SVD," *Renewable Energy*, vol. 36, no. 8, pp. 2146–2153, 2011.

[25] J. Wang, R. X. Gao, and R. Yan, "Multi-scale enveloping order spectrogram for rotating machine health diagnosis," *Mechanical Systems and Signal Processing*, vol. 46, no. 1, pp. 28–44, 2014.

[26] E. T. Jaynes, "Information theory and statistical mechanics," *Physics Review*, vol. 106, no. 4, pp. 620–630, 1957.

[27] K. Pandžić and M. Kisegi, "Principal Component analysis of a local temperature field within the global circulation," *Theoretical and Applied Climatology*, vol. 41, no. 4, pp. 177–200, 1990.

[28] J. Bendat and A. Piersol, *Random Data Analysis and Measurement Procedures*, John Wiley & Sons, New York, NY, USA, 3rd edition, 2000.

[29] A. Konrad, B. Y. Zhao, A. D. Joseph, and R. Ludwig, "A Markov-based channel model algorithm for wireless networks," *Wireless Networks*, vol. 9, no. 3, pp. 189–199, 2003.

[30] F. Bellini and G. F. Talamanca, "Runs tests for assessing volatility forecastability in financial time series," *European Journal of Operational Research*, vol. 163, no. 1, pp. 102–114, 2005.

[31] E. J. Chen and W. D. Kelton, "Determining simulation run length with the runs test," *Simulation Modelling Practice and Theory*, vol. 11, no. 3-4, pp. 237–250, 2003.

[32] T. W. Beck, T. J. Housh, J. P. Weir et al., "An examination of the Runs Test, Reverse Arrangements Test, and modified Reverse Arrangements Test for assessing surface EMG signal stationarity," *Journal of Neuroscience Methods*, vol. 156, no. 1-2, pp. 242–248, 2006.

[33] Y. Oyague, "Gearbox modeling and load simulation of abaseline 730-kW wind turbine using state-of-the-art simulation codes," Technique Report NREL/TP-500-41160, U.S. National Renewable Energy Laboratory, Golden, Colo, USA, 2009.

Hindawi Publishing Corporation
Journal of Sensors
Volume 2015, Article ID 961894, 9 pages
http://dx.doi.org/10.1155/2015/961894

Research Article

Rectifier Fault Diagnosis and Fault Tolerance of a Doubly Fed Brushless Starter Generator

Liwei Shi and Zhou Bo

School of Traffic & Vehicle Engineering, Shandong University of Technology, Zibo, Shandong 250049, China

Correspondence should be addressed to Liwei Shi; liwei10@nuaa.edu.cn

Received 25 August 2014; Accepted 7 October 2014

Academic Editor: Sergiu Dan Stan

This paper presents a rectifier fault diagnosis method with wavelet packet analysis to improve the fault tolerant four-phase doubly fed brushless starter generator (DFBLSG) system reliability. The system components and fault tolerant principle of the high reliable DFBLSG are given. And the common fault of the rectifier is analyzed. The process of wavelet packet transforms fault detection/identification algorithm is introduced in detail. The fault tolerant performance and output voltage experiments were done to gather the energy characteristics with a voltage sensor. The signal is analyzed with 5-layer wavelet packets, and the energy eigenvalue of each frequency band is obtained. Meanwhile, the energy-eigenvalue tolerance was introduced to improve the diagnostic accuracy. With the wavelet packet fault diagnosis, the fault tolerant four-phase DFBLSG can detect the usual open-circuit fault and operate in the fault tolerant mode if there is a fault. The results indicate that the fault analysis techniques in this paper are accurate and effective.

1. Introduction

A starter generator can start the engine and supply electrical power for the aeronautics and automobiles. A variable frequency starter generator is developed for the Boeing 787 which is introduced in [1]. The switched reluctance machine (SRM) [2] and the PM machine [3] were also considered as starter generators. However, the controlled power electronic circuit for switched reluctance generator is very complex and expensive. And the PM material is very strict with the working temperature [4, 5]. It is difficult for both of the SRM and PM machine to regulate the output voltage when they work as generators.

Doubly fed brushless starter generator (DFBLSG) is a new type of brushless DC machine that comes from doubly salient PM machine by using field winding instead of permanent magnet steel [6]. Its armature windings and excitation windings are both mounted on the salient poles of the stator, and it has similar salient rotor structure to SRM rotor. As a generator, DFBLSG does not need rotor position information and controlled power electronic circuit in the SRM generator. DFBLSG has such advantages as simple structure, low cost, high reliability, and good fault tolerance. Thus it has good application prospects in many fields including wind power generation, aeronautics, astronautics, automobiles, and ships [7]. In particular, it can be employed as aeronautics starter generator because it has excellent performance on both power generation and starting [8, 9].

The fault tolerant schematic of a machine system is shown in Figure 1. When a multiphase machine with more than three phases is implemented in the system, it can continue operating even with one or two open-circuit phases at the monitor of deferent sensors. So, it is necessary to build a system for fault tolerant application with the fault detecting sensors and controller [10, 11].

Generating mode is of particular importance for the starter and generator. As a weak part of the doubly fed brushless generator system, the rectifier is prone to failure. Practice shows that the faults of rectifier could be divided into short-circuit fault and open-circuit fault. Short-circuit fault would result in stopping operation by a fuse [8]. On occurrence of open-circuit fault, the unbalanced operating condition of rectification circuit would cause output voltage variation, phase current distortion, and even system crashes. Therefore, the research on rectifier faults detecting for doubly fed brushless starter generator is significantly important.

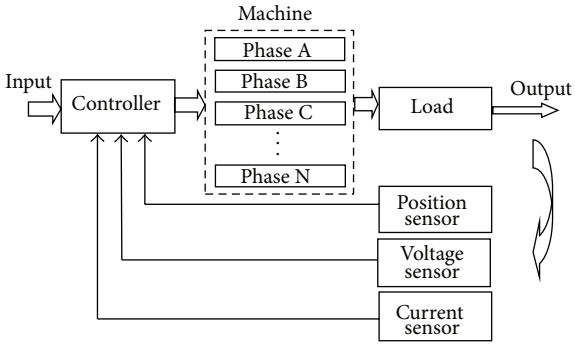

Figure 1: Fault tolerant schematic of a machine system.

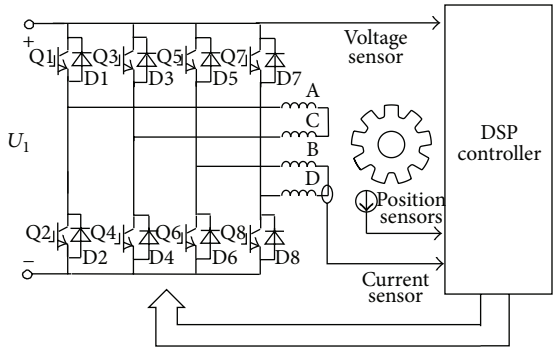

Figure 2: The system of the DFBLSG.

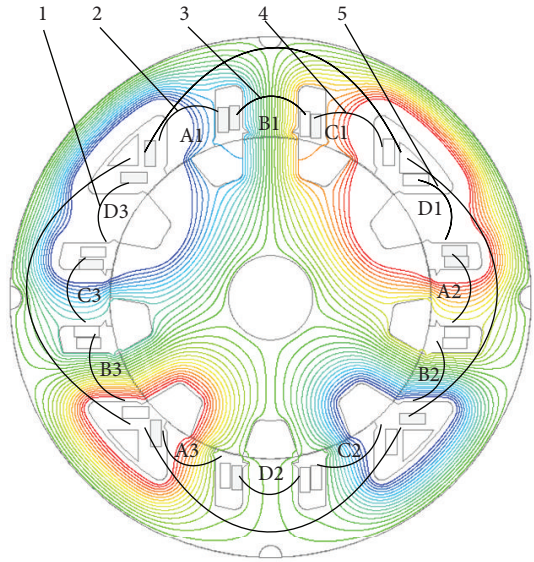

Figure 3: The structure and magnetic flux of the DFBLSG.

Recently, there are many different methods raised for rectifier fault diagnosis applications. The primary idea is diagnosing fault information included in output voltage. To detect the fault of a rectifier with 12 phases, an approach is given on the basis of voltage analysis with voltage eigenvalue in [12]. An extended Kalman filter is used to estimate the unknown model parameters for nonlinear dynamic systems [13]. Fourier transform and wavelet analysis has been used in fault diagnosis in [14–16]. In [14], a novel method for gearbox fault detection based on biorthogonal B-spline wavelet was proposed. And in [15], an automatic identification method for the leakage signal of petroleum pipeline is studied. The wavelet analysis is used to process the input signal because it has the superiority of varied size of the analysis window to the frequency [16].

This paper proposed a fault tolerant four-phase DFBLSG and presents a rectifier fault diagnosis method with wavelet packet analysis. The system components and fault tolerant principle of the 12/9-pole high reliable DFBLSG are given. And the common fault of the rectifier is analyzed. The process of wavelet packet transforms fault detection/identification algorithm is introduced in detail. The output voltage signal detected by a voltage sensor is used as a wavelet packet input signal. And the experiments were done to gather the energy characteristics. The wavelet coefficients were obtained from wavelet packet analysis of fault voltage signals, and then the wavelet reconstruction of each frequency band was processed. Meanwhile, the energy-eigenvalue tolerance was introduced to improve the diagnostic accuracy. With the wavelet packet fault diagnosis, the fault tolerant four-phase DFBLSG can detect the usual open-circuit fault and operate in the fault tolerant mode if there is a fault. The results indicate that the fault analysis techniques in this paper are accurate and effective.

2. System Components and Principle

2.1. System Components. The DFBLSG comprises machine body and its controller, as shown in Figure 2. A four-phase full-bridge inverter is used for DFBLSG drive. Phase A and phase C connect in series, and they build up an independent channel. The other channel is composed of phase B and phase D. The position sensors are employed to detect the rotor position and rotor speed on the starting mode. And a voltage sensor is used to detect the rectifier fault. The controller is utilized to control the output voltage, the rotating of the machine, and the fault detection.

When the DFBLSG works as a generator, all the switched tubes are turned off and four-phase output voltage is rectified by the eight diodes. The output voltage is stabilized by adjusting the field winding current under the monitor of a voltage sensor.

The starter generator can output 14 V DC source for the motor when it runs as a generator. The 12 V DC battery can supply DC source when the machine is required to start the engine.

2.2. Structure and Principle of DFBLSG. Figure 3 shows the structure of the novel four-phase photograph. It is different with the traditional 12/8-pole three-phase machine [17], because it has 12 stator poles and 9 rotor poles (Table 2).

Obviously, each phase winding consists of three concentrated coils. For example, phase A consists of A1, A2, and A3, which are connected in series, as shown in Figure 3. It should be noted that the phase winding direction of this configuration is different from the topology in of the traditional four-phase DFBLSG, which wounds the field coils

Table 1: Classification of diode open faults.

Item	Fault type	Example
T1	One diode or two diodes of the same loop open circuit	D1, D3, D5, D7, D2, D4, D6, D8, D1D4, D3D2, D5D8, D7D6
T2	Other two diodes or more of the same channel open circuit	D1D3, D5D7, D2D4, D6D8, D1D2, D3D4, D5D6, D7D8, D1D2D3
T3	Two diodes of the different channel open circuit	D1D5, D3D7, D2D6, D4D8, D1D6, D1D8, D3D6, D3D8, D5D2, D5D4, D7D2, D7D4
T4	Three diodes of the different channel open circuit	D1D2D5, D1D2D6

Table 2: Key parameters of the generator.

Item	Data
Number of stator poles	12
Number of rotor poles	9
Stator outer diameter (mm)	136
Rotor outer diameter (mm)	83.5
Air gap (mm)	0.25
Axle length (mm)	40
Stator tooth height (mm)	13.8
Stator yoke height (mm)	12
Stator pole arc coefficient	0.667
Rotor pole arc coefficient	0.5
Rated power (W)	300
Rated voltage (V)	14

around four stator poles. But both of them have the same direction as the field coils. The phase windings of the two sections are not connected directly. Therefore, there are two channels, which are labeled as A, C and B, D.

2.3. Rectifier and Its Fault. The traditional three-phase generator has three types of rectifiers [18], which are positive full-bridge rectifier, half-wave rectifier, and negative half-wave rectifier. Similarly, the four-phase DFBLSG can also use the above rectifiers. The four-phase full-bridge rectifier shown in Figure 4, which has two independent output channels, is studied because it has the ability of fault isolation.

Rectifier is the weaknesses of the power generation system. Potential faults of the DFBLSG can be divided into short circuit and open circuit. Because the short-circuit faults are very harmful to the system, it should be protected by a fuse. Hence, this paper will mainly study diode open-circuit faults including single diode open-circuit and double diodes open-circuit faults.

On occurrence of open faults, the output voltage would be distorted in accordance with certain laws. For example, when D1 and D2 are open, the output voltage will be distorted in the first half period. So, the diode open faults can be classified into 4 types according to distortion laws of waveform, as shown in Table 1.

3. Fault Detection Process

In Figure 2, the voltage is detected by a voltage sensor and the analog voltage signal is sent to DSP after conditioning. Then DSP controller analyzed the sampled signal and select

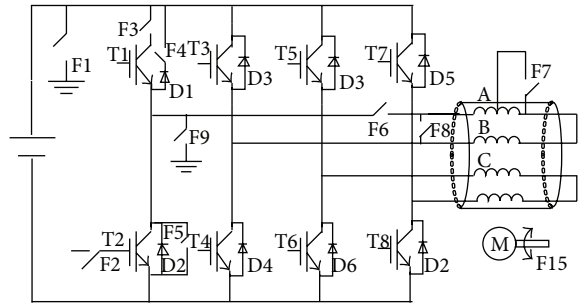

Figure 4: Potential faults of the DFBLSG.

fault energy eigenvalue with a wavelet packet firstly. Then, the eigenvalue is compared with a sample stored in DSP controller. If the fault condition is reached, the DSP will make appropriate decisions and output fault indication signal through the I/O port.

The fault detection process includes the following steps.

(1) Analyze the normalized voltage sampling signal with the wavelet packet, let the decomposed layer be j, and extract wavelet coefficient of every band [19].

The normalized equation of array $[P_i]$ can be described as

$$P_i' = \frac{P_i - P_{\min}}{P_{\max} - P_{\min}}. \quad (1)$$

(2) Reconstruct the decomposition coefficients of the wavelet packet and extract the signal from every band.

(3) Calculate each band signal energy eigenvalues according to

$$E_{2^j}^k = \sum_{i=1}^{N} \left|e_k(i)\right|^2, \quad k = 0, 1, \ldots, 2^{j-1}, \quad (2)$$

where $e_k(i)$ is the discrete points amplitude of the reconstructed signal.

(4) Build the fault characteristic vector T that has 2^j elements with the signal energy of each frequency band:

$$T = \left[E_{2^j}^0, E_{2^j}^1, \ldots, E_{2^j}^{2^j-1}\right]. \quad (3)$$

To eliminate the influence of voltage amplitude, a new characteristic vector should be built with the element of

$$s_k = \frac{E_{2^j}^k}{E} = \frac{\sum_{i=1}^{N} \left|e_k(i)\right|^2}{\sum_{i=1}^{2^{j-1}} E_{2^j}^k}, \quad k = 0, 1, \ldots, 2^{j-1}. \quad (4)$$

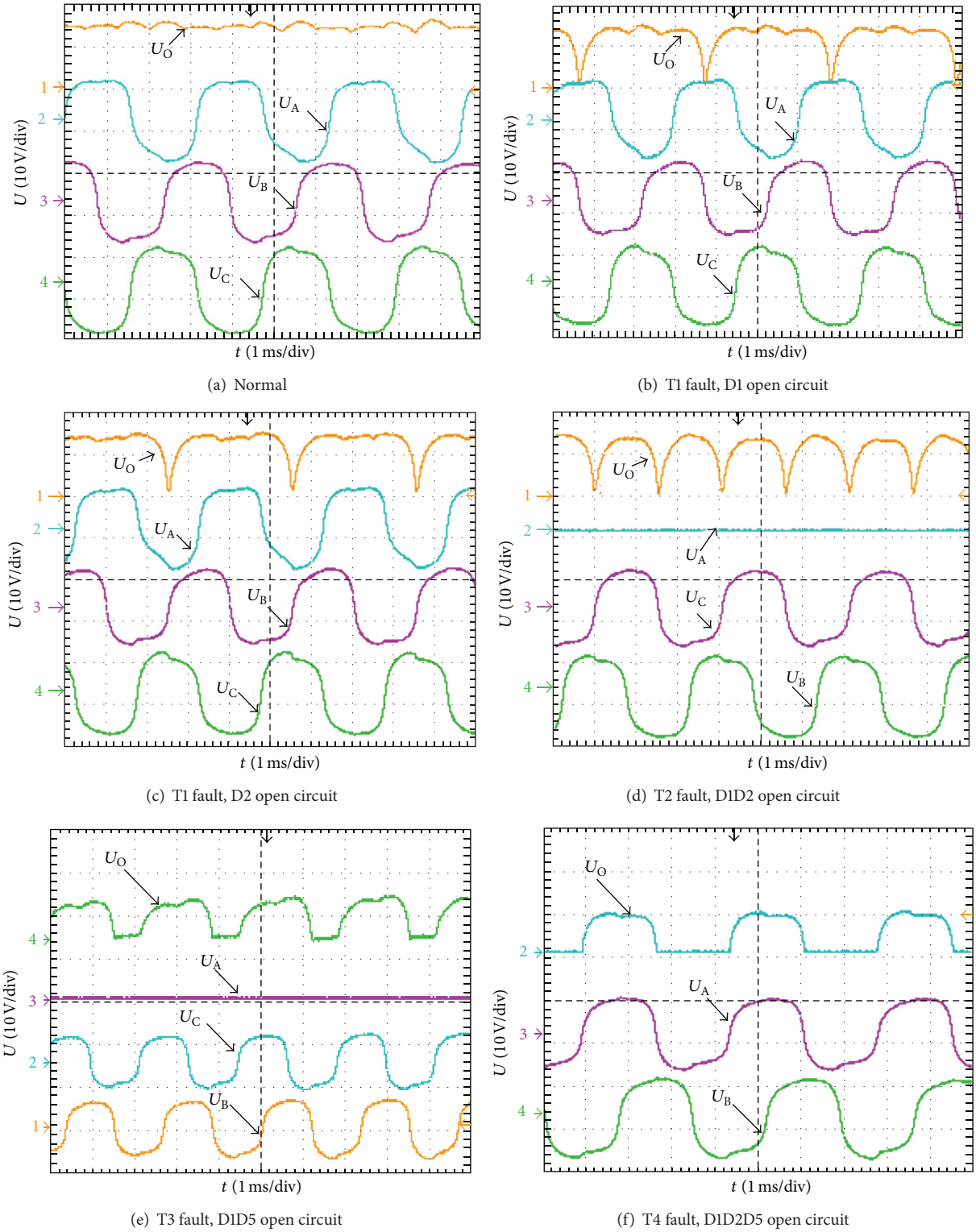

(a) Normal

(b) T1 fault, D1 open circuit

(c) T1 fault, D2 open circuit

(d) T2 fault, D1D2 open circuit

(e) T3 fault, D1D5 open circuit

(f) T4 fault, D1D2D5 open circuit

Figure 5: Voltage waveforms under normal and one phase open-circuit fault.

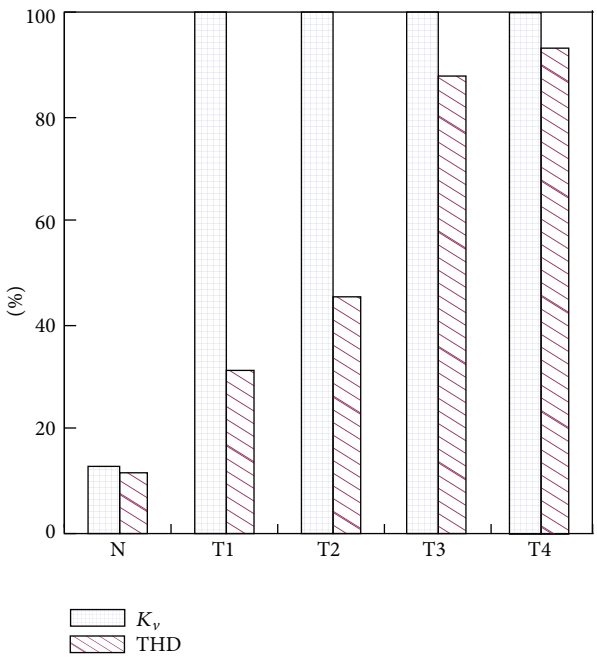

Figure 6: Voltage pulsating ratio and THD under normal and open-circuit fault. N: normal; T1 fault, D1 open circuit; T2 fault, D1D2 open circuit; T3 fault, D1D5 open circuit; T4 fault, D1D2D5 open circuit.

And the new characteristic vector is shown as

$$T = \left[s_0, s_1, \ldots, s_{2^j-1}\right]. \tag{5}$$

(5) Establish the sample fault file. We should collect a large number of experimental data samples, and then the fault characteristic vector can be determined with the statistical average value of the sample.

The statistical average value can be calculated with

$$C_k = \sum_{l=1}^{N} \frac{s_k(l)}{n}, \quad k = 0, 1, \ldots, 2^{j-1}, \tag{6}$$

where n is the number of experimental times.

The error discriminant vector ΔP is used to describe the tolerance range of statistical average value C_k, and the element of ΔP can be caculated by:

$$\Delta C_k = K\sigma = K\sqrt{\frac{1}{N}\sum_{l=1}^{N}\left[s_k(l) - C_k\right]^2}, \tag{7}$$

where σ is the sample standard deviation and K is the tolerance factor, generally taken to be 1.

Equation (6) establishes mappings between energy feature vector and fault state. With the obtained fault mode parameter, a table that describes the relationship between fault state and change parameter is stored in DSP. Then the faults can be identified and displayed.

4. Experiments and Wavelet Packet Analysis Conclusions

4.1. Prototype Experiments. A four-phase full-bridge rectifier was built in the experimental bench. The prototype machine operating in normal state and fault state was tested. Figure 5(a) shows the voltage waveform when the machine has no fault. Figures 5(b) and 5(c) display the voltage waveform with one diode open circuit. The other two diodes or more of the same channel open-circuit fault, two diodes of the different channel open-circuit fault, and three diodes of the different channel open-circuit fault were shown in Figures 5(d)–5(f), respectively.

The equation for calculation the voltage ripple is shown in

$$K_v = \frac{U_{\max} - U_{\min}}{U_o}. \tag{8}$$

And the total harmonic distortion (THD) of voltage is expressed as

$$\mathrm{THD} = \frac{\sqrt{\sum_2^{\infty} V_i^2}}{V_1} \times 100\%. \tag{9}$$

With the fast Fourier transform analysis of the voltage waveform obtained from the oscilloscope, the normal and various fault voltage ripple ratio and THD can be drawn in Figure 6. As can be seen from the figure, the four-phase full-bridge rectifier can tolerate the fault list in Table 1. But the voltage ripple and THD are very high when there is an open-circuit fault. So the in time detection of fault type is very necessary for us to relieve the negative influence of this voltage ripple.

Figure 7 presents the photograph of the generator and the controller. Figure 8(a) shows the nonload characteristic with a four-phase full bridge. And the external characteristic under different fault is shown in Figure 8(b) when the excitation current is 4A. From the figure, we can see that the generator can tolerate one-diode open-circuit faults well, because the other diode in the same leg can rectify the positive or negative current. Comparing the characteristics curves under various faults, the output voltage of single phase open circuit fault is lower than one diode open-circuit fault. The characteristic experiments results show the same conclusion with the voltage waveforms in Figure 5. Because the number of phase windings is relatively small, the external characteristic of the machine is "hard" compared to common generators. When there is a failure, the DFBLSG can achieve fault tolerance by increasing the field current or outputting a relatively low power with the same field current.

4.2. Wavelet Packet Analysis. The rectified voltage sampling frequency is 50 kHz, the sample length of oscilloscope is 2500, and the sampling repeated 10 times. According to the above diagnostic methods, we use db1 wavelet as the bases wave to carry out the wavelet packet analysis. The wavelet packet decomposition tree is shown in Figure 9 and the decomposition layer $j = 5$. As an example, Figure 10 presents

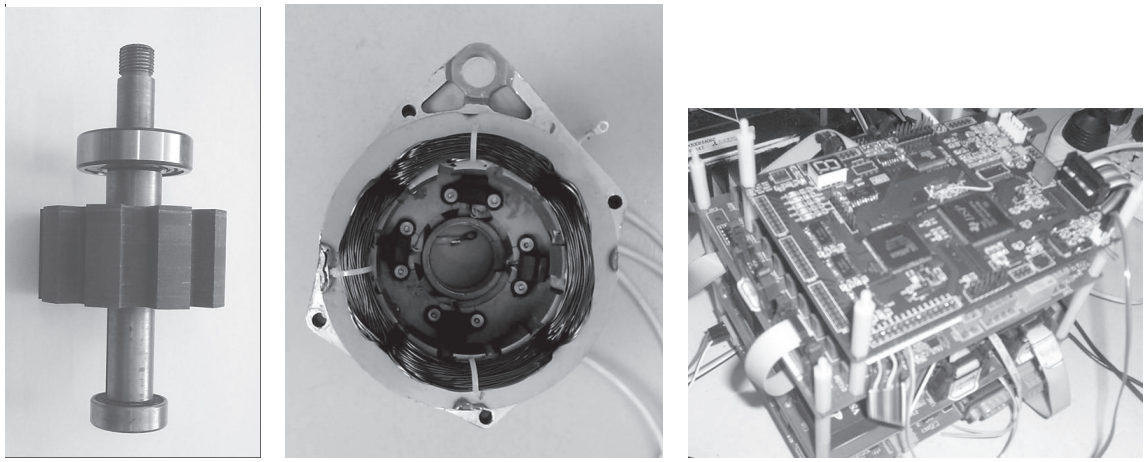

(a) Rotor (b) Stator (c) DSP controller

Figure 7: Rotor, stator, and controller photograph.

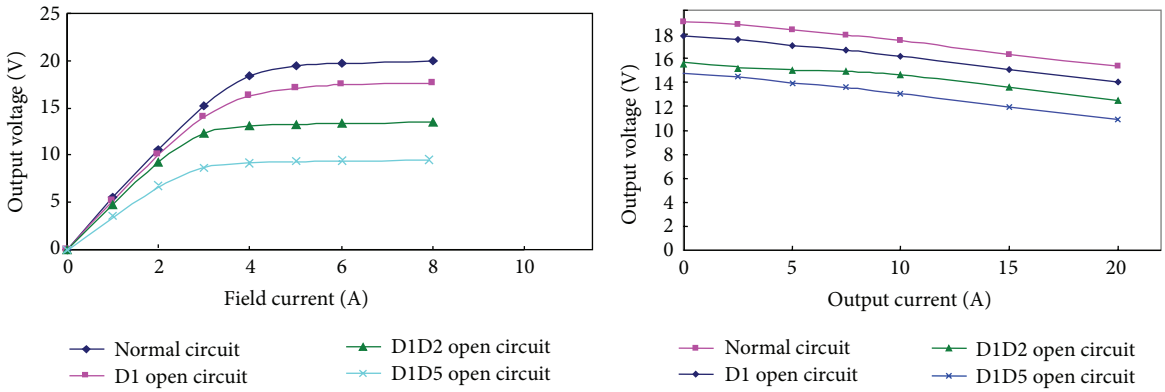

(a) Nonload characteristic (b) External characteristic

Figure 8: Characteristic experiments results with full bridge mode.

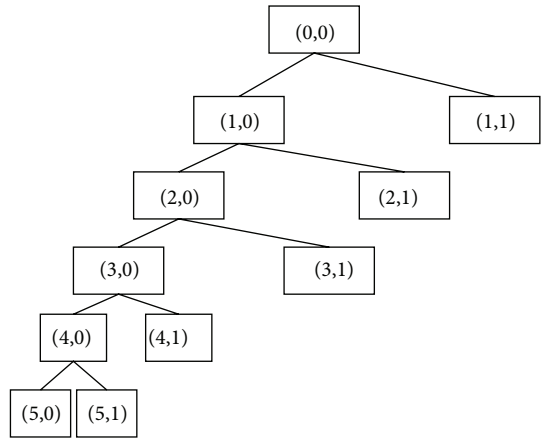

Figure 9: The five-layer wavelet packet decomposition tree.

the wavelet packet decomposition results of deferent band. Because the waveform describes a relative energy size, it has no unit.

Table 3: Energy-eigenvalue tolerance statistic on each fault condition.

	ΔC_1	ΔC_2	ΔC_3	ΔC_4	ΔC_5
Normal	0.008	0.0027	0.0027	0	0.0027
D1	0.075	0.0023	0.008	0.004	0.004
D1D1 open circuit	0.11	0.041	0.010	0.0032	0.0032
D1D5 open circuit	0.04	0.001	0.0003	0.0003	0.0003
D1D2D5 open circuit	0.16	0.05	0.0012	0.0006	0.0006

The energy eigenvalue statistic on each fault condition is shown in Figure 11. From the figure, we can see that the element vector data after 6th harmonic is almost zero. So these frequency band energy eigenvalues have no practical significance, and they can be negligible.

With (7), we can get the energy-eigenvalue tolerance statistic on each fault condition (Table 3).

If the system is normal, the energy characteristics of all the frequency bands are very little. If D1 is open circuit, characteristic of the first frequency band is high. If D1 and

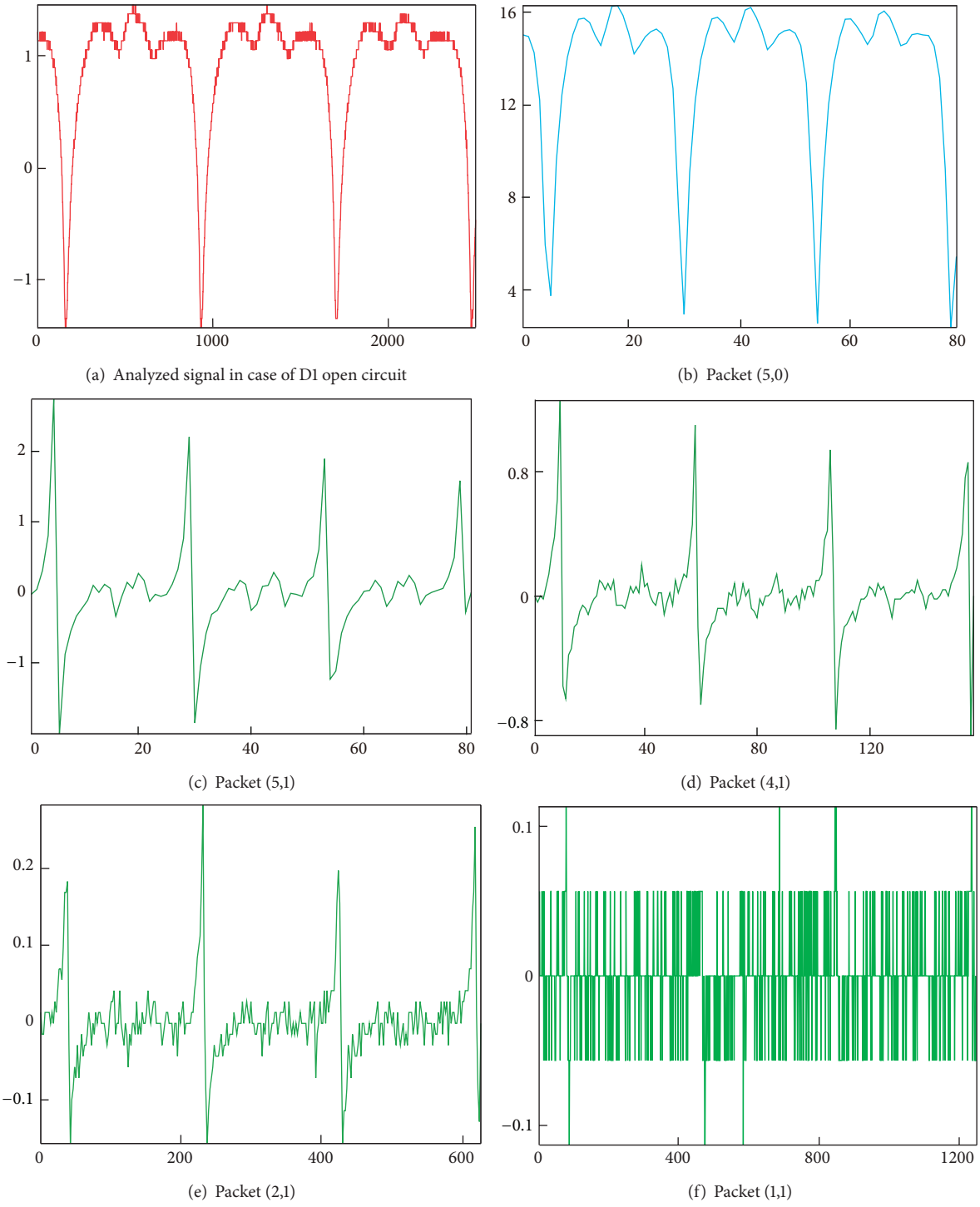

Figure 10: The wavelet packet decomposition results.

D2 are open circuit, the energy characteristic of the second frequency band is higher than the one of the first band. If there is an open-circuit fault on D1D5, the first and the second frequency band are almost the same. All the energy characteristics are very high if there is a D1D2D5 open-circuit fault.

The experiments prove that when the generator rectifier circuit fails, the wavelet packet analysis results of voltage on the sampling signal can be used for the fault diagnosis. With the established relationship between energy characteristics and fault state, the open-circuit fault can be recognized by the wavelet packet analysis.

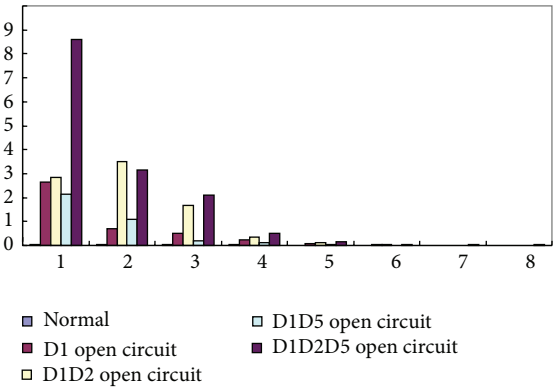

Figure 11: Energy eigenvalue statistic on each fault condition.

5. Conclusions

The doubly fed brushless starter generator has broad application prospects in the aerospace and automotive industry, which need high reliability for the whole system. To meet the requirement of the fault tolerant capability, a four-phase DFBLSG which has the characteristic of phase redundancy, phase isolation, and fault diagnosis is presented in this paper. As the weak part of the system, the rectifier faults are divided into one diode or two diodes of the same loop open circuit, two diodes of the same channel open-circuit, two diodes of the different channel open circuit, and three diodes of the different channel open circuit.

To detect the open-circuit fault of the rectifier, a rectifier fault diagnosis method with wavelet packet analysis is presented. Wavelet packet analysis can decompose the voltage signal into several layers in the whole frequency range. With the energy eigenvalues extracted from full-band wavelet packet, eigenvectors can be established to describe different faults. The fault tolerant performance and output voltage experiments were done to gather the energy characteristics with a voltage sensor. With the established relationship between energy characteristics and fault state, the open-circuit fault can be diagnosed by the wavelet packet analysis.

Conflict of Interests

The authors declare that there is no conflict of interests regarding the publication of this paper.

Acknowledgments

This paper is financially supported by the Natural Science Foundation of Shandong (no. ZR2012EM011). The authors would like to thank APSC in Nanjing University of Aeronautics and Astronautics.

References

[1] Z. Chen, H. Wang, and Y. Yan, "A doubly salient starter/generator with two-section twisted-rotor structure for potential future aerospace application," *IEEE Transactions on Industrial Electronics*, vol. 59, no. 9, pp. 3588–3595, 2012.

[2] W. Ding and D. Liang, "A fast analytical model for an integrated switched reluctance starter/generator," *IEEE Transactions on Energy Conversion*, vol. 25, no. 4, pp. 948–956, 2010.

[3] H. Mirahki, M. Moallem, and S. A. Rahimi, "Design optimization of IPMSM for 42 v integrated starter alternator using lumped parameter model and genetic algorithms," *IEEE Transactions on Magnetics*, vol. 50, no. 3, pp. 114–119, 2014.

[4] C. Liu, K. T. Chau, and X. Zhang, "An efficient wind-photovoltaic hybrid generation system using doubly excited permanent-magnet brushless machine," *IEEE Transactions on Industrial Electronics*, vol. 57, no. 3, pp. 831–839, 2010.

[5] D. Lee, Y.-H. Jeong, and S.-Y. Jung, "Design of wound rotor synchronous machine for ISG and performance comparison with interior permanent magnet synchronous machine," *Transactions of the Korean Institute of Electrical Engineers*, vol. 62, no. 1, pp. 37–42, 2013.

[6] Y. Du, K. T. Chau, M. Cheng, Y. Fan, W. Zhao, and F. Li, "A linear stator permanent magnet vernier HTS machine for wave energy conversion," *IEEE Transactions on Applied Superconductivity*, vol. 22, no. 3, Article ID 5202505, 2012.

[7] Z. Zhang, Y. Yan, and Y. Tao, "A new topology of low speed doubly salient brushless DC generator for wind power generation," *IEEE Transactions on Magnetics*, vol. 48, no. 3, pp. 1227–1233, 2012.

[8] L. Sun, Z. Zhang, and L. Qian, "Calculation and analysis of iron loss in Doubly Salient Brushless DC generator," in *Proceedings of the 39th Annual Conference of the IEEE Industrial Electronics Society*, pp. 2650–2655, November 2013.

[9] L. Zhang, B. Zhou, Y.-S. Zhang, F.-S. Cheng, and J.-D. Wei, "Analysis and suppression of torque ripple for doubly salient electro-magnetic motor," *Proceedings of the Chinese Society of Electrical Engineering*, vol. 30, no. 3, pp. 83–89, 2010.

[10] W. Cao, B. C. Mecrow, G. J. Atkinson, J. W. Bennett, and D. J. Atkinson, "Overview of electric motor technologies used for more electric aircraft (MEA)," *IEEE Transactions on Industrial Electronics*, vol. 59, no. 9, pp. 3523–3531, 2012.

[11] W. Xu, J. Zhu, Y. Zhang, and J. Hu, "Cogging torque reduction for radially laminated flux-switching permanent magnet machine with 12/14 poles," in *Proceedings of the 37th Annual Conference of the IEEE Industrial Electronics Society (IECON '11)*, pp. 3590–3595, Melbourne, Australia, November 2011.

[12] C.-F. Zhang, M. Yan, J. He, C. Luo, and Y.-Y. Xiao, "Current sensor fault diagnosis for doubly-fed wind generator control system," *Information Technology Journal*, vol. 12, no. 18, pp. 4368–4373, 2013.

[13] S. Mariani and A. Ghisi, "Unscented Kalman filtering for nonlinear structural dynamics," *Nonlinear Dynamics*, vol. 49, no. 1-2, pp. 131–150, 2007.

[14] G. Zhang and Y. Ge, "A novel method for gearbox fault detection based on biorthogonal B-spline wavelet," *Sensors and Transducers*, vol. 133, no. 10, pp. 83–94, 2011.

[15] B. Zhou, J. Wang, S. Li, and W. Wang, "A new key predistribution scheme for multiphase sensor networks using a new deployment model," *Journal of Sensors*, vol. 2014, Article ID 573913, 10 pages, 2014.

[16] M. Aktaş, "A novel method for inverter faults detection and diagnosis in PMSM drives of HEVs based on discrete wavelet transform," *Advances in Electrical and Computer Engineering*, vol. 12, no. 4, pp. 33–38, 2012.

[17] F. Yang and Z. Chen, "Research on torque ripple of doubly salient electro-magnetic generator under no-load condition,"

Transactions of China Electrotechnical Society, vol. 28, no. 1, pp. 290–295, 2013.

[18] B. A. Welchko, T. A. Lipo, T. M. Jahns, and S. E. Schulz, "Fault tolerant three-phase AC motor drive topologies: a comparison of features, cost, and limitations," *IEEE Transactions on Power Electronics*, vol. 19, no. 4, pp. 1108–1116, 2004.

[19] X. Chen, G. Lin, and Y. Zhang, "Denoising method based on sparse representation for WFT signal," *Journal of Sensors*, vol. 2014, Article ID 145870, 10 pages, 2014.

Hindawi Publishing Corporation
Journal of Sensors
Volume 2015, Article ID 678120, 19 pages
http://dx.doi.org/10.1155/2015/678120

Research Article

Fault Line Selection Method of Small Current to Ground System Based on Atomic Sparse Decomposition and Extreme Learning Machine

Xiaowei Wang,[1] Yanfang Wei,[1] Zhihui Zeng,[1] Yaxiao Hou,[2] Jie Gao,[1] and Xiangxiang Wei[1]

[1]*School of Electrical Engineering and Automation, Henan Polytechnic University, Jiaozuo 454000, China*
[2]*School of Electrical Engineering and Automation, Harbin Institute of Technology, Harbin 150001, China*

Correspondence should be addressed to Xiaowei Wang; proceedings@126.com

Received 13 October 2014; Accepted 28 November 2014

Academic Editor: Sergiu Dan Stan

This paper proposed a fault line voting selection method based on atomic sparse decomposition (ASD) and extreme learning machine (ELM). Firstly, it adopted ASD algorithm to decompose zero sequence current of every feeder line at first two cycles and selected the first four atoms to construct main component atom library, fundamental atom library, and transient characteristic atom libraries 1 and 2, respectively. And it used information entropy theory to calculate the atom libraries; the measure values of information entropy are got. It constructed four ELM networks to train and test atom sample and then obtained every network accuracy. At last, it combined the ELM network output and confidence degree to vote and then compared the vote number to achieve fault line selection (FLS). Simulation experiment illustrated that the method accuracy is 100%, it is not affected by fault distance and transition resistance, and it has strong ability of antinoise interference.

1. Introduction

For small current to ground system, FLS study focus is fault line identified when single phase to ground fault occurred; at this moment, the fault current is weaker, and Petersen coil to ground mode also has the features. Therefore, the conventional method with using current amplitude size and phase information is difficult to obtain satisfactory results.

In recent years, modern signal processing technology used FLS to get fault characteristic information, such as wavelet transform [1], *S* transform [2], mathematical morphology [3], Hilbert-Huang transform (HHT) [4], Prony algorithm [5], and Hough transform [6]. Besides, the common method of FLS criterion had artificial neural networks [7], support vector machines [8], and Bayesian classification [9].

Zero sequence current was decomposed by wavelet transform and calculated wavelet modulus maxima to determine arrival time of traveling wave's head and then compared the amplitude and polarity of every feeder line at this time to achieve FLS [1]. It used *S* transform to get modulus value and phase angle of every frequency range and compared modulus value and phase angle to obtain characteristic frequency and voting mechanism, respectively; the experiments indicated that the method could not only judge the fault line accurately but also obtain the FLS confidence degree [2]. Paper [10] used *S* transform to get transient fault feature, and, based on the frequency point of transient maximum energy, it chose characteristic frequency sequence; therefore, the criterion with relative entropy values of multiple combination modes determined the fault section. Paper [3] proposed a novel method which was based on mathematical morphology; the method included two aspects: one used morphological filters to preprocess the data and removed the noise impact for FLS at the maximum extent and the other adopted morphological operators to detect the denoised signal with mutant aspect to judge the fault line. Paper [4] calculated transient

instantaneous power by Hilbert-Huang transform (HHT) and got fault direction well; the method took advantage of transient high-frequency component at lower sampling rate. It tried to divide the zero sequence current signal into several segments to ensure good continuity and smaller mutation at every subsegment, and Prony algorithm was applied to choose transient dominant component with maximum energy principle and then calculated the relative entropy and voted by preliminary vote and k values check to judge the fault line [5]. Hough transform was adopted to construct whole mutant direction angle which indicated overall trend of zero sequence current at initial stage, and FLS was achieved by distinguishing the direction angle [6]. Paper [7] replaced ordinary neurons with rough neurons and fuzzy neurons to identify 10 kinds of fault type; the method improved the training speed and reduced training samples and fault identification accuracy was enhanced. It used correlation coefficient of zero sequence voltage and charge as characteristic input to construct FLS process which was based on transient zero sequence Q-U features; the method adopted support vector machine algorithm with small sample [8]. For incomplete information of fault diagnosis, [9] adopted evidence uncertainty reasoning and compared abnormal events to reduce computation amount.

This paper proposed a novel FLS method which was based on combination of ASD and ELM. Firstly, it used atomic sparse algorithm to decompose zero sequence current of every feeder line and extracted the first four atoms to construct fault sample library, respectively; besides, it calculated information entropy measure of every library. Then, it trained the ELM network to improve network output accuracy. At last, fault voting was adopted to vote every feeder line and compared the values, and then the fault line was judged. Simulation results showed that the accuracy rate of proposed method is 100% and had strong ability of antinoise interference.

The remaining of this paper is organized as follows. In Section 2, we analyzed the physical characteristics of zero sequence current. In Sections 3 and 4, the theory of time-frequency atom decomposition and ELM work principle are presented, respectively. In Section 5, test signals analysis is given in the paper. In Section 6, we chose the characteristic atoms of zero sequence current. In Section 7, the FLS methods are proposed. In Section 8, example analysis is applied to verify the proposed method. In Section 9, we discussed the applicability of the method. In Section 10, the paper is completed with conclusions and future directions.

2. Physical Characteristics Analysis

Transient zero sequence circuit of single phase to ground fault is shown in Figure 1, where C_0 and L_0 are zero sequence capacitance and inductance, respectively, R_g is transition resistance of grounding point, R_p and L_p are equivalent resistance and inductance of arc suppression coil, and $e(t)$ is zero sequence voltage.

When the fault occurred in compensation network, Figure 1, the transient zero sequence current flows through

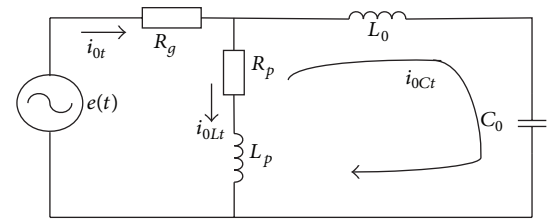

Figure 1: Transient zero sequence equivalent circuit of single phase to ground.

fault location [11, 12]; the calculation is shown in the following formula:

$$\begin{aligned} i_{0t} &= i_{0Lt} + i_{0Ct} \\ &= I_{Lm}\cos\varphi e^{-t/\tau_L} + I_{Cm} \\ &\quad \times \left(\frac{\omega_f}{\omega}\sin\varphi\sin\omega t - \cos\varphi\cos\omega_f t\right) e^{-\delta t}, \end{aligned} \tag{1}$$

where i_{0Lt} and i_{0Ct} are inductance component and capacitance component of transient zero sequence current, I_{Lm} and I_{Cm} are initial value of inductance current and capacitance current, respectively, ω is angular frequency, ω_f and δ are oscillation angle frequency and attenuation coefficient of transient zero sequence current capacitance component, respectively, τ_L is decay time constant of inductance current, and φ is initial phase of fault line.

ω_f and δ calculations are shown in the following formula, respectively:

$$\omega_f = \sqrt{\left|\frac{1}{L_0C_0} - \left(\frac{R_g}{2L_0}\right)^2\right|}, \tag{2}$$

$$\delta = \frac{R_g}{2L_0}. \tag{3}$$

Transient zero sequence current is comprised of sinusoidal function from formula (1), and its waveform has attenuation characteristics. It can be seen from formula (2) and (3) that oscillation angle frequency ω_f is influenced by L_0, C_0, and R_g; attenuation coefficient δ is also influenced by L_0 and R_g; when transition resistance R_g increased, ω_f decreased and δ increased; it reflected that wave oscillation trend of zero sequence current becomes slow and the attenuation time become fast, and then transient process will end soon and into steady state. Therefore, if it could extract accurately transient component to achieve FLS exactly at the large resistance to ground fault, it will be an important index to test the applicability of the FLS methods.

Figure 2 is zero sequence current of actual distribution network when overhead line 1 caused fault; it can be seen from Figure 2 that, whether the overhead line, cable line, or hybrid line, its zero sequence current has oscillation attenuation characteristics.

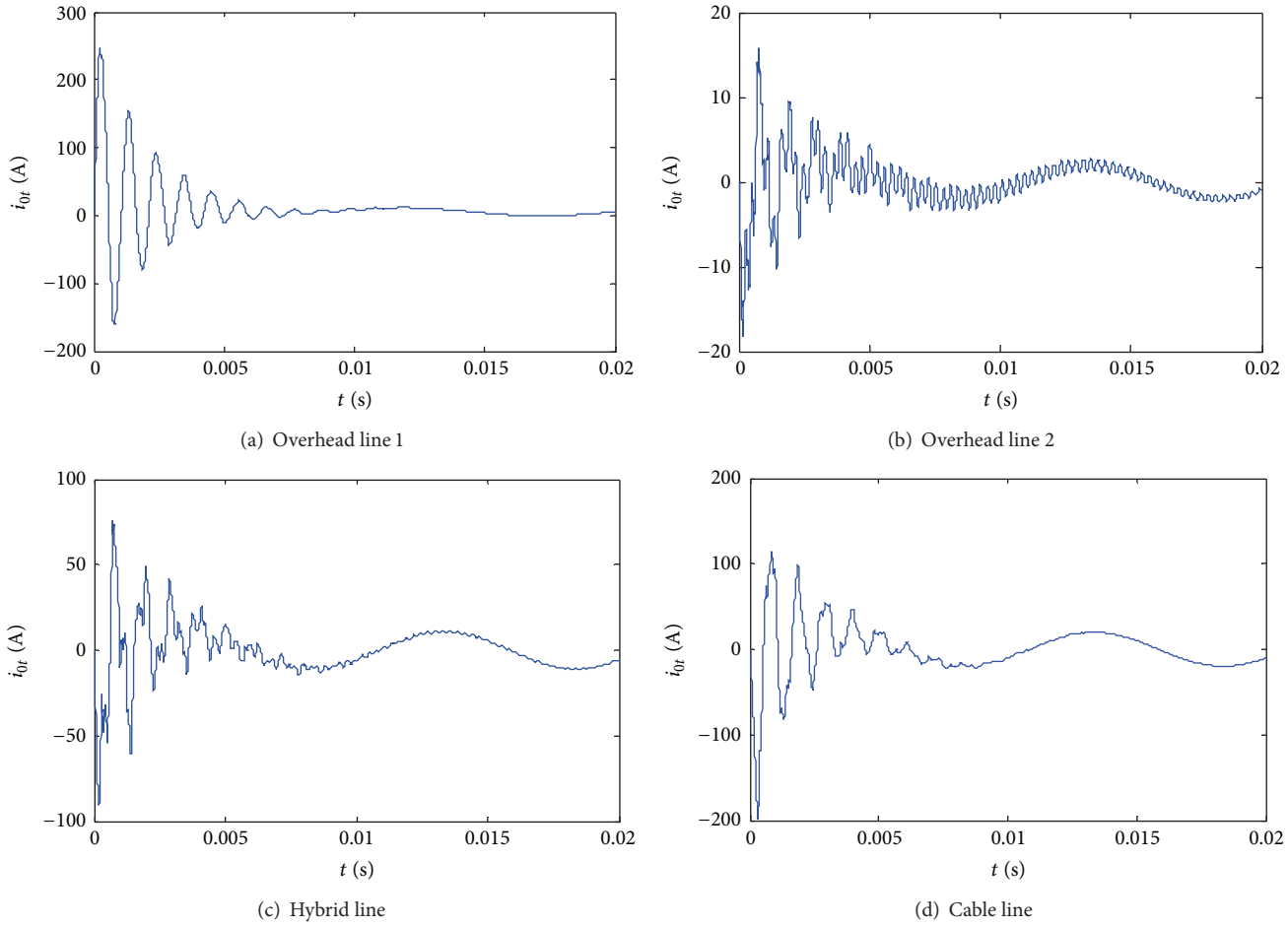

FIGURE 2: Transient zero sequence current.

3. Time-Frequency Atom Decomposition Theory

3.1. Decomposition Methods. For continuous signal $f(t) \in H$, H is Hilbert space and transformed $f(t)$ into $f(n)$; its process is discretization [13–15]. Defined atom dictionary $D = (g_r)_{r\in\Gamma}$, Γ is group of parameters r, $\|g_r\| = 1$. Choose the atoms to match the signal $f(n)$ from atom dictionary D, that is, the maximum inner product between $f(n)$ and all atoms. $g_{(r_0)}(n)$ meet the following formula:

$$\left|\left\langle f(n), g_{(r_0)}(n)\right\rangle\right| = \sup_{\gamma\in\Gamma}\left|\left\langle f(n), g_r\right\rangle\right|. \tag{4}$$

The signal could be decomposed by the best matching atom $g_{(r_0)}(n)$ component and the residual signal $Rf(n)$, and the calculation expression is shown in the following formula:

$$f(n) = \left\langle f(n), g_{(r_0)}(n)\right\rangle g_{(r_0)}(n) + Rf(n). \tag{5}$$

In (5), $Rf(n)$ approached along $g_{(r_0)}(n)$ direction. Obviously, $g_{(r_0)}(n)$ and $Rf(n)$ were orthogonal; therefore, the following formula was got:

$$\|f(n)\|^2 = \left|\left\langle f(n), g_{(r_0)}(n)\right\rangle\right|^2 + \|Rf(n)\|^2. \tag{6}$$

Because atom dictionaries are over completeness, the optimal solution could be turned to suboptimal solution; that is, choose the approximation atom to a certain extent. The calculation is shown in

$$\left|\left\langle f(n), g_{(r_0)}(n)\right\rangle\right| = \alpha \sup_{\gamma\in\Gamma}\left|\left\langle f(n), g_r\right\rangle\right|. \tag{7}$$

In formula (7), $0 \le \alpha \le 1$, decompose $Rf(n)$ and chose the best matching atom $g_{(r_1)}(n)$ from atom dictionary, make $R^0 f(n) = f(n)$ iterative k times; the k time residual component $R^k f(n)$ could be expressed as

$$R^k f(n) = \left\langle R^k f(n), g_{(r_k)}(n)\right\rangle g_{(r_k)}(n) + R^{k+1} f(n). \tag{8}$$

The signal $f(n)$ decomposed m times, and its expression is shown in

$$f(n) = \sum_{k=0}^{m-1}\left\langle R^k f(n), g_{(r_k)}(n)\right\rangle g_{(r_k)}(n) + R^m f(n). \tag{9}$$

Therefore, signal energy $\|f(n)\|^2$ could be expressed in

$$\|f(n)\|^2 = \sum_{k=0}^{m-1}\left|\left\langle R^k f(n), g_{(r_k)}(n)\right\rangle g_{(r_k)}(n)\right|^2 + \|R^m f(n)\|^2. \tag{10}$$

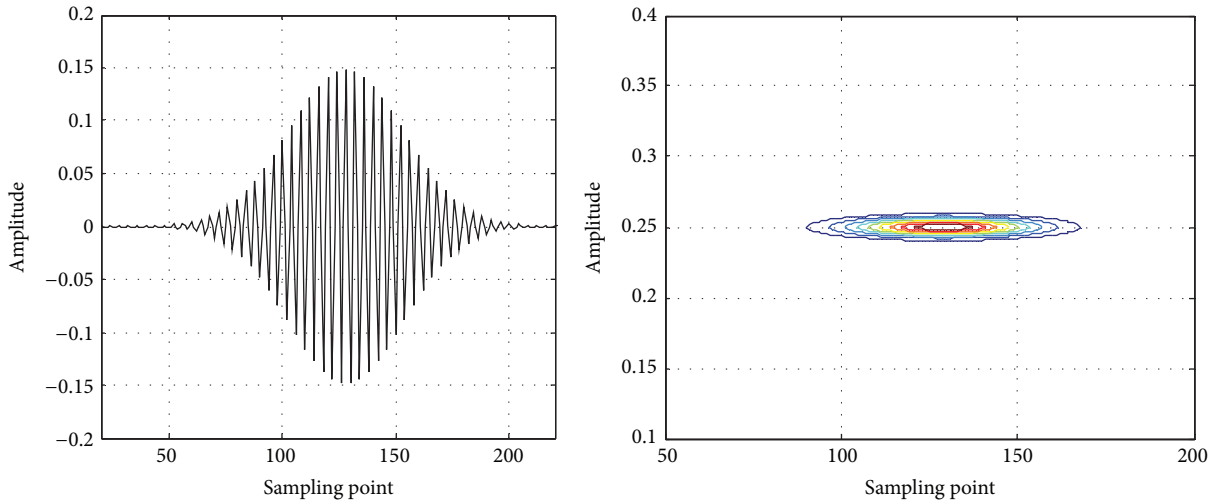

(a) Time-frequency diagram (b) Wigner-Ville distribution

Figure 3: Gabor atoms time-frequency diagram and Wigner-Ville distribution. $s = 2^6$, $u = 128$, $\xi = \pi/2$.

In (10), $g_{(r_k)}(n)$ meet the formula

$$\left|\left\langle R^k f(n), g_{(r_k)}(n)\right\rangle\right| = \alpha \sup_{\gamma\in\Gamma}\left|\left\langle R^k f(n), g_r\right\rangle\right|. \quad (11)$$

If it decomposed m times to meet the accuracy, then stop the decomposition. Because the residual component $R^m f(n)$ tends to 0, $f(n)$ could be expressed by chosen atoms. It was shown in

$$f(n) = \sum_{k=0}^{m-1}\left\langle R^k f(n), g_{(r_k)}(n)\right\rangle g_{(r_k)}(n). \quad (12)$$

The similarity degree C_m between original signal $f(n)$ and constructed signal $f_m(n)$ is shown in

$$C_m = \frac{\langle f(n), f_m(n)\rangle}{\|f(n)\| \cdot \|f_m(n)\|}. \quad (13)$$

Because $\|g_r\| = 1$, calculated Wigner-Ville distribution of formula (12), it could get

$$\begin{aligned} Wf(n,l) &= \sum_{k=0}^{M-1}\left|\left\langle R^k f(n), g_{r_k}(n)\right\rangle\right|^2 Wg_{r_k}(n,l) \\ &+ \sum_{k=0}^{M-1}\sum_{m=0,m\neq k}^{M-1}\left\langle R^k f(n), g_{r_k}(n)\right\rangle \overline{\left\langle R^m f(n), g_{r_m}(n)\right\rangle} \\ &\cdot W\left[g_{r_k}(n), g_{r_m}(n)\right](n,l). \end{aligned} \quad (14)$$

In (14), $Wg_{r_k}(n,l)$ is Wigner-Ville distribution of atom $g_{r_k}(n)$ and l is discretization frequency variable. The last item in (14) is cross terms of every atom. Mallat eliminated the cross terms and got the energy distribution in

$$Ef(n,l) = \sum_{k=0}^{M-1}\left|\left\langle R^k f(n), g_{(r_k)}(n)\right\rangle\right|^2 Wg_{(r_k)}(n,l). \quad (15)$$

In (15), $|\langle R^k f(n), g_{(r_k)}(n)\rangle|^2$ is energy intensity and $Ef(n,l)$ is density function of $f(n)$ energy distribution.

3.2. Gabor Atoms. Gabor atoms are constructed by Gauss energy function with telescopic, translation, and modulation transform, and its expression is shown in the following formula:

$$g_r(t) = \frac{1}{\sqrt{s}} g\left(\frac{t-u}{s}\right) e^{j\xi t}. \quad (16)$$

The expression of corresponding real Gabor atom is shown in the following formula:

$$g_{(r,\phi)}(t) = \frac{1}{\sqrt{s}} g\left(\frac{t-u}{s}\right)\cos(\xi t + \phi). \quad (17)$$

In (17), $g(t)$ is standard Gauss signal and is equal to $2^{1/4}e^{-\pi t^2}$, s is scale parameter, $1/\sqrt{s}$ is atom normalization parameter, and u, ξ, and ϕ are parameters of time shift, frequency modulation, and phase.

Parameter r is equal to (s, u, ξ), and its discretization treatment is $r = (a^j, pa^j\Delta u, ka^{-j}\Delta\xi)$, where $0 < j \le \log_2 N$, $0 \le p \le N2^{-j+1}$, $0 \le k \le 2^{j+1}$, and N is sampling points, where $a = 2$, $\Delta u = 0.5$, and $\Delta\xi = \pi$. ϕ is discrete as $\phi = v\cdot\pi/6$, where $0 \le v \le 12$, v is integer.

Single atom time-frequency diagram and Wigner-Ville distribution of Gabor atom are shown in Figure 3.

It can be known that Gabor atom has the best time-frequency aggregation in Figure 3 and utilized sparse signal representation to fully reveal signal time-frequency characteristics. The deficiency of Gabor atom is that atom frequency

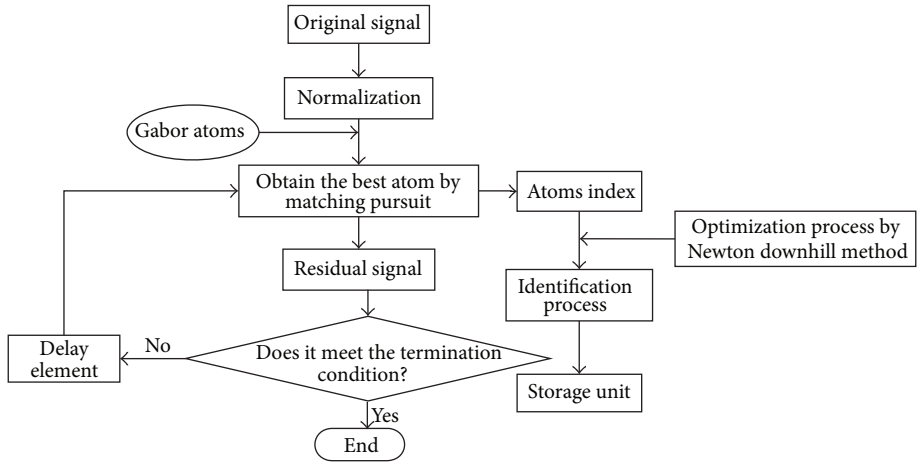

Figure 4: Atomic sparse decomposition process.

is not changed with time, and the division way of time-frequency plane belongs to lattice segmentation. Compare Figures 2 and 3; it is known that the similarity degree between Gabor atom waveforms and zero sequence currents is higher and, therefore, adopts matching pursuit way to match; it could not only accurately extract the fault feature components but also save a large number of calculation time. Hence, it used Gabor atoms to extract the fault features in the paper.

4. ELM Work Principle

Extreme learning machine is a novel feed-forward neural network [16–18], which is assumed to have N training sample $\{(\mathbf{x}_k, t_k)\}_{k=1}^{N}$; its expression is shown in (16):

$$o_k = \boldsymbol{\omega}^T f\left(\mathbf{W}_{\text{in}}\mathbf{x}_{\mathbf{k}} + \mathbf{b}\right), \quad k = 1, 2, \ldots, N. \tag{18}$$

In (18), $\mathbf{x}_{\mathbf{k}}$, $\mathbf{b}$, and o_k are input vector, hidden layer bias, and network output, respectively, $\mathbf{W}_{\text{in}}$ is input weight linked input node and hidden layer node, $\boldsymbol{\omega}$ is output weight linked hidden layer node and output node, f is hidden layer activation function and its form is Sigmoid function generally, and N is sample number.

At the beginning of training, $\mathbf{W}_{\text{in}}$ and $\mathbf{b}$ randomly generated and remain unchanged; it only needs to train output weight $\boldsymbol{\omega}$. Assume that feed-forward neural network approached training sample with zero error; that is, $\sum_{k=1}^{N} \|o_k - t_k\| = 0$. Therefore, $\mathbf{W}_{\text{in}}$, $\mathbf{b}$, and $\boldsymbol{\omega}$ meet the formula

$$\boldsymbol{\omega}^T f\left(\mathbf{W}_{\text{in}}\mathbf{x}_{\mathbf{k}} + \mathbf{b}\right) = t_k, \quad k = 1, 2, \ldots, N. \tag{19}$$

Formula (19) is written to matrix form; that is, $\mathbf{H}\boldsymbol{\omega} = \mathbf{T}$, where

$$\mathbf{H} = \begin{bmatrix} f(\mathbf{W}_{\text{in}}\mathbf{x}_1 + \mathbf{b}_1) & \cdots & f(\mathbf{W}_{\text{in}}\mathbf{x}_1 + \mathbf{b}_m) \\ \vdots & \ddots & \vdots \\ f(\mathbf{W}_{\text{in}}\mathbf{x}_N + \mathbf{b}_1) & \cdots & f(\mathbf{W}_{\text{in}}\mathbf{x}_N + \mathbf{b}_m) \end{bmatrix}_{N\times m}. \tag{20}$$

In (20), $\mathbf{H}$ and m are output matrix and node number of hidden layer, respectively, and $\mathbf{T}$ is expected output vector and it could be expressed as $\mathbf{T} = [t_1, t_2, \ldots, t_N]^T$. If the activation function of hidden layer is infinitely differentiable and the number of hidden layer node met the relationship $m \le N$, it could approach training sample with small training error. $\boldsymbol{\omega}$ value is calculated by pseudoinverse algorithm generally [19].

The training process of single-hidden layer feed-forward neural network (SLFN) is equivalent to calculating least squares solution of linear system; it is shown in

$$\|\mathbf{H}\widehat{\boldsymbol{\omega}} - \mathbf{T}\| = \min_{\omega} \|\mathbf{H}\boldsymbol{\omega} - \mathbf{T}\|. \tag{21}$$

In (21), $\widehat{\boldsymbol{\omega}}$ is least squares solution of minimum norm of $\mathbf{H}\boldsymbol{\omega} = \mathbf{T}$. $\mathbf{H}^+$ is generalized inverse of hidden layer output matrix $\mathbf{H}$. For feed-forward neural network, smaller weights have stronger generalization ability. For all least squares solution of equation $\mathbf{H}\boldsymbol{\omega} = \mathbf{T}$, $\widehat{\boldsymbol{\omega}}$ has the smallest norm number; that is, $\|\widehat{\boldsymbol{\omega}}\| = \|\mathbf{H}^+\mathbf{T}\| \le \|\boldsymbol{\omega}\|$, where

$$\forall \boldsymbol{\omega} \in \left\{\boldsymbol{\omega} \mid \|\mathbf{H}\boldsymbol{\omega} - \mathbf{T}\| \le \|\mathbf{H}\mathbf{z} - \mathbf{T}\|, \ \forall \mathbf{z} \in R^{N\times m}\right\}. \tag{22}$$

From (22), not only can ELM achieve the minimum training error but it also has stronger generalization ability than the traditional gradient descent algorithm. There is only one $\mathbf{H}^+$ for the generalized inverse $\mathbf{H}^+$ of matrix $\mathbf{H}$, so the $\widehat{\boldsymbol{\omega}}$ value is unique.

5. Test Signal Analysis

Given the test signal, there are three frequency components which have different time scale intervals; the calculation is as follows:

$$s(t) = \begin{cases} 9e^{-t}\sin(150\pi t) & 0 \le t \le 0.2\ \text{s} \\ 3.8e^{-t}\sin(100\pi t) & \\ \quad +2.8e^{-0.5t}\sin(70\pi t) & 0.2\ \text{s} < t < 0.5\ \text{s}. \end{cases} \tag{23}$$

We added 20 db Gauss white noise to the signal and verified anti-interference ability of atom decomposition method. For original signal, it should be normalized the signal is divided by its Euclid norm [20]. The decomposition process was shown in Figure 4.

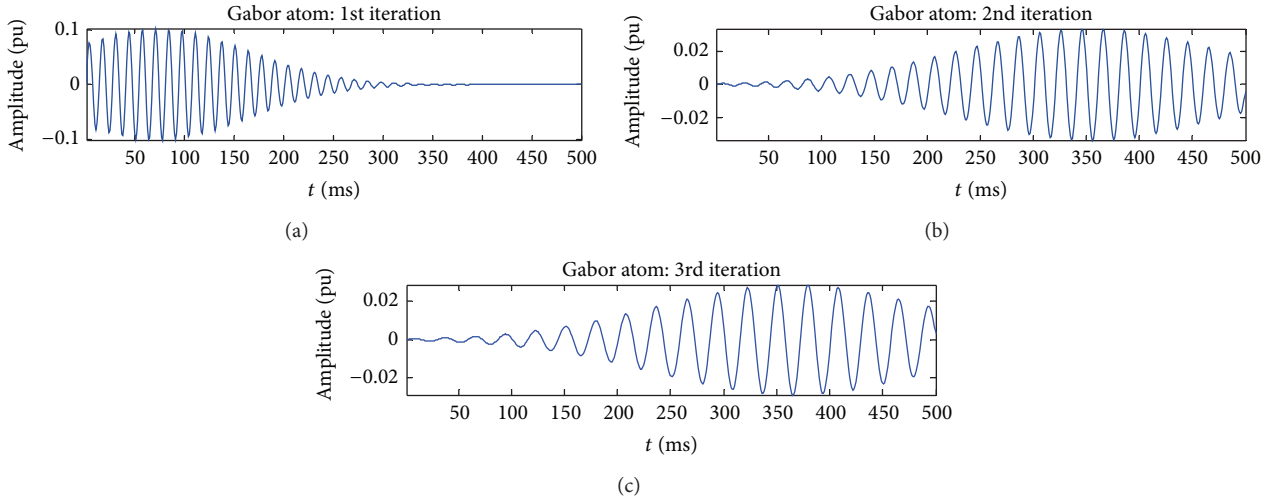

Figure 5: The first, second, and third atoms.

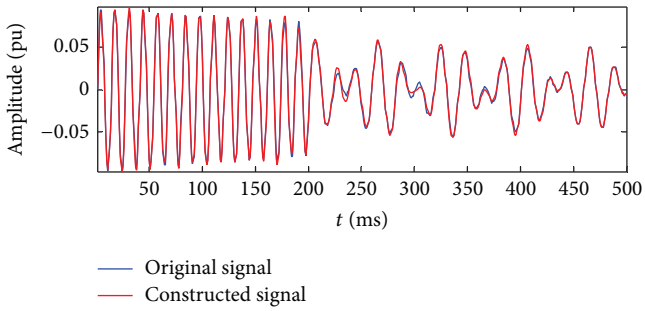

Figure 6: Comparison of original signal and constructed signal by 20 iterations.

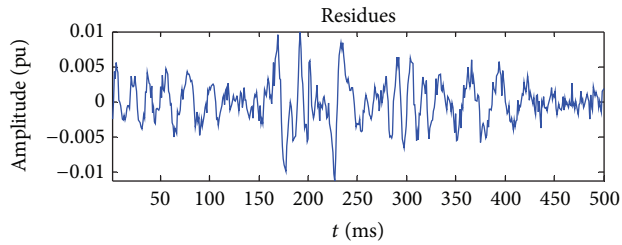

Figure 7: Residual component decomposed by 20 iterations.

Identification method: frequency center F is equaled to $f_s\xi/2\pi$, f_s is sampling frequency, start time is $T_s = u - s/2$, end time is $T_e = u+s/2$, ϕ is phase angle, and the amplitude is equaled to atom normalization amplitude to multiply actual energy value which is Euclid norm.

Set f_s = 1 kHz; simulation time and sampling points areequaled to 0.5 s and 500, respectively. Before the decomposition, the normalization equation is shown in

$$s_g(n) = \frac{s(n)}{\|s(n)\|}. \tag{24}$$

In (24), $s(n)$ is discrete signal of $s(t)$, $s_g(n)$ is normalization expression of $s(n)$, $\|s(n)\|$ is Euclid norm, and its value is 92.7915.

Set iteration number as 20, and decompose $s_g(n)$ by atomic algorithm. Figure 5 shows atom 1, atom 2, and atom 3 generated by iteration, respectively, and all atoms in Figure 5 are normalized results. Comparison of original signal and constructed signal is shown in Figure 6; it indicated that the difference of two signals is smaller by 20 iteration numbers. The residual component amplitude is only 10^{-3} in Figure 7 and further shows that the accuracy is satisfied atomic decomposition requirement.

The parameters of atom 1, atom 2, and atom 3 are shown in Table 1. Notably, every atom decomposed by atomic algorithm does not have physical meaning; it just indicated distribution characteristics of time scales. Hence, the atomic parameters in Table 1 are needed for identification processing and we transformed it to indicate local features of original signal; it is shown in Table 2.

We observed the amplitude, frequency, and phase value of atoms in Table 2; it could know that the atoms 1, 2, and 3 represent $9e^{-t}\sin(150\pi t)$, $3.8e^{-t}\sin(100\pi t)$, and $2.8e^{-0.5t}\sin(70\pi t)$ of original signal, respectively, by identification processing. For atom 1, because the actual end time is 200 ms and the calculated end time is 187.7268 ms, deviation is 12.2732 ms. But, for atoms 2 and 3, comparing the calculated start time with actual start time, the deviations are 1.4297 ms and 7.8642 ms, respectively; the difference is smaller.

Time-frequency analysis by 20 iteration number decomposition is shown in Figure 8; we can see that the atoms could indicate local characteristics of nonstationary test signals accurately, including frequency segment, time interval, and frequency components energy; compared to the traditional FFT spectrum, cross interference and noise interference can be suppressed effectively, and the calculation accuracy is also higher than FFT.

Table 1: Characteristic parameters of every atom.

Atoms	Scale s/pu	Location shift u/pu	Frequency shift w/Hz	Phase/rad	Atom amplitude
1	227.6520	72.9008	0.4709	−2.0125	0.0903
2	308.3047	352.7226	0.3150	−2.2285	0.0380
3	316.8729	366.3006	0.2200	−1.8173	0.0281

Table 2: Local characteristic parameters of test signal.

Atoms	Amplitude	Frequency/Hz	Phase/rad	Start time/ms	End time/ms
1	9.0112	74.9841	−2.0125	—	186.7268
2	3.7921	50.1592	−2.2285	198.5703	—
3	2.8041	35.0319	−1.8173	207.8642	—

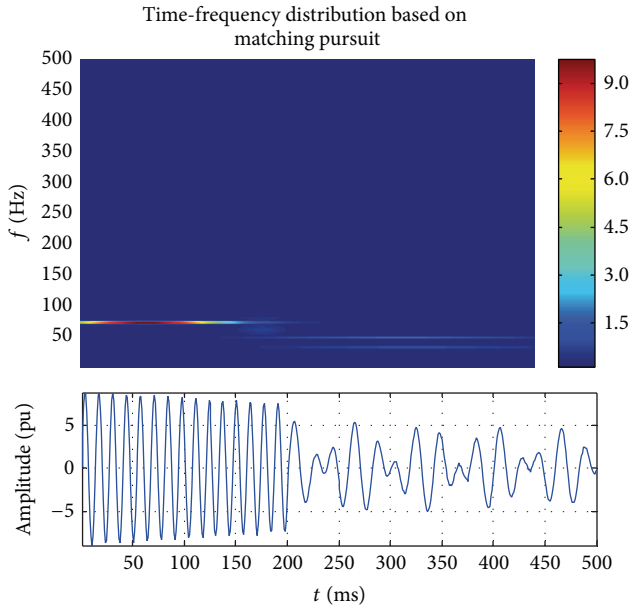

Figure 8: Time-frequency representation of test signal.

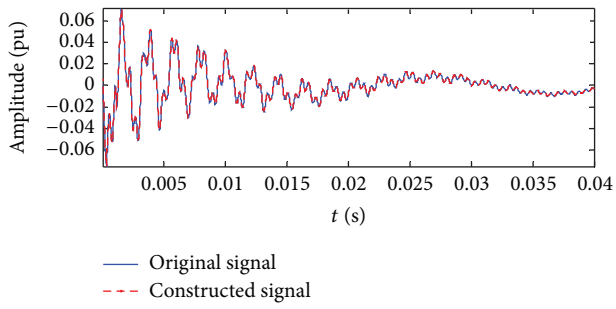

Figure 9: Fitting waveform of overhead line S_2.

6. Choose Characteristic Atom of Zero Sequence Current

To verify ASD algorithm extracting fault feature components ability in distribution network, it gives the feeder fault as example; by ASD, set the iteration number as 4; hence, the zero sequence current fitting waveform of overhead line is shown in Figure 9.

The similarity between constructed signal and original overhead line S_2 signal is higher by 4 iterations, and the fitting accuracy meets the requirements. The first four atoms' waveform and specific parameters are shown in Figure 10 and Tables 3 and 4, respectively.

Combined with Figure 10 and Table 4, atom 1 waveform shows oscillation attenuation trend; both waveform and energy value have higher similarity with original signal, and it indicated major information of original signal; therefore, atom 1 is defined as main components atom, and its frequency value is equal to 472.9299 Hz. Atom 2 is defined as fundamental atom, and its frequency value is 50.9554 Hz. Atom 3 and atom 4 all show oscillation attenuation trend, but their frequency values are different from atom 1: they are equal to 1778.6624 Hz and 1176.7516 Hz, respectively, and all the high frequency components; therefore, it is defined as transient characteristic atoms 1 and 2, respectively.

Zero sequence current fitting waveform of cable line S_4 is shown in Figure 11, the first four atoms are shown in Figure 12, and the parameters of every atom are shown in Tables 5 and 6. Combining Figure 12 and Table 6, it is known that atom 1 of cable line is main components atom, and its frequency is equal to 472.9299 Hz. Therefore, the frequencies of fundamental atom and transient characteristic atoms 1 and 2 are equal to 49.3631 Hz, 1175.1592 Hz, and 2366.2420 Hz, respectively. Comparing Figures 10 and 12, it got different characteristic of transient characteristic atoms between overhead line and cable line.

Comparing Figures 10(c), 10(d) and Figures 12(c), 12(d) respectively, for cable line, oscillation attenuation trend of transient characteristic atoms is more obvious; its oscillation process is shorter than overhead line. Because the capacitance to ground value of cable line is larger than overhead line in actual distribution network, it got different oscillation process of fault current.

7. Fault Line Selection Methods

7.1. Atom Dictionary Measure Based on Information Entropy Index. Information entropy can measure uncertain degree of event; the information entropy value is larger; it indicated that

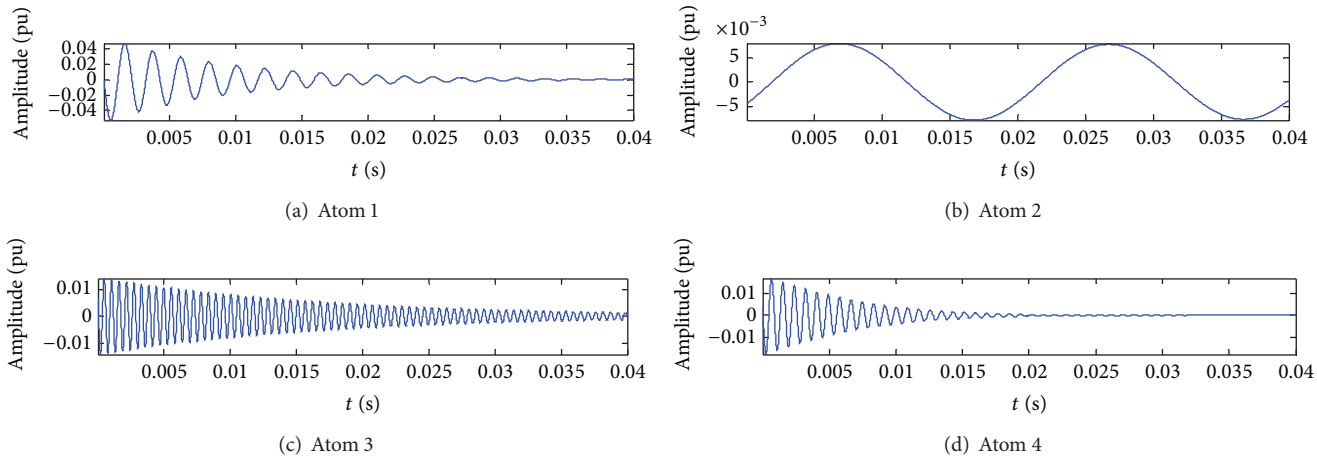

Figure 10: Zero sequence current characteristic atom of overhead line S_2.

Table 3: Every atom characteristic parameters of overhead line S_2.

Atoms	Scale s/pu	Location shift u/pu	Frequency shift w/Hz	Phase/rad	Atom amplitude
1	3.941×10^4	-2.7094×10^5	0.0297	1.5419	0.0385
2	1.15×10^6	-2.6135×10^6	0.0032	−2.1710	0.0048
3	4.1957×10^4	-1.6524×10^5	0.1117	0.9501	0.0122
4	2.97×10^3	-1.7133×10^3	0.0739	1.2609	0.0135

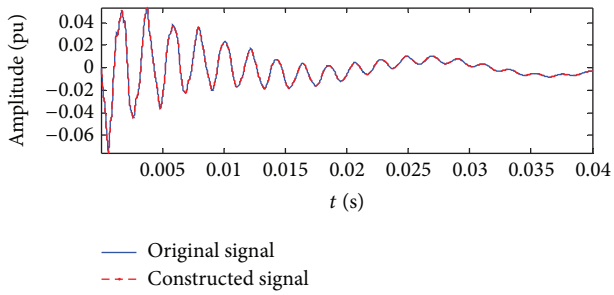

Figure 11: Fitting waveform of cable line S_4.

uncertain degree is larger; that is, random characteristics of event are stronger; therefore, the credibility applied to fault diagnosis is lower [21, 22]. According to the characteristics of single phase to ground fault, one fault feature is more reliable, the fault difference of fault line and healthy line is larger, and its information entropy value is smaller; it indicated that certain characteristics of FLS result based on the fault characteristics are larger. Therefore, it used information entropy to measure uncertain characteristics of every feature. To evaluate certain degree of sample library by atoms, it adopted information entropy theory to calculate in the paper; the details are as follows.

Firstly, calculate the ratio of atom library and atom library sum; it is shown in

$$\lambda(k) = \frac{L(k)}{\sum_{k=0}^{N} L(k)}. \tag{25}$$

In (25), $L(k)$ is atom library; it can be main component atom library, fundamental atom library, and transient characteristic atom library. $\lambda(k)$ is probability reflected every line fault, and the calculation formula of information entropy is shown in

$$H = -\sum_{k=0}^{N} \lambda(k) \ln \lambda(k). \tag{26}$$

In (26), information entropy reflected characteristics information content of samples, and the value is larger, it indicated that sample in the atom library has more uncertainty; hence, the fault characteristic component is less, and the credibility is lower. On the contrary, the credibility of atom library is higher.

Figures 13(a), 13(b), 13(c), and 13(d) are information entropy value of main components atom, fundamental atom, transient characteristic atoms 1 and 2; it can be seen from Figure 13 that information entropy values of most atoms are smaller and reflected certainty of the sample is stronger, and it applied to FLS which has more credibility; however, the entropy values of some samples are larger; it reflected that certainty of the samples is weak, and the credibility is lower. To evaluate credibility of every atom, the statistical method is adopted to measure the information entropy; the details are as follows.

Step 1. We selected the maximum entropy value of atom libraries 1, 2, 3, and 4, expressed as $H_{1\max}$, $H_{2\max}$, $H_{3\max}$, and $H_{4\max}$, compared the four values, and determined the maximum entropy value $H_{\max}$.

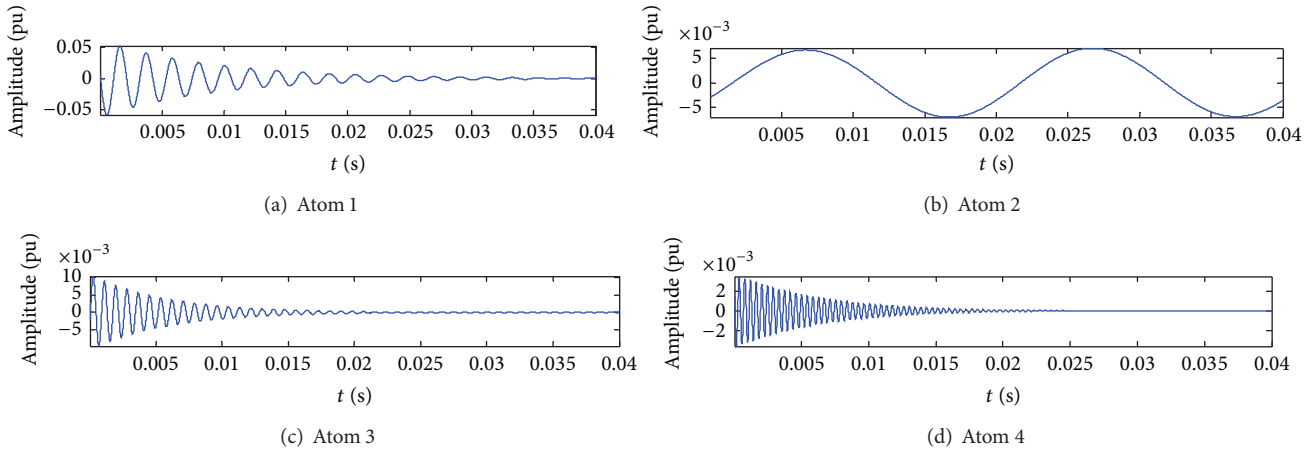

Figure 12: Zero sequence current characteristic atom of cable line S_4.

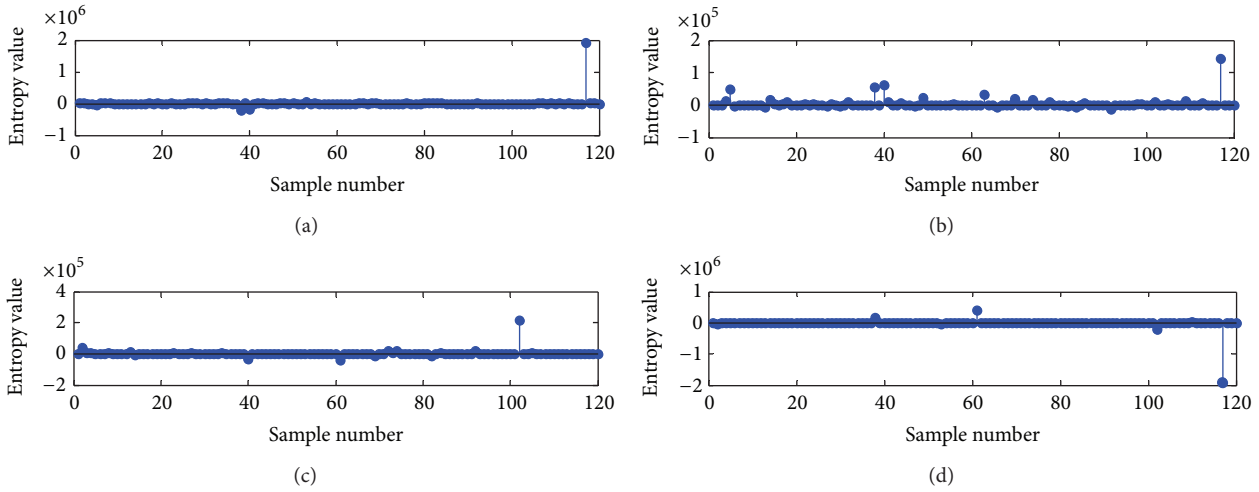

Figure 13: Information entropy value of every atom library.

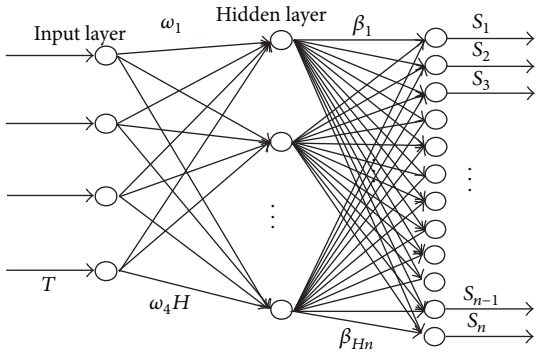

Figure 14: ELM network topology structure.

Step 2. We calculated $H/H_{\max}$ and then counted sample number of every atom library which is less than μ (in the paper $\mu = 0.01$).

Step 3. We took sample number by Step 2 to divide total number of samples and got information entropy measure of atom library.

The information entropy measure value can evaluate data credibility of every atom library with FLS, the measure value is smaller, and it indicated that the sample uncertainty is smaller and the certainty is larger; therefore, the credibility with FLS is higher. On the contrary, the value is larger, indicated certainty is smaller, and the credibility is lower.

7.2. Confidence Degree of Fault Line Selection. Judgment results did not add additional constraints in the past FLS method; it only required to show the fault line symbol, and the symbol output results have the following disadvantages.

(1) It can not reflect significant degree of fault feature. When the fault occurred, if fault feature is obvious, the FLS is very reliable; on the contrary, the fault feature is weak, and the results may be wrong, but the difference is hard to reflect in symbol FLS method.

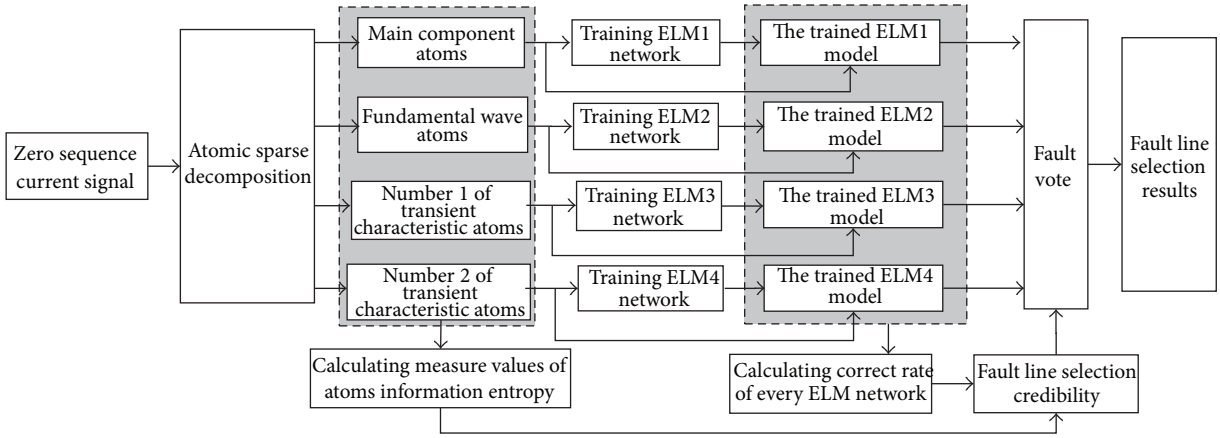

Figure 15: Basic framework of fault voting.

Table 4: Zero sequence current local characteristic parameters of overhead line S_2.

Atoms	Amplitude	Frequency shift/Hz	Phase/rad	Start time/ms	End time/ms
1	3.8654	472.9299	1.5419	10.2568	—
2	0.0485	50.9554	−2.1710	15.5897	—
3	1.2352	1778.6624	0.9501	8.5679	—
4	1.3446	1176.7516	1.2609	9.5879	22.5625

(2) It can not provide fault indication information of other lines.

(3) It is not conducive to use multiple criteria comprehensively. When using multiple criteria to select fault line, it is not viable to vote results of several criteria simply [23–25].

This paper proposed a novel FLS method based on atom library fusion ideas; its purpose is not to give FLS results by every criterion simply; it quantitatively measured fault symptom degree of every line by every atom characteristic and then trained the ELM to make decision. Finally, it adopted vote to get the results.

It has given concept of FLS confidence degree in the paper; the confidence degree is defined as real variables that is used to measure atom samples certainty and ELM training accuracy; its scope is $[0, \infty)$. The confidence degree value of atom library is larger; it indicated that vote weight of the atom library is larger. The calculation is shown in

$$\begin{aligned}\text{Confidence degree} &= \text{information entropy measure of atom library} \\ &\times \text{ELM network accuracy.}\end{aligned} \quad (27)$$

7.3. Fault Line Selection Model of ELM. Based on the acquired main component atom, fundamental atom, and transient characteristic atom of group W, the ELM network is trained. There are three steps for the initial judgment of FLS in ELM network.

Step 1. Normalize the input/output training samples of group W, which is limited to $[0, 1]$, and randomly offer the input weights and hidden layer threshold of the input neurons and the τ hidden layer neurons $\omega_\tau = [\omega_{1\tau}, \omega_{2\tau}, \omega_{3\tau}, \omega_{4\tau}]^T$ $(\tau \in H)$.

Step 2. According to the generalized inverse matrix theory of Penrose Moore, the output weights of the network with the least square solution are calculated in an analytical way $\beta_\tau = [\omega_{\tau 1}, \ldots, \beta_{\tau 12}]^T$ and well-trained ELM network is obtained, from which the nonlinear mapping relations between every sample atom and fault conditions in the line can be shown.

Step 3. Given a set of fault atomic sample input data, the initial selection of fault line is presented based on the well-trained ELM network. The accuracy rate of test set is adopted to test the result of the initial selection [26, 27].

Based on the above analysis, the ELM network topology established in this paper is shown in Figure 14.

7.4. Fault Vote Mechanism. According to the theory of information entropy measure and FLS confidence degree, the paper proposed the basic framework as shown in Figure 15.

From Figure 15, the four atoms correspondingly composed atom library as fault training samples and input it to corresponding ELM network to train, and then, according to ELM network output and FLS confidence degree to achieve the fault vote, finally it judged the FLS results [28, 29]. Based on the vote principle of society, it proposed fault vote selection way based on confidence degree; the specific steps are as follows.

Step 1. Firstly, set that every line is healthy line; in other words, assume that there is no fault.

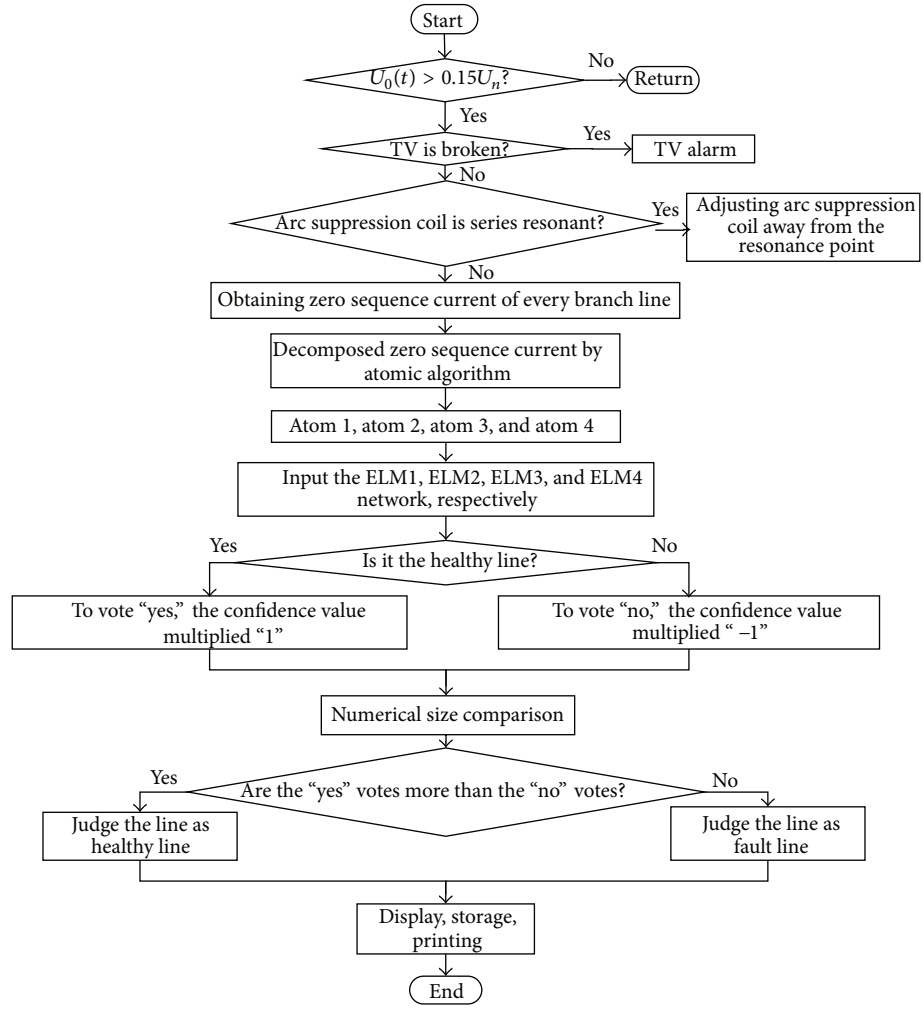

Figure 16: Fault line selection process.

Table 5: Every atom characteristic parameters of cable line S_4.

Atoms	Scale s/pu	Location shift u/pu	Frequency shift w/Hz	Phase/rad	Atom amplitude
1	3.6216×10^4	-2.2767×10^5	0.0297	1.4440	0.0513
2	1.3019×10^4	2.4196×10^3	0.0031	−2.0734	0.0065
3	2.3151×10^4	-1.5341×10^5	0.0738	−1.8505	0.0123
4	4.6146×10^3	-4.8524×10^3	0.1486	0.9955	0.0043

Step 2. When a line is judged as healthy line by ELM network output, the confidence degree value is multiplied "1," which is consistent with Step 1 assumption, hence voted "agree." On the other hand, when a line is judged as fault line by ELM network output, the confidence degree value is multiplied "–1," which is deviated from Step 1 assumption, hence voted "against."

Step 3. When ELM network judgment is completed, compare the vote number value of "agree" and "against" and then, when "agree" value is larger than "against," judge the line as healthy line; on the contrary, the line is judged as fault line.

The specific process of FLS is shown in Figure 16.

8. Example Analysis

In this paper, the ATP-EMTP is used to simulate a single phase to ground fault, and the simulation model is shown in Figure 17. The parameters of simulation model are as follows [30].

In order to simplify the analysis, the power supply adopts ideal source; therefore, the internal impedance of the source is 0.

Overhead line positive-sequence parameters are R_1 = 0.17 Ω/km, L_1 = 1.2 mH/km, and C_1 = 9.697 nF/km; zero sequence parameters are R_0 = 0.23 Ω/km, L_0 = 5.48 mH/km, and C_0 = 6 nF/km.

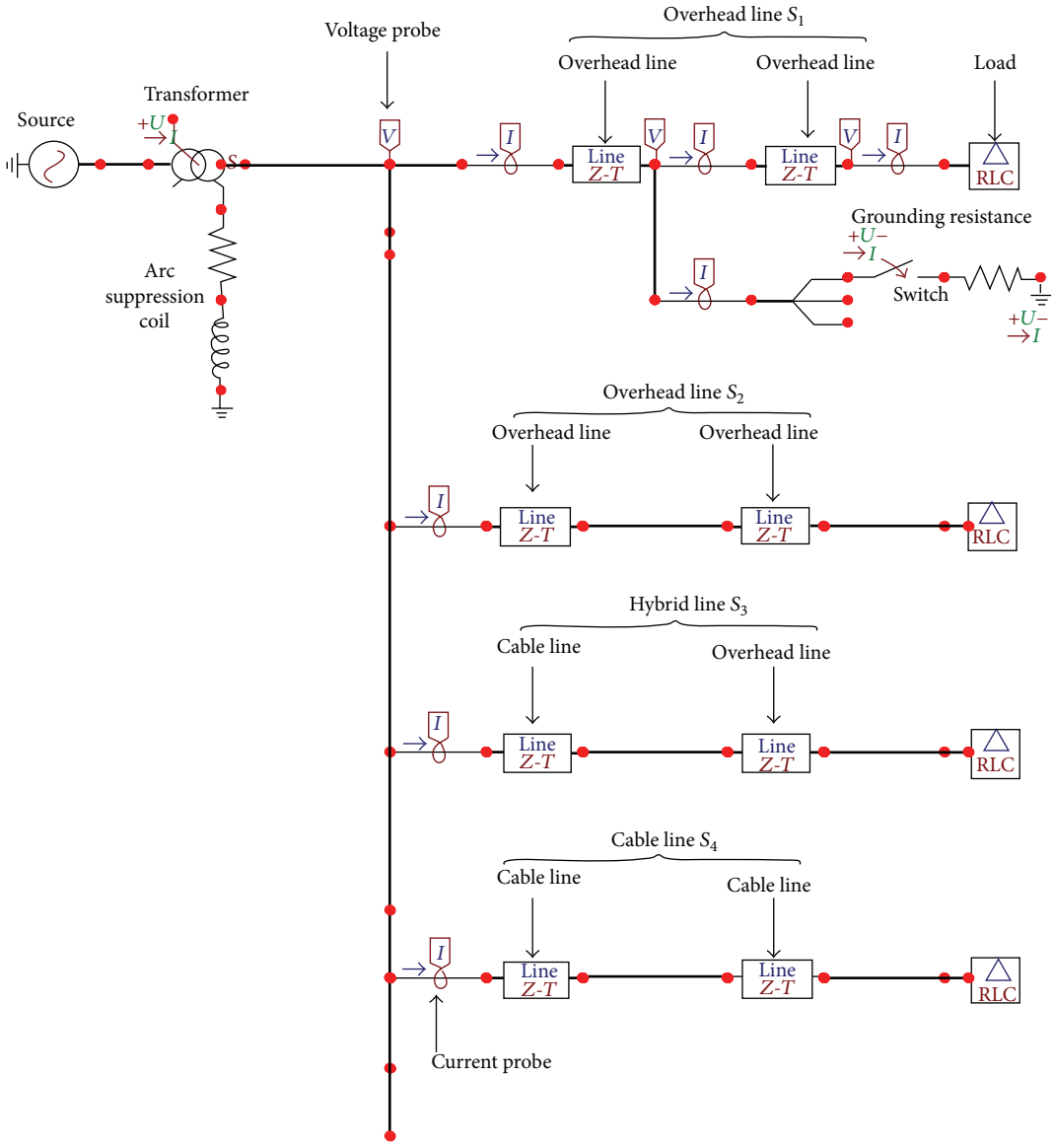

Figure 17: ATP simulation model.

Cable line positive-sequence parameters are R_{11} = 0.193 Ω/km, L_{11} = 0.442 mH/km, and C_{11} = 143 nF/km; zero sequence parameters are R_{00} = 1.93 Ω/km, L_{00} = 5.48 mH/km, and C_{00} = 143 nF/km.

The overhead lines S_1 and S_2 are 13.5 km and 24 km, respectively. Cable line S_4 is 10 km. Hybrid line S_3 is 17 km, where the cable line is 5 km and the overhead line is 12 km.

Transformer is 110/10.5 kV, connection mode indicates that the primary side is triangle connection, and the second side is star connection. Primary resistance is 0.40 Ω, inductance is 12.2 Ω, secondary resistance is 0.006 Ω, inductance is 0.183 Ω, excitation current is 0.672 A, magnetizing flux is 202.2 Wb, magnetic resistance is 400 kΩ. Load: all are delta, Z_L = 400 + j20 Ω. Petersen coil: L_N = 1281.9 mH, R_N = 40.2517 Ω.

Sampling frequency f_s is equal to 10^5 Hz, simulation time is 0.06 s, and the single phase to ground fault occurred at 0.02 s. Based on the simulation model, when the initial phase angle is 0°, the transition resistance is 1 Ω, 10 Ω, 100 Ω, 1000 Ω, or 2000 Ω, respectively; the single phase to ground fault tests are carried out at the points of 5 km and 10 km in line S_1, 9 km and 17 km in line S_3, and 6 km and 10 km in line S_4 with the arc suppression coil to ground (overcompensation is 10%). The zero sequence current signals of four feeder lines, which are chosen from 2 circles after the fault, can be collected for each fault, and the total number is 4 × 5 × 2 × 3 = 120. After the atomic decomposition of these 120 zero sequence current signals, the first 4 atoms of each group are picked out, respectively, to comprise a main component atomic library, a fundamental atomic library, and two transient atomic libraries. Each library contains 120 atomic samples, the first 100 samples of which are taken as the training set and the last 20 samples of which as the test set [31].

According to the ELM theory, when the number of hidden layer neurons equals the number of the training set samples, then, for any W_{in} and b, ELM can approximate to the

Table 6: Zero sequence current local characteristic parameters of cable line S_4.

Atoms	Amplitude	Frequency/Hz	Phase/rad	Start time/ms	End time/ms
1	33.6181	472.9299	1.4440	11.5875	—
2	4.2596	49.3631	−2.0734	14.8956	—
3	8.0605	1175.1592	−1.8505	8.6987	21.5614
4	2.8179	2366.2420	0.9955	9.4893	28.4462

Table 7: Fault voting result of overhead line S_1 under 0°.

Fault location/km	Transition resistance/Ω	Feeder line style	Atom 1	Atom 2	Atom 3	Atom 4	Voting results	Fault line selection results
10	100	**Overhead line S_1**	**0.9667 × (−1)**	**0.855 × (−1)**	**0.8358 × (−1)**	**0.7866 × (−1)**	**3.4441 > 0**	**Vote S_1 is fault line**
		Overhead line S_2	0.9667 × 1	0.855 × 1	0.8358 × (−1)	0.7866 × (−1)	1.8217 > 1.6224	Vote S_2 is healthy line
		Hybrid line S_3	0.9667 × 1	0.855 × 1	0.8358 × 1	0.7866 × 1	3.4441 > 0	Vote S_3 is healthy line
		Cable line S_4	0.9667 × 1	0.855 × 1	0.8358 × 1	0.7866 × (−1)	2.6575 > 0.7866	Vote S_4 is healthy line
5	1000	**Overhead line S_1**	**0.9667 × (−1)**	**0.855 × (−1)**	**0.8358 × (−1)**	**0.7866 × (−1)**	**3.4441 > 0**	**Vote S_1 is fault line**
		Overhead line S_2	0.9667 × 1	0.855 × 1	0.8358 × 1	0.7866 × 1	3.4441 > 0	Vote S_2 is healthy line
		Hybrid line S_3	0.9667 × 1	0.855 × (−1)	0.8358 × 1	0.7866 × 1	2.5891 > 0.855	Vote S_3 is healthy line
		Cable line S_4	0.9667 × 1	0.855 × 1	0.8358 × 1	0.7866 × (−1)	2.6575 > 0.7866	Vote S_4 is healthy line
10	1000	**Overhead line S_1**	**0.9667 × (−1)**	**0.855 × (−1)**	**0.8358 × (−1)**	**0.7866 × (−1)**	**3.4441 > 0**	**Vote S_1 is fault line**
		Overhead line S_2	0.9667 × 1	0.855 × 1	0.8358 × 1	0.7866 × 1	3.4441 > 0	Vote S_2 is healthy line
		Hybrid line S_3	0.9667 × 1	0.855 × 1	0.8358 × 1	0.7866 × 1	3.4441 > 0	Vote S_3 is healthy line
		Cable line S_4	0.9667 × 1	0.855 × 1	0.8358 × (−1)	0.7866 × 1	2.6083 > 0.8358	Vote S_4 is healthy line
5	2000	**Overhead line S_1**	**0.9667 × (−1)**	**0.855 × (−1)**	**0.8358 × (−1)**	**0.7866 × 1**	**2.6575 > 0.7866**	**Vote S_1 is fault line**
		Overhead line S_2	0.9667 × 1	0.855 × 1	0.8358 × 1	0.7866 × 1	3.4441 > 0	Vote S_2 is healthy line
		Hybrid line S_3	0.9667 × 1	0.855 × 1	0.8358 × 1	0.7866 × 1	3.4441 > 0	Vote S_3 is healthy line
		Cable line S_4	0.9667 × 1	0.855 × (−1)	0.8358 × 1	0.7866 × 1	2.5891 > 0.855	Vote S_4 is healthy line
10	2000	**Overhead line S_1**	**0.9667 × (−1)**	**0.855 × (−1)**	**0.8358 × (−1)**	**0.7866 × (−1)**	**3.4441 > 0**	**Vote S_1 is fault line**
		Overhead line S_2	0.9667 × 1	0.855 × 1	0.8358 × 1	0.7866 × 1	3.4441 > 0	Vote S_2 is healthy line
		Hybrid line S_3	0.9667 × 1	0.855 × 1	0.8358 × (−1)	0.7866 × 1	2.6083 > 0.8358	Vote S_3 is healthy line
		Cable line S_4	0.9667 × 1	0.855 × 1	0.8358 × 1	0.7866 × 1	3.4441 > 0	Vote S_4 is healthy line

Table 8: Fault voting result of hybrid line S_3 under 0°.

Fault location/km	Transition resistance/Ω	Feeder line style	Atom 1	Atom 2	Atom 3	Atom 4	Voting results	Fault line selection results
17	100	Overhead line S_1	0.9667 × 1	0.855 × 1	0.8358 × (−1)	0.7375 × 1	2.5592 > 0.8358	Vote S_1 is healthy line
		Overhead line S_2	0.9667 × 1	0.855 × 1	0.8358 × 1	0.7375 × (−1)	2.6575 > 0.7375	Vote S_2 is healthy line
		Hybrid line S_3	**0.9667 × (−1)**	**0.855 × 1**	**0.8358 × (−1)**	**0.7375 × (−1)**	**2.54 > 0.855**	**Vote S_3 is fault line**
		Cable line S_4	0.9667 × 1	0.855 × (−1)	0.8358 × 1	0.7375 × 1	2.54 > 0.855	Vote S_4 is healthy line
9	1000	Overhead line S_1	0.9667 × 1	0.855 × 1	0.8358 × 1	0.7375 × (−1)	2.6575 > 0.7375	Vote S_1 is healthy line
		Overhead line S_2	0.9667 × 1	0.855 × 1	0.8358 × 1	0.7375 × (−1)	2.6575 > 0.7375	Vote S_2 is healthy line
		Hybrid line S_3	**0.9667 × (−1)**	**0.855 × (−1)**	**0.8358 × (−1)**	**0.7375 × (−1)**	**3.395 > 0**	**Vote S_3 is fault line**
		Cable line S_4	0.9667 × 1	0.855 × 1	0.8358 × (−1)	0.7375 × 1	2.5592 > 0.8358	Vote S_4 is healthy line
17	1000	Overhead line S_1	0.9667 × 1	0.855 × 1	0.8358 × 1	0.7375 × (−1)	2.6575 > 0.7375	Vote S_1 is healthy line
		Overhead line S_2	0.9667 × 1	0.855 × 1	0.8358 × (−1)	0.7375 × 1	2.5592 > 0.8358	Vote S_2 is healthy line
		Hybrid line S_3	**0.9667 × (−1)**	**0.855 × (−1)**	**0.8358 × (−1)**	**0.7375 × (−1)**	**3.395 > 0**	**Vote S_3 is fault line**
		Cable line S_4	0.9667 × 1	0.855 × 1	0.8358 × 1	0.7375 × 1	3.395 > 0	Vote S_4 is healthy line
9	2000	Overhead line S_1	0.9667 × 1	0.855 × 1	0.8358 × 1	0.7375 × 1	3.395 > 0	Vote S_1 is healthy line
		Overhead line S_2	0.9667 × 1	0.855 × 1	0.8358 × 1	0.7375 × 1	3.395 > 0	Vote S_2 is healthy line
		Hybrid line S_3	**0.9667 × (−1)**	**0.855 × (−1)**	**0.8358 × (−1)**	**0.7375 × 1**	**2.6575 > 0.7375**	**Vote S_3 is fault line**
		Cable line S_4	0.9667 × 1	0.855 × 1	0.8358 × 1	0.7375 × 1	3.395 > 0	Vote S_4 is healthy line
17	2000	Overhead line S_1	0.9667 × 1	0.855 × 1	0.8358 × 1	0.7375 × 1	3.395 > 0	Vote S_1 is healthy line
		Overhead line S_2	0.9667 × 1	0.855 × 1	0.8358 × 1	0.7375 × 1	3.395 > 0	Vote S_2 is healthy line
		Hybrid line S_3	**0.9667 × (−1)**	**0.855 × (−1)**	**0.8358 × (−1)**	**0.7375 × (−1)**	**3.395 > 0**	**Vote S_3 is fault line**
		Cable line S_4	0.9667 × 1	0.855 × 1	0.8358 × 1	0.7375 × 1	3.395 > 0	Vote S_4 is healthy line

training samples with no deviation, and the calculation result is the best. Therefore, four ELM networks are used to train the fault atomic samples in four atomic libraries, respectively, of which the input layer neurons are 4000, the hidden layer neurons are 100, and the output layer neuron is 1.

According to the information entropy theory, the values of information entropy of main component atomic library, fundamental atomic library, and transient atomic libraries 1 and 2 are calculated as 0.9667, 0.95, 0.9833, and 0.9833 respectively. In addition, after the ELM networks train every atom library, the accuracy rate of the 4 test sets of ELM network is 100%, 90%, 85%, and 80%. Therefore, according to formula (27), the confidence degree of every atomic library is 0.9667, 0.855, 0.8358, and 0.7866. Table 7 shows the voting results of fault in overhead line S_1 when the initial phase angle is 0°. According to the fault voting mechanism, assuming that all the branch lines are healthy lines, if the line checked by the ELM network is a healthy line, then multiply the line selection credibility by "1" which shows "agree"; if the line checked is a fault line, then multiply the line selection credibility by "−1," which shows "against." Finally, FLS is achieved through the comparison between the votes of "agree" and of "against." As can be seen from Table 7, at different fault distance and different grounding resistance value, the fault in overhead line

Table 9: Fault voting result of cable line S_4 under 0°.

Fault location/km	Transition resistance/Ω	Feeder line style	Atom 1	Atom 2	Atom 3	Atom 4	Voting results	Fault line selection results
10	100	Overhead line S_1	0.9667 × 1	0.7125 × 1	0.9341 × (−1)	0.7375 × 1	2.4167 > 0.9341	Vote S_1 is healthy line
		Overhead line S_2	0.9667 × 1	0.7125 × 1	0.9341 × 1	0.7375 × 1	3.3508 > 0	Vote S_2 is healthy line
		Hybrid line S_3	0.9667 × 1	0.7125 × 1	0.9341 × 1	0.7375 × 1	3.3508 > 0	Vote S_3 is healthy line
		Cable line S_4	**0.9667 × (−1)**	**0.7125 × (−1)**	**0.9341 × (−1)**	**0.7375 × (−1)**	**3.3508 > 0**	**Vote S_4 is fault line**
6	1000	Overhead line S_1	0.9667 × 1	0.7125 × 1	0.9341 × 1	0.7375 × (−1)	2.6133 > 0.7375	Vote S_1 is healthy line
		Overhead line S_2	0.9667 × 1	0.7125 × 1	0.9341 × 1	0.7375 × 1	3.3508 > 0	Vote S_2 is healthy line
		Hybrid line S_3	0.9667 × 1	0.7125 × 1	0.9341 × 1	0.7375 × (−1)	2.6133 > 0.7375	Vote S_3 is healthy line
		Cable line S_4	**0.9667 × (−1)**	**0.7125 × (−1)**	**0.9341 × (−1)**	**0.7375 × (−1)**	**3.3508 > 0**	**Vote S_4 is fault line**
10	1000	Overhead line S_1	0.9667 × 1	0.7125 × (−1)	0.9341 × 1	0.7375 × 1	2.6383 > 0.7125	Vote S_1 is healthy line
		Overhead line S_2	0.9667 × 1	0.7125 × (−1)	0.9341 × 1	0.7375 × 1	2.6383 > 0.7125	Vote S_2 is healthy line
		Hybrid line S_3	0.9667 × 1	0.7125 × 1	0.9341 × 1	0.7375 × (−1)	2.6133 > 0.7375	Vote S_3 is healthy line
		Cable line S_4	**0.9667 × (−1)**	**0.7125 × (−1)**	**0.9341 × (−1)**	**0.7375 × (−1)**	**3.3508 > 0**	**Vote S_4 is fault line**
6	2000	Overhead line S_1	0.9667 × 1	0.7125 × 1	0.9341 × 1	0.7375 × 1	3.3508 > 0	Vote S_1 is healthy line
		Overhead line S_2	0.9667 × 1	0.7125 × (−1)	0.9341 × 1	0.7375 × 1	2.6383 > 0.7125	Vote S_2 is healthy line
		Hybrid line S_3	0.9667 × 1	0.7125 × 1	0.9341 × 1	0.7375 × (−1)	2.6133 > 0.7375	Vote S_3 is healthy line
		Cable line S_4	**0.9667 × (−1)**	**0.7125 × (−1)**	**0.9341 × (−1)**	**0.7375 × (−1)**	**3.3508 > 0**	**Vote S_4 is fault line**
10	2000	Overhead line S_1	0.9667 × 1	0.7125 × (−1)	0.9341 × 1	0.7375 × 1	2.6383 > 0.7125	Vote S_1 is healthy line
		Overhead line S_2	0.9667 × 1	0.7125 × (−1)	0.9341 × 1	0.7375 × 1	2.6383 > 0.7125	Vote S_2 is healthy line
		Hybrid line S_3	0.9667 × 1	0.7125 × 1	0.9341 × 1	0.7375 × 1	3.3508 > 0	Vote S_3 is healthy line
		Cable line S_4	**0.9667 × (−1)**	**0.7125 × (−1)**	**0.9341 × (−1)**	**0.7375 × 1**	**2.6133 > 0.7375**	**Vote S_4 is fault line**

S_1 is accurately checked out through the comparison of the values above, even if the grounding resistance value is as high as 1000 Ω.

Table 8 offers the selection result of hybrid line S_3 when the initial fault phase is 0°. An experiment of fault line under the end of the high resistance ground is made to further verify the accuracy of this method. Similarly, the entropy value of the main component atomic library, fundamental atomic library, and transient component atomic libraries 1 and 2 at this time is 0.9667, 0.95, 0.9833, and 0.9833 and the accuracy rate of the four test sets after being trained by the ELM network is 100%, 90%, 85%, and 75%; therefore the corresponding confidence degree of every atomic library is 0.9667, 0.855, 0.8358, and 0.7375. Table 8 shows that even when the fault occurs at the distance of 17 km under 2000 Ω, the voting result is 3.395 > 0, which indicates that fault occurs in line S_3.

Table 9 offers the selection result of cable line S_4 when the initial fault phase is 0°. The entropy value of every atomic library is 0.9667, 0.95, 0.9833, and 0.9833; the accuracy rate of the test sets after the atomic libraries are trained by the ELM network is 100%, 75%, 95%, and 75%; therefore the confidence degree of every atomic library is 0.9667, 0.7125, 0.9341, and 0.7375. The voting results prove that the method proposed

Table 10: Information entropy value of every atom library.

	Main component atom library	Fundamental atom library	Transient characteristic atom library number 1	Transient characteristic atom library number 2
Information entropy value	0.9792	0.9583	0.9861	0.9861

Table 11: Test result of every ELM network.

Samples style	ELM	
	Correct samples number/total number	Accuracy rate
Main component atom library	23/24	95.8333%
Fundamental atom library	20/24	83.3333%
Transient characteristic atom library number 1	21/24	87.5%
Transient characteristic atom library number 2	19/24	79.1667%
Total	83/96	86.4583%

in this paper can select fault line accurately when grounding fault of cable line occurs.

9. Applicability Analysis

Since the distribution network is exposed to the outdoor environment, when the fault occurs, the current signals collected contain large amounts of noise, which is a negative factor for FLS. In order to test the antinoise interference ability of the method proposed in this paper, a strong noise of 0.5 db is added to the zero sequence current signals. Figures 18(a) and 18(b) present the zero sequence current waveforms of overhead line S_1 when grounding fault occurs at 10 Ω and 2000 Ω. It shows that when the added noise is 0.5 db, compared with Figure 2, the zero sequence current signals of each line have changed greatly and there are lots of burrs on the waveforms due to noise interference, which makes the transient characteristics of fault line almost undistinguishable and which is harmful for FLS [32–34]. The zero sequence current signals of each line are much weaker in Figure 18(b) since it represents grounding fault under high resistance with noise interference. Therefore, whether or not accurate FLS of weak signals can be achieved with strong noise interference is important for testing the applicability of the proposed method. Table 10 shows the entropy values of each atomic library with noise interference, and Table 11 is the testing results of each ELM network.

It can be seen from Table 11 that, with the added 0.5 db noise, the overall accuracy of line selection of a single atomic library of ELM network can only reach 86.4583% without considering measuring instrument error, electromagnetic interference, and other factors, and the accuracy of the selection method based on one single fault characteristic is not successful in practice with all kinds of complicated conditions in consideration. So the method proposed in this paper tries to select fault line through fault voting of multiple atomic library fusion. Table 12 is the fault selection results of each line with strong noise interference when the initial phase angle is 0°.

Table 12 shows that, with the added 0.5 db noise, the method based on multiple atomic libraries of ELM model can still accurately select the fault line without the influence of transition resistance, fault distance, and other factors. Compared with the results based on one single atomic library shown in Table 11, effectively fusing with a variety of fault characteristics, this method improves the correct rate of FLS with its excellent fault tolerance and robustness.

10. Conclusions

A fault voting selection method based on the combination of atomic sparse decomposition and ELM is proposed in this paper. The following are the conclusions of the research.

(1) ASD breaks through the idea of fixed complete basis to decompose signal; it utilizes signal features to decompose signal by choosing adaptively appropriate base of atom library. Because the ASD has adaptive, analytical, and sparse characteristics, the algorithm has outstanding advantage of fault feature extraction of power system; the atoms extracted not only restore the main characteristic of initial signal well but also apply to judge the fault line with ELM network conveniently.

(2) It could get the unique optimum solution by set hidden layer neurons number of ELM network and does not need to adjust connection weight and hidden layer threshold. We construct four ELM networks and train and test each sample atom library to improve the accuracy of every sample test set, and it provided the base for FLS at next step. Through our research, we found that ELM network has fast learning speed, good generalization performance, and less adjustment parameters; it better applied to the fault diagnosis field of power system.

(3) Information entropy can measure the confidence degree of every sample library, combined the ELM network accuracy to establish FLS confidence degree, and then constructed fault vote selection mechanism by ELM network output and confidence degree value. As can be seen by voting, the accuracy of the method is 100%, and it is not affected by fault distance

Table 12: Fault voting result with strong noise.

(a) Fault voting result of overhead line S_1

Fault location/km	Transition resistance/Ω	Feeder line style	Atom 1	Atom 2	Atom 3	Atom 4	Voting results	Fault line selection results
5	5	**Overhead line S_1**	**0.9384 × (−1)**	**0.7986 × (−1)**	**0.8217 × (−1)**	**0.7807 × (−1)**	**3.3394 > 0**	**Vote S_1 is fault line**
		Overhead line S_2	0.9384 × 1	0.7986 × 1	0.8217 × (−1)	0.7807 × (−1)	1.737 > 1.6024	Vote S_2 is healthy line
		Hybrid line S_3	0.9384 × 1	0.7986 × 1	0.8217 × 1	0.7807 × 1	3.3394 > 0	Vote S_3 is healthy line
		Cable line S_4	0.9384 × 1	0.7986 × 1	0.8217 × 1	0.7807 × (−1)	2.5587 > 0.7807	Vote S_4 is healthy line
10	500	**Overhead line S_1**	**0.9384 × 1**	**0.7986 × (−1)**	**0.8217 × (−1)**	**0.7807 × (−1)**	**2.401 > 0.9384**	**Vote S_1 is fault line**
		Overhead line S_2	0.9384 × 1	0.7986 × 1	0.8217 × 1	0.7807 × 1	3.3394 > 0	Vote S_2 is healthy line
		Hybrid line S_3	0.9384 × 1	0.7986 × 1	0.8217 × 1	0.7807 × 1	3.3394 > 0	Vote S_3 is healthy line
		Cable line S_4	0.9384 × 1	0.7986 × 1	0.8217 × 1	0.7807 × 1	3.3394 > 0	Vote S_4 is healthy line

(b) Fault voting result of hybrid line S_3

Fault location/km	Transition resistance/Ω	Feeder line style	Atom 1	Atom 2	Atom 3	Atom 4	Voting results	Fault line selection results
5	500	Overhead line S_1	0.9384 × 1	0.7986 × 1	0.8217 × 1	0.7807 × (−1)	2.5587 > 0.7807	Vote S_1 is healthy line
		Overhead line S_2	0.9384 × 1	0.7986 × 1	0.8217 × 1	0.7807 × 1	3.3394 > 0	Vote S_2 is healthy line
		Hybrid line S_3	**0.9384 × (−1)**	**0.7986 × (−1)**	**0.8217 × 1**	**0.7807 × (−1)**	**2.5177 > 0.8217**	**Vote S_3 is fault line**
		Cable line S_4	0.9384 × 1	0.7986 × 1	0.8217 × (−1)	0.7807 × 1	2.5177 > 0.8217	Vote S_4 is healthy line
14	2000	Overhead line S_1	0.9384 × 1	0.7986 × 1	0.8217 × 1	0.7807 × (−1)	2.5587 > 0.7807	Vote S_1 is healthy line
		Overhead line S_2	0.9384 × 1	0.7986 × (−1)	0.8217 × 1	0.7807 × 1	2.5408 > 0.7986	Vote S_2 is healthy line
		Hybrid line S_3	**0.9384 × (−1)**	**0.7986 × (−1)**	**0.8217 × (−1)**	**0.7807 × (−1)**	**3.3394 > 0**	**Vote S_3 is fault line**
		Cable line S_4	0.9384 × 1	0.7986 × 1	0.8217 × 1	0.7807 × 1	3.3394 > 0	Vote S_4 is healthy line

(c) Fault voting result of cable line S_4

Fault location/km	Transition resistance/Ω	Feeder line style	Atom 1	Atom 2	Atom 3	Atom 4	Voting results	Fault line selection results
4	200	Overhead line S_1	0.9384 × 1	0.7986 × 1	0.8217 × 1	0.7807 × (−1)	2.5587 > 0.7807	Vote S_1 is healthy line
		Overhead line S_2	0.9384 × 1	0.7986 × 1	0.8217 × 1	0.7807 × 1	3.3394 > 0	Vote S_2 is healthy line
		Hybrid line S_3	0.9384 × 1	0.7986 × 1	0.8217 × 1	0.7807 × 1	3.3394 > 0	Vote S_3 is healthy line
		Cable line S_4	**0.9384 × (−1)**	**0.7986 × 1**	**0.8217 × (−1)**	**0.7807 × (−1)**	**2.5408 > 0.7986**	**Vote S_4 is fault line**
8	10	Overhead line S_1	0.9384 × 1	0.7986 × (−1)	0.8217 × 1	0.7807 × 1	2.5408 > 0.7986	Vote S_1 is healthy line
		Overhead line S_2	0.9384 × 1	0.7986 × 1	0.8217 × 1	0.7807 × 1	3.3394 > 0	Vote S_2 is healthy line
		Hybrid line S_3	0.9384 × 1	0.7986 × 1	0.8217 × 1	0.7807 × 1	3.3394 > 0	Vote S_3 is healthy line
		Cable line S_4	**0.9384 × (−1)**	**0.7986 × 1**	**0.8217 × (−1)**	**0.7807 × (−1)**	**2.5408 > 0.7986**	**Vote S_4 is fault line**

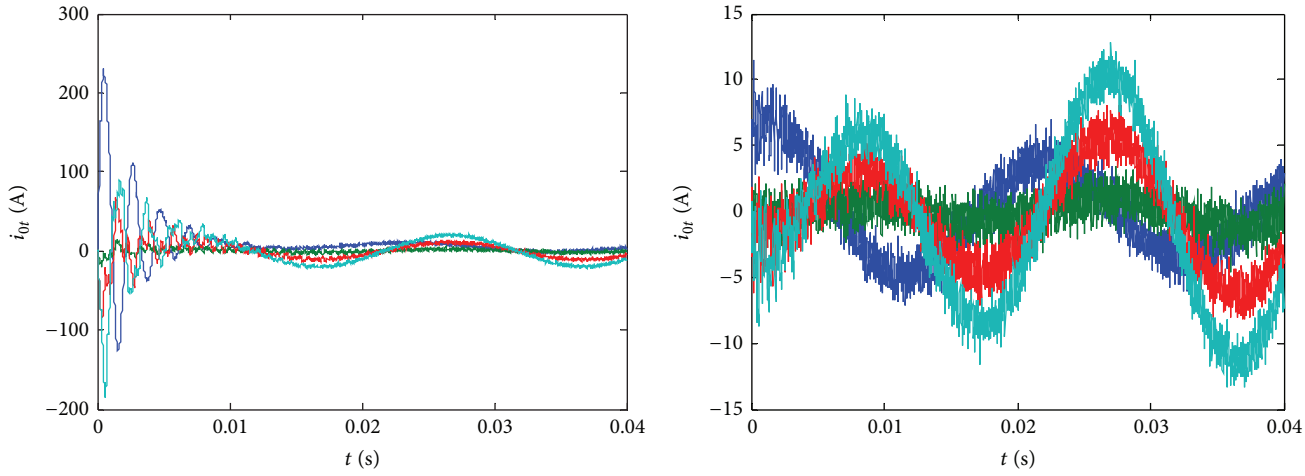

(a) 10 Ω to ground fault

(b) 2000 Ω to ground fault

Figure 18: Zero sequence current with strong noise.

and transition resistance value; besides, the method can accurately achieve FLS with 0.5 db strong noise interference.

(4) Because ASD algorithm adopts matching pursuit way to find the best atom in decomposition process, it needs a large number of inner product operations, so it needs to spend a long time. Therefore, the future work is how to reduce matching pursuit calculation time.

Notations

ASD: Atomic sparse decomposition
ELM: Extreme learning machine
FLS: Fault line selection
HHT: Hilbert-Huang transform.

Conflict of Interests

The authors declare that there is no conflict of interests regarding the publication of this paper.

Acknowledgments

This work was supported by National Natural Science Fund (61403127) of China, Science and Technology Research (12B470003, 14A470004, and 14A470001) of Henan Province, Control Engineering Lab Project (KG2011-15, KG2014-04) of Henan Province, China, and Doctoral Fund (B2014-023) of Henan Polytechnic University, China.

References

[1] X. Dong and S. Shi, "Identifying single-phase-to-ground fault feeder in neutral noneffectively grounded distribution system using wavelet transform," *IEEE Transactions on Power Delivery*, vol. 23, no. 4, pp. 1829–1837, 2008.

[2] J. Zhang, Z. He, and Y. Jia, "Fault line identification approach based on S-transform," *Proceedings of the CSEE*, vol. 31, no. 10, pp. 109–115, 2011.

[3] J. Ren, W. Sun, M. Zhou, and A. Cao, "Transient algorithm for single-line to ground fault selection in distribution networks based on mathematical morphology," *Automation of Electric Power Systems*, vol. 32, no. 1, pp. 70–75, 2008.

[4] T. Cui, X. Dong, Z. Bo, and A. Juszczyk, "Hilbert-transform-based transient/intermittent earth fault detection in noneffectively grounded distribution systems," *IEEE Transactions on Power Delivery*, vol. 26, no. 1, pp. 143–151, 2011.

[5] X. W. Wang, J. W. Wu, and R. Y. Li, "A novel method of fault line selection based on voting mechanism of prony relative entropy theory," *Electric Power*, vol. 46, no. 1, pp. 59–64, 2013.

[6] H. Shu, L. Gao, R. Duan, P. Cao, and B. Zhang, "A novel hough transform approach of fault line selection in distribution networks using total zero-sequence current," *Automation of Electric Power Systems*, vol. 37, no. 9, pp. 110–116, 2013.

[7] S. Lin, Z. He, T. Zang, and Q. Qian, "Novel approach of fault type classification in transmission lines based on rough membership neural networks," *Proceedings of the Chinese Society of Electrical Engineering*, vol. 30, no. 28, pp. 72–79, 2010.

[8] S. Zhang, Z.-Y. He, Q. Wang, and S. Lin, "Fault line selection of resonant grounding system based on the characteristics of charge-voltage in the transient zero sequence and support vector machine," *Power System Protection and Control*, vol. 41, no. 12, pp. 71–78, 2013.

[9] Q. Li and J. Z. Xu, "Power system fault diagnosis based on subjective Bayesian approach," *Automation of Electric Power Systems*, vol. 31, no. 15, pp. 46–50, 2007.

[10] X.-W. Wang, S. Tian, Y.-D. Li, T. Li, Y.-J. Zhang, and Q. Li, "A novel fault section location method for small current neutral grounding system based on characteristic frequency sequence of S-transform," *Power System Protection and Control*, vol. 40, no. 14, pp. 109–115, 2012.

[11] X. W. Wang, Y. X. Hou, S. Tian, Y.-D. Li, J. Gao, and X.-X. Wei, "A novel fault line selection method based on time-frequency atom decomposition and grey correlation analysis of small current to ground system," *Journal of China Coal Society*, 2014.

[12] H.-S. Zhao, L.-X. Yao, L.-F. Ke, and L. Wu, "A novel method for fault line selection and location in distribution system," *Power System Protection and Control*, vol. 38, no. 16, pp. 6–10, 2010.

[13] S. G. Mallat and Z. Zhang, "Matching pursuits with time-frequency dictionaries," *IEEE Transactions on Signal Processing*, vol. 41, no. 12, pp. 3397–3415, 1993.

[14] L. Lovisolo, E. A. B. da Silva, M. A. M. Rodrigues, and P. S. R. Diniz, "Efficient coherent adaptive representations of monitored electric signals in power systems using damped sinusoids," *IEEE Transactions on Signal Processing*, vol. 53, no. 10, part 1, pp. 3831–3846, 2005.

[15] L. Lovisolo, M. P. Tcheou, E. A. B. da Silva, M. A. M. Rodrigues, and P. S. R. Diniz, "Modeling of electric disturbance signals using damped sinusoids via atomic decompositions and its applications," *EURASIP Journal on Advances in Signal Processing*, vol. 2007, Article ID 29507, 2007.

[16] X. Zhang, J. Liang, F. Zhang, L. Zhang, and B. Xu, "Combined model for ultra short-term wind power prediction based on sample entropy and extreme learning machine," *Proceedings of the Chinese Society of Electrical Engineering*, vol. 33, no. 25, pp. 33–40, 2013.

[17] Q. Yuan, W. Zhou, S. Li, and D. Cai, "Approach of EEG detection based on ELM and approximate entropy," *Chinese Journal of Scientific Instrument*, vol. 33, no. 3, pp. 514–519, 2012.

[18] F. Y. Wu, X. F. Le, and D. L. Nan, "A short-term wind speed prediction model using phase-space reconstructed extreme learning machine," *Proceedings of the CSU-EPSA*, vol. 25, no. 1, pp. 136–141, 2013.

[19] G. B. Huang, Q. Y. Zhu, and C. K. Siew, "Extreme learning machine: theory and applications," *Neurocomputing*, vol. 70, no. 1–3, pp. 489–501, 2006.

[20] J. J. Jia, Q. W. Gong, X. Li, Q. Y. Guan, and S. L. Chen, "Single-phase adaptive recluse of shunt compensated transmission lines using atomic decomposition," *Automation of Electric Power Systems*, vol. 37, no. 5, pp. 117–123, 2013.

[21] Q. Jia, L. Shi, N. Wang, and H. Dong, "A fusion method for ground fault line detection in compensated power networks based on evidence theory and information entropy," *Transactions of China Electrotechnical Society*, vol. 27, no. 6, pp. 191–197, 2012.

[22] L. Fu, Z. Y. He, R. K. Mai, and Q. Q. Qian, "Application of approximate entropy to fault signal analysis in electric power system," *Proceedings of the Chinese Society of Electrical Engineering*, vol. 28, no. 28, pp. 68–73, 2008.

[23] Q.-Q. Jia, Q.-X. Yang, and Y.-H. Yang, "Fusion strategy for single phase to ground fault detection implemented through fault measures and evidence theory," *Proceedings of the CSEE*, vol. 23, no. 12, pp. 6–11, 2003.

[24] H. R. Karimi, P. J. Maralani, B. Lohmann, and B. Moshiri, "H_∞ control of parameter-dependent state-delayed systems using polynomial parameter-dependent quadratic functions," *International Journal of Control*, vol. 78, no. 4, pp. 254–263, 2005.

[25] S. Yin, S. X. Ding, A. Haghani, H. Hao, and P. Zhang, "A comparison study of basic data-driven fault diagnosis and process monitoring methods on the benchmark Tennessee Eastman process," *Journal of Process Control*, vol. 22, no. 9, pp. 1567–1581, 2012.

[26] H. M. Yang, L. Huang, C. F. He, and D. X. Yi, "Probabilistic prediction of transmission line fault resulted from disaster of ice storm," *Power System Technology*, vol. 36, no. 4, pp. 213–218, 2012.

[27] H. R. Karimi, "A computational method for optimal control problem of time-varying state-delayed systems by Haar wavelets," *International Journal of Computer Mathematics*, vol. 83, no. 2, pp. 235–246, 2006.

[28] H. Zhang, Z. He, and J. Zhang, "A fault line detection method for indirectly grounding power system based on quantum neural network and evidence fusion," *Transactions of China Electrotechnical Society*, vol. 24, no. 12, pp. 171–178, 2009.

[29] H. R. Karimi, "Robust H∞ filter design for uncertain linear systems over network with network-induced delays and output quantization," *Modeling, Identification and Control*, vol. 30, no. 1, pp. 27–37, 2009.

[30] Z. Kang, D. Li, and X. Liu, "Faulty line selection with non-power frequency transient components of distribution network," *Electric Power Automation Equipment*, vol. 31, no. 4, pp. 1–6, 2011.

[31] S. Yin, H. Luo, and S. X. Ding, "Real-time implementation of fault-tolerant control systems with performance optimization," *IEEE Transactions on Industrial Electronics*, vol. 61, no. 5, pp. 2402–2411, 2014.

[32] X. W. Wang, J. Gao, X. X. Wei, and Y. X. Hou, "A novel fault line selection method based on improved oscillator system of power distribution network," *Mathematical Problems in Engineering*, vol. 2014, Article ID 901810, 19 pages, 2014.

[33] H. R. Karimi, N. A. Duffie, and S. Dashkovskiy, "Local capacity H_∞ control for production networks of autonomous work systems with time-varying delays," *IEEE Transactions on Automation Science and Engineering*, vol. 7, no. 4, pp. 849–857, 2010.

[34] X. W. Wang, X. X. Wei, J. Gao, Y. X. Hou, and Y. F. Wei, "Stepped fault line selection method based on spectral kurtosis and relative energy entropy of small current to ground system," *Journal of Applied Mathematics*, vol. 2014, Article ID 726205, 18 pages, 2014.